LJMU Research Online

Murphy-Glaysher, FJ, Darnley, MJ, Harvey, EJ, Newsam, AM, Page, KL, Starrfield, S, Wagner, RM, Woodward, CE, Terndrup, DM, Kafka, S, Arranz Heras, T, Berardi, P, Bertrand, E, Biernikowicz, R, Boussin, C, Boyd, D, Buchet, Y, Bundas, M, Coulter, D, Dejean, D, Diepvens, A, Dvorak, S, Edlin, J, Eenmae, T, Eggenstein, H, Fournier, R, Garde, O, Gout, J, Janzen, D, Jordanov, P, Kiiskinen, H, Lane, D, Larochelle, R, Leadbeater, R, Mankel, D, Martineau, G, Miller, I, Modic, R, Montier, J, Morales Aimar, M, Muyllaert, E, Naves Nogues, R, O'Keeffe, D, Oksanen, A, Pyatnytskyy, M, Rast, R, Rodgers, B, Rodriguez Perez, D, Schorr, F, Schwendeman, E, Shadick, S, Sharpe, S, Soldán Alfaro, F, Sove, T, Stone, G, Tordai, T, Venne, R, Vollmann, W, Vrastak, M and Wenzel, K

 V392 Persei: a γ-ray bright nova eruption from a known dwarf nova

http://researchonline.ljmu.ac.uk/id/eprint/17097/

Article

The version presented here may differ from the published version or from the version of the record. Please see the repository URL above for details on accessing the published version and note that access may require a subscription.

For more information please contact researchonline@ljmu.ac.uk

V392 Persei: a γ-ray bright nova eruption from a known dwarf nova

F. J. Murphy-Glaysher,[1]⋆ M. J. Darnley,[1] É. J. Harvey,[1] A. M. Newsam,[1] K. L. Page,[2]
S. Starrfield,[3] R. M. Wagner,[4] C. E. Woodward,[5] D. M. Terndrup,[4] S. Kafka,[6,7]
T. Arranz Heras,[6] P. Berardi,[8] E. Bertrand,[8] R. Biernikowicz,[6] C. Boussin,[8,9] D. Boyd,[6]
Y. Buchet,[8] M. Bundas,[6] D. Coulter,[6] D. Dejean,[8] A. Diepvens,[6] S. Dvorak,[6] J. Edlin,[8]
T. Eenmae,[6,10] H. Eggenstein,[6] R. Fournier,[6] O. Garde,[8,11] J. Gout,[6] D. Janzen,[6,12] P. Jordanov,[6]
H. Kiiskinen,[6] D. Lane,[6] R. Larochelle,[6,12] R. Leadbeater,[8] D. Mankel,[6] G. Martineau,[8]
I. Miller,[6] R. Modic,[6] J. Montier[8] M. Morales Aimar,[6] E. Muyllaert,[6] R. Naves Nogues,[6]
D. O'Keeffe,[6] A. Oksanen,[6] M. Pyatnytskyy,[6] R. Rast,[6,12] B. Rodgers,[6,12] D. Rodriguez Perez,[6]
F. Schorr,[6] E. Schwendeman,[6] S. Shadick,[6,12] S. Sharpe,[6] F. Soldán Alfaro,[6,13] T. Sove,[6,12]
G. Stone,[6] T. Tordai,[6] R. Venne,[6] W. Vollmann,[6] M. Vrastak,[6] K. Wenzel[6]

[1]*Astrophysics Research Institute, Liverpool John Moores University, IC2, Liverpool Science Park, Brownlow Hill, Liverpool L3 5RF, UK*
[2]*School of Physics & Astronomy, University of Leicester, LEI 7RH, UK*
[3]*School of Earth and Space Exploration, Arizona State University, Box 871404, Tempe, AZ 85287-1404, USA*
[4]*Department of Astronomy, The Ohio State University, Columbus, OH 43210, USA*
[5]*Minnesota Institute for Astrophysics, School of Physics & Astronomy, 116 Church Street SE, University of Minnesota, Minneapolis, MN 55455, USA*
[6]*American Association of Variable Star Observers, 49 Bay State Rd, Cambridge, MA 02138, USA*
[7]*American Meteorological Society, 45 Beacon Street, Boston, MA 02108-3693, USA*
[8]*Astronomical Ring for Access to Spectroscopy —* http://www.astrosurf.com/aras
[9]*Observatoire de l'Eridan et de la Chevelure de Bérénice, France*
[10]*Tartu Observatory, University of Tartu, Estonia*
[11]*Observatoire de la Tourbière, France*
[12]*Department of Physics and Engineering Physics, University of Saskatchewan, Saskatoon, SK, S7N 5E2, Canada*
[13]*Seville University, Seville, Spain*

ABSTRACT

V392 Persei is a known dwarf nova (DN) that underwent a classical nova eruption in 2018. Here we report ground-based optical, *Swift* UV and X-ray, and *Fermi*-LAT γ-ray observations following the eruption for almost three years. V392 Per is one of the fastest evolving novae yet observed, with a t_2 decline time of 2 days. Early spectra present evidence for multiple and interacting mass ejections, with the associated shocks driving both the γ-ray and early optical luminosity. V392 Per entered Sun-constraint within days of eruption. Upon exit, the nova had evolved to the nebular phase, and we saw the tail of the super-soft X-ray phase. Subsequent optical emission captured the fading ejecta alongside a persistent narrow line emission spectrum from the accretion disk. Ongoing hard X-ray emission is characteristic of a standing accretion shock in an intermediate polar. Analysis of the optical data reveals an orbital period of 3.230 ± 0.003 days, but we see no evidence for a white dwarf (WD) spin period. The optical and X-ray data suggest a high mass WD, the pre-nova spectral energy distribution (SED) indicates an evolved donor, and the post-nova SED points to a high mass accretion rate. Following eruption, the system has remained in a nova-like high mass transfer state, rather than returning to the pre-nova DN low mass transfer configuration. We suggest that this high state is driven by irradiation of the donor by the nova eruption. In many ways, V392 Per shows similarity to the well-studied nova and DN GK Persei.

Key words: novae — cataclysmic variables — stars: individual (V392 Per) — accretion disks — transients: novae — x-rays: stars

⋆ E-mail: F.J.MurphyGlaysher@2018.ljmu.ac.uk

1 INTRODUCTION

Classical novae (CNe) are among the most luminous stellar transients, exceeded only by supernovae and gamma-ray bursts. CNe are binary systems in which a white dwarf (WD; typically composed of carbon and oxygen, or of oxygen and neon) accretes hydrogen-rich material from a donor star via an accretion disk (Warner 1995). Accretion proceeds via Roche-lobe overflow for the majority of CNe; those with main sequence or sub-giant donors. For CNe with giant donors, material is accreted from the giant's wind. The accreted envelope builds in temperature and pressure until a thermonuclear runaway occurs (Starrfield et al. 1976, 2016; Starrfield 1989), blasting material from the WD's surface, leaving the WD and donor relatively unscathed. The CN is observed as a rapid increase in optical luminosity of 10–15 magnitudes, followed by a slower decline.

CNe are a sub-type of cataclysmic variable (CV); a class that includes dwarf novae (DNe) and nova-likes (NL). DN outbursts are less luminous than CN eruptions and are powered by the release of gravitational potential energy, which can occur when hydrogen-rich material in the accretion disk is suddenly deposited onto the WD. DN outbursts are produced in systems where the accretion rate ($\dot{M}$) is lower than the critical rate (Smak 1983, see their Equation 2), due to thermal or tidal instabilities within the disk (Osaki 1996). For a given disk radius, CVs with high $\dot{M}$ produce hot, stable disks – the NL systems, that do not show DN outbursts.

Abdo et al. (2010) first reported detection of γ-ray emission from a nova; the V407 Cygni ejecta shocked surrounding circumstellar wind, accelerating leptons to relativistic velocities and emitting γ-ray photons of energy > 100 MeV. Since that initial discovery, γ-ray signatures have been exhibited in increasing numbers of classical novae (see Aydi et al., 2020b; Chomiuk, Metzger & Shen 2021a, for recent reviews). Several γ-ray detected novae occurred in systems with red giant donors: V407 Cyg, V1535 Sco (Franckowiak et al. 2018), and the recurrent novae V745 Sco (Cheung et al. 2014; Banerjee et al. 2014), V3890 Sgr (Buson, Jean & Cheung 2019) and RS Oph (Cheung, Ciprini & Johnson 2021). In these systems, the shocks generating the γ-rays are likely to originate in collisions between the nova ejecta and the dense red-giant winds and circumbinary material. However, the other γ-ray emitting novae have main sequence companions and are unlikely to be surrounded by dense winds. In these systems, the shocks are proposed to be due to interaction between multiple ejection components (Aydi et al. 2020b). Studies suggest that the γ-ray and optical emission can show correlated peaks, with the shocks driving the optical emission (Ackermann et al. 2014). Aydi et al. (2020a) demonstrated that shock-powered emission was responsible for the bulk of the luminosity of V906 Car, with multiple simultaneous γ-ray and optical flares.

A number of CVs have been observed to undergo both CN eruptions and DN outbursts. GK Per (Bianchini et al. 1986; Zemko et al. 2017), V446 Her (Honeycutt, Robertson & Kafka 2011), RR Pic, V1047 Cen, and V606 Aql (Kato & Kojiguchi 2021) are CNe that subsequently underwent DN outbursts. Z Cam, AT Cnc, and 2MASS J17012815-4306123 (Nova Sco 1437) are known DNe surrounded by proposed ancient CN shells (Shara et al. 2007, 2012, 2017). V1213 Cen and V1017 Sgr exhibited DN outbursts six and eighteen years, respectively, before a CN; V1017 Sgr also showed post-nova DN outbursts (Mróz et al. 2016). The nebula Te 11, with a DN at its centre, was proposed to be the shell of an ancient nova eruption, rather than a planetary nebula (Miszalski et al. 2016).

V392 Persei was a known CV with a few observed DN outbursts, with quiescent magnitudes of $15.0 < m_{\rm pg} < 17.0$ (Downes & Shara 1993) and $V > 17$ (Zwitter & Munari 1994). Its CN eruption was

discovered on 2018 Apr 29 (UT) by Y. Nakamura, with an unfiltered brightness of 6.2 mag (Wagner et al. 2018). The following day, γ-ray emission was detected from V392 Per ($> 6\sigma$; Li, Chomiuk & Strader 2018), with detections continuing for 11 days (Gordon et al. 2021; Albert et al. 2022). Non-thermal synchrotron emission during early radio observations (Chomiuk et al. 2021b) provided further support for the presence of shocks during the eruption. The system is proposed to host an evolved donor similar to the sub-giant donors of U Sco and GK Per, or the low-luminosity giant donor of M31N 2008-12a (Darnley & Starrfield 2018). Potential orbital periods of 3.4118 days (Munari, Moretti & Maitan 2020a) and 3.21997 days (Schaefer 2021) are consistent with an evolved donor.

In this paper, we present panchromatic data from the 2018 nova eruption of V392 Per and its subsequent evolution. In Section 2 we describe our observational dataset. We present the photometry and spectra in Section 3 and the spectral analysis in Section 4. We discuss our results in Section 5 and summarise our findings in Section 6.

2 DATA

Observations of V392 Per were obtained by the fully robotic 2.0 m Liverpool Telescope (LT; Steele et al. 2004) on La Palma. LT images were taken with the IO:O instrument (Smith & Steele 2017) through $u'BVr'i'z'$ filters. Additional i'-band photometry was collected using both Las Cumbres Observatory (LCOGT; Brown et al. 2013) 1.0 m Telescopes at McDonald Observatory in Fort Davis, Texas. We also used optical photometry from the American Association of Variable Star Observers (AAVSO; Kafka 2021).

The LT and LCOGT data were reduced using standard tools within PyRAF (Science Software Branch at STScI 2012) and aperture photometry was performed using `qphot`. The data were calibrated against 25 reference stars in the field (see Table A2), selected from the Pan-STARRS catalogue (DR1; Chambers & Pan-STARRS Team 2016). The reference stars had $g'r'i'z'$ magnitudes $14 < m < 22$, and were sufficiently distant from other stars. Pan-STARRS photometry was converted to Johnson BV and Sloan-like $r'i'z'$ using relations in Tonry et al. (2012). A single star in a *Swift* observation of the field was utilised to calibrate the u'-band photometry. For comparison with the LT/LCOGT data, the AAVSO photometry was converted to the AB system using relations from Blanton & Roweis (2007). Due to the typically larger or unknown uncertainties on the AAVSO data and the large number of independent observers, we opted not to apply colour corrections to these data.

LT spectra were collected using SPRAT (with a spectral resolution $R \approx 350$; Piascik et al. 2014, blue-optimised mode) and FRODOSpec (Barnsley, Smith & Steele 2012). Groups of three or five exposures were taken at each epoch. Cosmic rays were removed by a two-stage process involving interactive interpolation and exposure combination with the IRAF routine `scombine` (Tody 1986). The resolving power of the FRODOSpec red arm was $R \approx 2200$ or $R \approx 5300$, and the blue arm was $R \approx 2600$ or $R \approx 5500$. These spectra were reduced using the LT pipeline; producing bias subtracted, flat-fielded, wavelength calibrated, sky-subtracted products.

Relative flux calibration of the SPRAT spectra was conducted with 78 observations of the spectrophotometric standard Hiltner 102 (Stone 1977). Relative flux calibration of the FRODOSpec spectra was performed using observations of the spectrophotometric standard stars Hiltner 102 and BD+33 2642 (Oke 1990) for the higher and lower resolution modes, respectively.

Optical spectra of V392 Per were obtained with the 2.4 m Hiltner telescope of the Michigan-Dartmouth-MIT (MDM) Observatory

on Kitt Peak. The Hiltner spectra were obtained using the Ohio State Multi-Object Spectrograph (OSMOS; Martini et al. 2011). A 1″2 wide entrance long-slit combined with high-efficiency, low-resolution blue and red optimized VPH grisms and a 4096 × 4096 pixel STA CCD, was employed covering either the 3980–6860 Å spectral region (the inner slit position) or the 3200–9000 Å region (the centre slit position). In both cases, the nominal spectral resolution $\Delta\lambda$ was about 3.8 Å corresponding to $R \simeq 1600$ at 6000 Å. Spectra of HgArNeXe spectral line lamps and of a quartz-halogen lamp were obtained to provide wavelength calibration and to flat field the detector respectively. In general, several spectra were obtained of the standard stars Hiltner 102 or G191-B2B (Stone 1977) on each night to remove the instrumental response function and provide relative flux calibration. The spectra were reduced using IRAF packages to subtract the bias overscans from each of the four quadrants of the detector and produce flat-fielded, one dimensional wavelength and flux calibrated extracted spectra.

We obtained optical spectra of V392 Per at two epochs with the 8.4 m Large Binocular Telescope (LBT; Hill et al. 2008) and the Multi Object Double Spectrograph (MODS; Pogge et al. 2010). MODS utilizes separate and optimized blue and red channel spectrographs. Observations at both epochs consisted of simultaneous blue and red spectra with R ∼ 1850 and R ∼ 2300 respectively, covering the 3249–10100 Å spectral region. Spectra of HgArNeXe lamps and an internal quartz–halogen lamp were used to determine the wavelength calibration and to flat–field the spectra. Standard stars, including G191-B2B, were used to measure the instrumental response function and to provide relative flux calibration. The spectra were reduced using custom routines to bias-subtract and flat–field the data and then using IRAF (Tody 1986) for spectral extraction, wavelength and flux calibration. The wavelength scale of the 2019 data has been shifted by 2 Å post-reduction to ensure that the position of the Hα emission lines coincide.

All aforementioned spectra were absolute flux calibrated using interpolated $BVr'i'$ photometry (see Section 3.4). Spectra were corrected for heliocentric velocity and dereddened using $E(B - V) = 0.7$ (see Section 3.3). Additional spectra were retrieved from the Astronomical Ring for Access to Spectroscopy database[1] (ARAS; Teyssier 2019). These spectra were only used to measure the P Cygni velocities from the Balmer lines. All spectra are listed in Table A1.

Neil Gehrels *Swift* Observatory (Gehrels et al. 2004) observations of V392 Per (target IDs: 10734 and 10773) were obtained using the X-ray Telescope (XRT; Burrows et al. 2005) and UV/Optical Telescope (UVOT; Roming et al. 2005). An initial observation on 2018 July 20, upon emerging from Sun constraint, was taken to ascertain the suitability of the target for the UVOT UV-grism, and determined that it was too faint. Subsequent observations were taken approximately weekly with XRT, initially in automatic mode, before switching to XRT in photon counting (PC) mode. In October 2018, observations switched to every two weeks until April 2019, from July 2019 observations moved to a four-weekly cadence, and monthly from 2020 January–April. The final observation was taken in 2020 August. *Swift* data were processed and analysed using the standard HEASoft tools and relevant calibration files.

XRT analysis utilised the full event range of grades 0–12. At no point did the data suffer from pile-up. A circular extraction region of 10–15 pixels (2.36″ pixel^{-1}) was used, depending on the source brightness; the background was estimated from a 60 pixel radius

Table 1. Key parameters of the V392 Per eruption.

Methodology:	Discovery at $T_{\max}$	Plateau at t_3
Discovery (MJD)	58237.474	
Eruption: T_0 (MJD)	58233^{+3}_{-2}	58236.0 ± 0.2
Maximum light: $T_{\max}$ (MJD)	58237.474	58237.1 ± 0.3
Rise time: Δt_0 / days	4^{+2}_{-3}	1.1 ± 0.2
t_2 / days	3.1 ± 0.2	2.0 ± 0.1
t_3 / days	8^{+1}_{-2}	4.2 ± 0.3
Plateau onset / days	12 ± 1	$5.2^{+0.9}_{-1.1}$
Plateau duration / days	3 ± 2	5 ± 1
$m_{V,\max}$ / mag	$5.92^{-0.04}_{+0.3}$	5.51 ∓ 0.09
$E(B - V)$ / mag	$0.70^{+0.03}_{-0.02}$	
$M_{V,Gaia}$ / mag	$-9.0^{-0.6}_{+0.4}$	$-9.4^{-0.4}_{+0.3}$
$M_{V,MMRD}$ / mag	-8.5 ∓ 0.2	-8.8 ∓ 0.2
d_{Gaia} / kpc	$3.5^{+0.6}_{-0.5}$	
d_{MMRD} / kpc	2.7 ± 0.5	2.7 ± 0.3

circle, offset from, but close to, the source. Upon examination of the hardness ratio (HR), it was clear that there was no rapid spectral evolution. The on-line XRT product generator[2] (Evans et al. 2009) was used to extract spectra over a number of intervals, during each of which the HR remained approximately constant.

UVOT analysis utilised the updated sensitivity calibrations released in 2020. Magnitudes were estimated using `uvotsource`, with a 3″ radius source extraction region to avoid possible low-level contamination from a nearby source, and 20″ background circle.

All photometry is recorded in Table A3, and near-UV and optical light curves of V392 Per are presented in Figure 1.

3 RESULTS

3.1 Sun constraints

Observation of V392 Per was heavily impacted by on-sky proximity to the Sun at the time of its eruption. Early ground-based observations focussed on spectroscopic data until the system entered its Sun constraint. *Swift* was constrained more severely than ground-based telescopes. The *Swift* Sun constraints covered the periods from discovery up to 2018 Jul 18; 2019 Apr 25 to Jul 20; and 2020 Apr 24 to Jul 19. The *Swift* constraints are shown by the vertical shaded regions in Figure 1.

3.2 Time of eruption

The eruption of V392 Per was discovered on 2018 April 29 by Yuji Nakamura in Kameyama (Wagner et al. 2018); who also collected the last pre-eruption observation on April 21.4627[3], 8.01 days earlier. The discovery observation is the brightest of the nova and one could assume that this coincides with onset of the eruption (T_0), or with maximum light ($T_{\max}$). Thus, we used the *V*-band light curve (see Figure 1) to estimate t_2 and t_3 (the time to decline from peak by two and three magnitudes, respectively) and the rise time Δt_0 (here, using Equation 16 from Hachisu & Kato 2006). Eruption parameters computed via this approach are recorded in Table 1.

However, the light curve follows the P-class morphology (Strope, Schaefer & Henden 2010), exhibiting a pseudo-plateau in the early

---
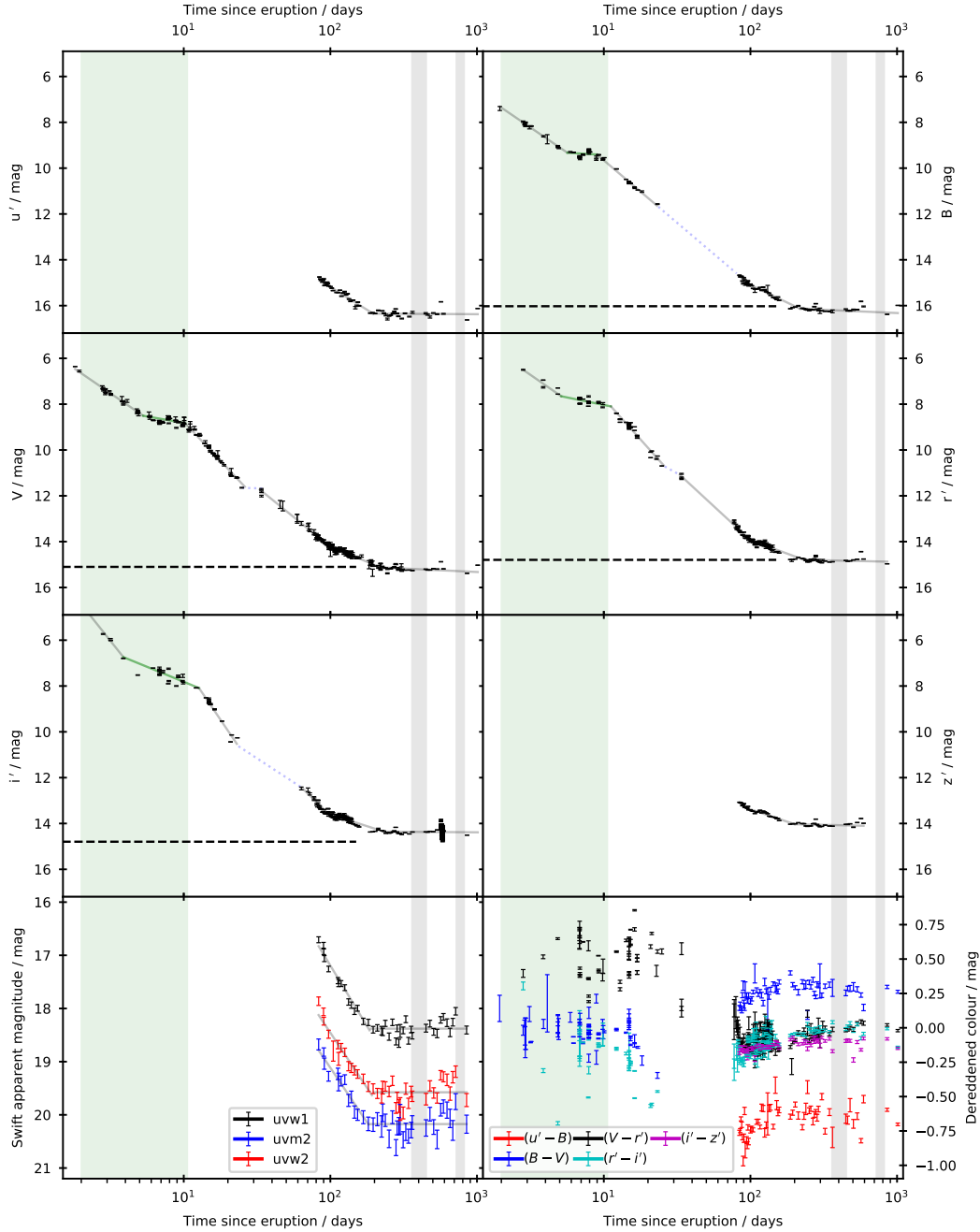
Figure 1. Light curves of the nova eruption of V392 Per from LT, LCOGT, AAVSO, and *Swift* observations. Grey regions indicate the *Swift* Sun constraints, and the green region demarks the epoch of γ-ray detection by *Fermi*-LAT. Broken power laws have been fitted to each light curve (see Section 3.4). The horizontal dashed line indicates photometry of a nearby (9″ away) star in the field. **Bottom-right**: Dereddened colour evolution using $E(B-V) = 0.7$ mag.

evolution (see Figure 1), where the otherwise smooth, steep decline has a relatively flat interval, typically 3–6 mag below peak, followed by another steep decline. If we assume that T_{max} coincides with the earliest *V*-band observation ($V = 6.36$ mag), then plateau onset occurs after a decline of only 2.1 mag. Thus t_3 occurs during the plateau, interrupting the smooth decline, which leads to a relatively long rise time estimate ($\Delta t_0 = 4^{+2}_{-3}$ days) for such a rapidly evolving eruption. Here, poor constraint of the eruption time leads to large uncertainties on all light curve derived parameters.

As an alternative, we assumed that plateau onset coincides

with t_3. In the Strope et al. (2010) sample of 19 P-class novae, only V4021 Sgr entered a plateau earlier (2.4 mag below peak; it also had the slowest decline of the sample). Fixing plateau onset at t_3 provides a conservative estimate of the time of maximum: if the plateau onset occurs later there would have been an earlier and brighter peak. The light curve evolution of V392 Per is well described by a series of broken power-laws (see Figure 1), whose indices depend upon the assumed T_0. Hence, an iterative approach was used to fit the light curves (see Section 3.4) to determine T_{max} such that the plateau

began at t_3. This leads to independent estimates of T_0, Δt_0, t_2, t_3, and $T_{max} = 0.3 \pm 0.3$ days pre-discovery (see Table 1).

Regardless of the method employed, $t_2 < 4$ days: a very fast eruption (Payne-Gaposchkin 1964), and V392 Per is one of the fastest evolving novae yet discovered. Based on the likelihood that maximum light was missed, the rapid evolution of the light curve, the γ-ray detection, and behaviour of similar P-class novae, we adopt these estimates throughout.

3.3 Distance, Extinction, and Astrometry

Stoyanov et al. (2020) measured radial velocities of diffuse interstellar bands and interstellar K I in their V392 Per spectra from 2018 May 1–2, deriving $E(B - V) = 1.2 \pm 0.1$. Munari et al. (2020a) compared the $(B - V)$ colour of V392 Per shortly after peak with the expected intrinsic colour at maximum to derive $E(B - V) = 0.72 \pm 0.06$. The Stoyanov et al. (2020) measurement was very early post-eruption and the ejecta may have added to the extinction column.

The equivalent width of the interstellar sodium doublet absorption line is often used to determine reddening. However, the interstellar Na I-D lines were saturated in our spectra. Stoyanov et al. (2020) also reported saturation of the Na doublet.

The astrometry of V392 Per, as reported by *Gaia* EDR3 (Gaia Collaboration et al. 2016, 2021) is $\alpha = 4^h 43^m 21^s.369814 \pm 0.04$ mas, $\delta = 47°21'25''.84112 \pm 0.03$ mas (J2000). EDR3 reports a parallax measurement for V392 Per of $\varpi = 0.276 \pm 0.046$ mas. Following Bailer-Jones et al. (2021), this leads to a distance estimate of $d = 3.5^{+0.6}_{-0.5}$ kpc. Utilising the 3D dust maps of Green et al. (2019), we estimate the line of sight reddening toward V392 Per to be $E(B - V) = 0.70^{+0.03}_{-0.02}$. This follows the approach used by Darnley & Starrfield (2018)[4], however, both the distance and reddening estimates are smaller due to advances between *Gaia* DR2 and EDR3. This reddening estimate is in agreement with that by Munari et al. (2020a) and we adopt $E(B - V) = 0.7$ throughout. As such, and utilising the plateau method (see Section 3.2), we estimate a peak absolute magnitude $M_{V,Gaia} = -9.4^{-0.4}_{+0.3}$ mag. This large *Gaia* distance and resulting luminous M_V demonstrate that V392 Per is NOT a "faint-fast" nova, like those commonly seen in M 31 and in M 87 (Kasliwal et al. 2011; Shara et al. 2016). Thus the use of the MMRD is justified to check on the *Gaia* distance. The 'S-shaped' MMRD calibrated by Della Valle & Izzo (2020, see their Equation 15) for a nova with $t_2 = 2.0 \pm 0.1$ produces a consistent ($< 2\sigma$) estimate of $M_{V,MMRD} = -8.8 \mp 0.2$, and an MMRD distance estimate of 2.7 ± 0.3 kpc (within 1.4σ of the *Gaia* distance).

3.4 Photometry and light curve fitting

Figure 1 presents the $u'BVr'i'z'$ and *Swift*/UVOT uvw1, uvm2, and uvw2 light curves for V392 Per. The optical observations are shown with the same scale to aid comparison, and the $BVr'i'$ light curves include observations taken by AAVSO observers (all photometric data before the first Sun constraint: see Table A4 for observer details). The colour evolution of the nova is also shown in Figure 1. The series of high-cadence i'-band photometry collected by LT and LCOGT is included and illustrates the high amplitude variations seen (see Section 3.6).

As shown in Figure 1, the optical and near-UV light curves of V392 Per can be broadly replicated by a series of six broken power

---

[4] The parallax reported by Darnley & Starrfield (2018) was actually that of RS Oph, although their reported distance did relate to V392 Per.
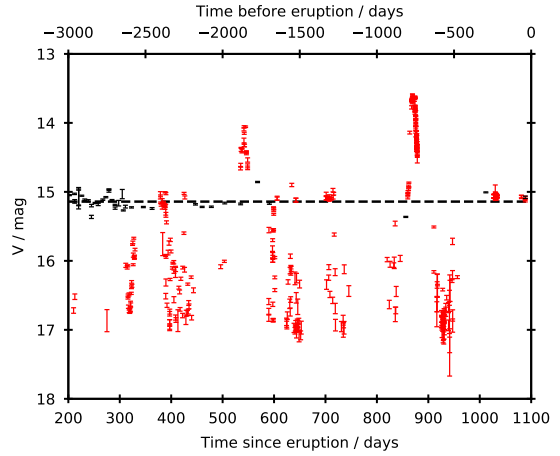
Figure 2. Comparison of post-nova (black) and pre-nova (red) V-band brightness of V392 Per. The average post-nova magnitude $\bar{V} = 15.2 \pm 0.1$ mag is shown by the dashed line. The time-scale for the pre-eruption AAVSO data from March 2004 to March 2018, which covers around 3 times the duration of the post-nova observations, is shown by the top time axis.

laws ($f \propto t^\alpha$) and a least-squares regression was employed to fit each light curve. Key parameters from the best fits are shown in Table A5. In general, the light curve exhibits an initial decline from maximum before entering a quasi-plateau after ∼ 5 days. The plateau continues for a further ∼ 5 days after which the decline steepens further and the light curve follows three broken power laws as it approaches an approximately flat luminosity ∼ 225 days post-eruption.

The onset, duration, and gradient of the plateau differs between the passbands; with a shallower gradient, later onset and longer duration with decreasing wavelength. Such plateaus have been proposed to be caused by a surviving, or reformed, accretion disk emerging from the optically thick photosphere as it recedes back toward the WD surface (Hachisu & Kato 2006; Henze et al. 2018). The behaviour here is compatible with a cooler outer disk emerging from the receding photosphere earlier than the inner hotter regions.

There is a potential light curve discontinuity during the first Sun constraint. The B-band light curve is poorly sampled but appears continuous across the gap, but the $Vr'i'$ data point to a change in gradient during that Sun constraint, possibly hinting at a further plateau stage during the gap. Upon exiting the initial Sun constraint, the system had entered the nebular phase, with strong emission from [O III] 4363, 4959, and 5007 Å and He II 4686 Å present (see Section 4). These emission lines began to appear before the end of the Sun constraint and, due to their strengths, may have driven the changes observed in the B and V light curves.

The power-law indices in the initial decline in the BVr'-bands are $\alpha = -1.75 \pm 0.04$, -1.76 ± 0.07, and -1.78 ± 0.8, respectively. This appears in good agreement with the expected continuum from free-free emission from an optically thin plasma (also see Section 5.1 for discussion about the nature of the early-decline light curve). Other than the initial power law and the plateau, we do not ascribe any physical meaning to the power laws. We simply utilise these as a tool to calibrate the optical spectroscopy (see Section 4).

The light curves have remained broadly static at the post-nova luminosity since ∼ 225 days post-eruption, with $\bar{V} = 15.2 \pm 0.1$ mag. This is substantially brighter than the long-term quiescent minimum of ∼ 17 mag, and was referred to by Munari et al. (2020a) as 'sustained post-(eruption) brightening', see Figure 2.

3.5   Spectral Energy Distribution

The evolution of the spectral energy distribution (SED) of V392 Per is shown in Figure 3. The SEDs are derived from dereddened photometry through LT $u'BVr'i'z'$, and *Swift* uvw2, uvm2 and uvw1 filters. We have assumed the *Gaia* determined distance of 3.5 kpc and $E(B-V) = 0.7$ mag. All plots include the SED averaged over the post-nova period, $t \geq 223$ days post-eruption.

Since V392 Per emerged from the first Sun constraint, the SED shape has remained broadly constant, with the overall luminosity fading toward the post-nova average (black line), although the overall SED slope has gradually decreased: the SED has become redder. From day 194 post-eruption, the SED luminosity has remained very close to the average post-nova value. From day 84, the SED shows a persistent V-band bump, which seems to be driven by [O III] 4959+5007 Å emission. We propose that the SED from the u'-band and bluer is that of an accretion disk (see Section 5).

3.6   Orbital Period

The post-nova light curve of V392 Per shows clear and significant variation, see Figure 1 (i'-band) and Figure 2. There are three published periods for V392 Per:

Schmidt (2020) used Cousins I-band photometry collected over 78 days between 2019 December 22 and 2020 March 9 (effectively the same period as Munari et al. 2020a). The data were detrended by subtracting the nightly mean magnitude. Schmidt (2020) performed a discrete Fourier transform and Lomb-Scargle periodogram analysis, yielding a period of $P = 0.06600 \pm 0.00002$ days.

The Munari et al. (2020a) period was calculated using ANS Collaboration VRI data taken over 17 nights between 2019 December 30 and 2020 March 11. The Fourier power spectrum of these data revealed two significant, potentially linked peaks, $P = 3.4118$ days and $P = 1.4107$ days (both illustrated in Figure 4). Consideration of the pre-nova photometry and derived system parameters led them to favour the longer period. Munari et al. notes that their R and I-band data show similar periodic modulation.

Schaefer (2021) utilised 1150 TESS observations from 2019, with 28725 supplementary AAVSO observations from 2019–2021, and, following cleaning and detrending, employed a Fourier technique and folded light curve fitting to estimate $P = 3.21997 \pm 0.00039$ days, with an amplitude of 0.122 magnitudes. However, the TESS CCD scale ($21''$ pixel^{-1}) would prohibit the disentanglement of signals from V392 Per and the nearby, similar luminosity, field star (standard #15; $9''$ distant). Some AAVSO observers were unable to separate these two sources as the nova faded. Munari, Moretti & Maitan (2020b) find the neighbour star shows no variability; our photometry of this source concurs.

We collected 423 high-cadence observations in the i'-band using LT and LCOGT between 2019 November 17 and December 2. These data show variation with amplitude up to ~ 0.7 mag over the course of a night, much greater than reported by Munari et al. or Schaefer. The left panel of Figure 4 shows the Lomb-Scargle power spectrum for all our i'-band observations taken after day 252, during the roughly consistent brightness post-nova phase, and we also show the associated window function. The periods reported by Munari et al. (2020a) and Schaefer (2021) are indicated on the power spectrum. The strongest significant peak is found at $P = 1.62419 \pm 0.00069$ d, when utilising a single (sinusoidal) Fourier term; this is very close to half the Schaefer (2021) value. Adding a second sinusoidal term reveals an additional peak at $P = 3.2297 \pm 0.0027$ days, very close to Schaefer's. The right panel of Figure 4 presents our i'-band

data folded around $P = 3.2297$ days. Here, upon visual inspection, there does appear to be a plausible phase-folded light curve that is compatible with a double-dipping CV. However, the folded light curve appears 'noisy', and we suggest that this may be due to different periodic, or other, activity from the system.

3.7   Optical spectra

Our LT and Hiltner 2.4 m flux calibrated and dereddened spectra are shown in Figures 5–7. Those shown in Figure 5 were taken before V392 Per entered the initial Sun constraint, and cover the period of early spectral evolution, while the spectra were declining in optical thickness. The strongest features in the earliest spectrum (2.1 days post-eruption; 1 day post-maximum) are H I Balmer series lines, with Hα–Hδ exhibiting broad, optically thick, P Cygni profiles. All lines attributable to the eruption have P Cygni shapes. We see strong lines from He I 4471 Å, in particular, and from He I 4388 Å and 4438 Å. Lines from Fe II multiplet 42 are dominant features. A broad Na I-D profile is punctuated by saturated interstellar absorption lines (see Section 3.3). In the second spectrum (4.9 days post-eruption), we also see He I 6678 Å, 7065 Å, and 7281 Å. In addition, lines from O I 7774 Å, 8227 Å, and 8446 Å were present (but not shown in Figure 5). All spectra before the initial Sun constraint exhibit these lines, but their intensity and optical depth diminishes over this first week of evolution, and the line profiles evolve from P Cygni profiles to triple-peaked structures (also see Darnley et al. 2018a; Mugrauer et al. 2018; Tomov et al. 2018; Wagner et al. 2018). Based on the spectral morphology, we would place this eruption in the Fe II taxonomic class, although the inferred ejecta velocities are higher than normally seen in spectra from this class.

Once V392 Per became visible following the first Sun constraint (76 days post-eruption), the spectra had transitioned to the nebular phase (see Figure 6; Darnley 2018a). We see the continued presence of Balmer and He I emission; however, the spectra are dominated by nebular [O III] 4959+5007 Å and auroral [O III] 4363 Å lines, with He II emission (particularly at 4200 Å and 4686 Å) now also present. As reported by Darnley (2018b), the [O III] 5007 Å line rivals Hα in brightness, and [O III] 4363 Å and He II 4686 Å are stronger than Hβ. The forbidden lines are double-peaked, whereas the H I and He I lines retain the triple-peaked structure, and the widths of the forbidden lines are consistent with those of H I. The final set of spectra are shown in Figure 7. Here we witness the decline of the nebular emission and the transition to the post-nova spectrum. Emission from the [O III] lines fades relative to that from He II 4686 Å and H I.

As first reported by Munari & Ochner (2018), we also see evidence for [Ne III] 3869 Å in the Hiltner and LBT spectra taken on days 132, 146, 189 and 220 post eruption. However, we do not see evidence for [Ne IV] 4715 Å. This line might blend with the He II 4686 Å profile, but we link the structure seen at ~ ±2000 km s^{-1} around He II to a contribution from the ejecta (see Section 4.4).

3.8   *Swift* X-ray and UV observations

Swift observations commenced as soon as V392 Per emerged from the first Sun constraint on 2018 July 20 (Darnley et al. 2018b). The *Swift*/UVOT photometry is shown in Figure 1. Although starting much later, the near-UV light curves match the late decline and approximately flat post-nova phases seen in the optical. There is a slight upward trend in the near-UV brightness during the post-nova phase. The system is consistently fainter through the uvm2 filter (which lies between the uvw1 and uvw2 filters, and samples the
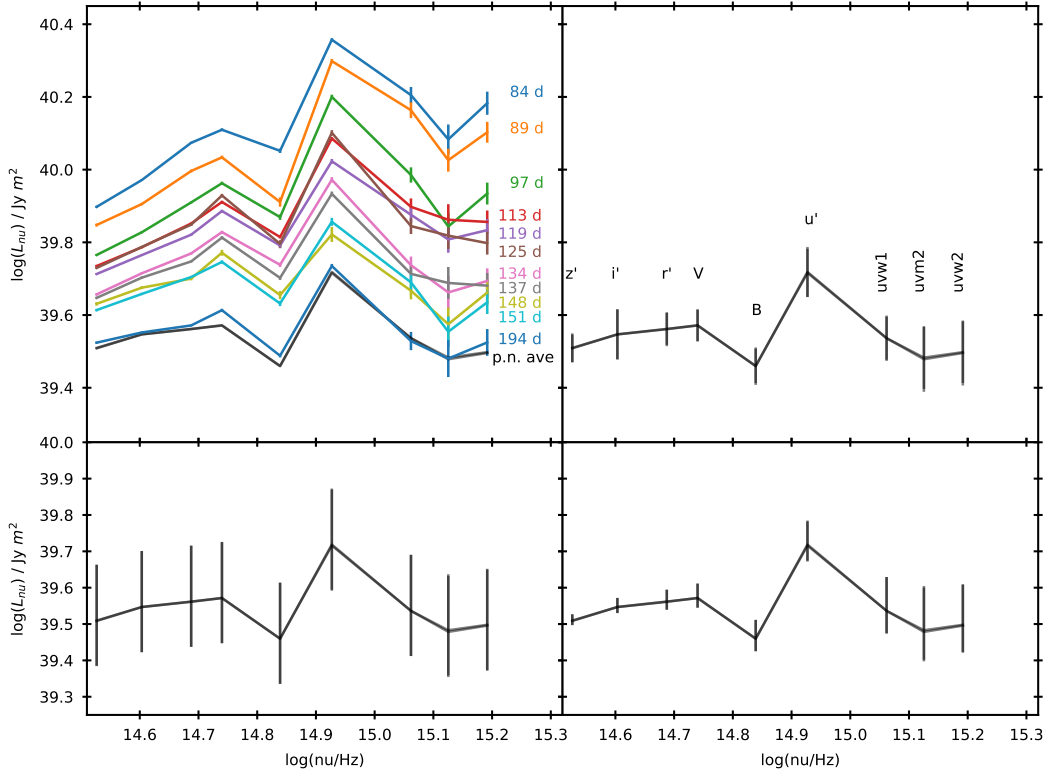
Figure 3. Spectral energy distribution (SED) evolution of V392 Per. **Top left**: Evolution between days 84–194, and the average post-nova (p.n. ave) SED, from day 220 and beyond, is shown in black at the bottom. **Top right**: Average post-nova SED, error bars indicate 1σ scattter. **Bottom left**: Distance uncertainty, $d = 3.5^{+0.6}_{-0.5}$ kpc **Bottom right**: Extinction uncertainties, $E(B-V) = 0.70^{+0.03}_{-0.02}$.
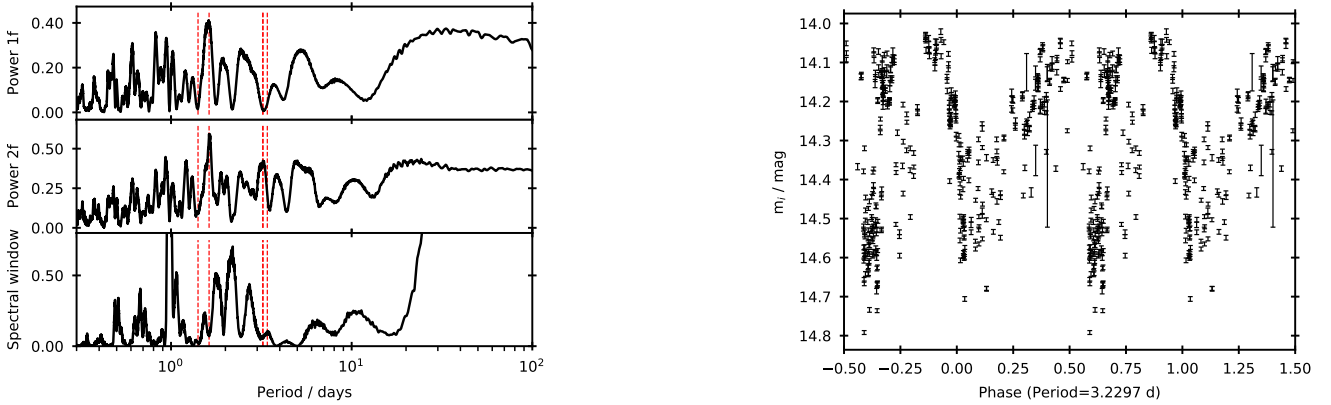
Figure 4. Top left: Power spectrum of post-nova i'-band observations using a single Fourier sinusoidal term. **Middle left:** As top left, but utilising two Fourier terms. **Bottom left:** Window function power spectrum. In all three panels the vertical red dashed lines indicate the reported periods, from left to right: $P = 1.4107$ days (Munari et al. 2020a); $P = 1.62419 \pm 0.00069$ d (this work); $P = 3.21997 \pm 0.00039$ days (Schaefer 2021); $P = 3.2297 \pm 0.0027$ days (this work; indistinguishable from Schaefer 2021); and $P = 3.4118$ days (Munari et al. 2020a). **Right:** Post-eruption i'-band light curve, folded on best fit period of $P = 3.2297$ (± 0.0027) days.

2175 Å 'bump' in the interstellar extinction curve), suggestive of high extinction.

The *Swift*/XRT light curve is presented in the left-hand panel of Figure 8. The plot at the top (black) shows the XRT count rate. A rapid decline in counts is seen from days 83–97, after which the counts remain approximately flat until entry into the second

Sun-constraint. Upon exiting the second constraint, the XRT counts remained slightly elevated. The X-ray HR [defined as counts (0.8–10 keV) / counts (0.3–0.8 keV)] is shown in the bottom panel (red). The HR is approximately constant (although slightly decreasing) from day 112 onward. However, the HR at day 83 is clearly lower (softer), and between days 83–97 there is a gradual hardening. Here
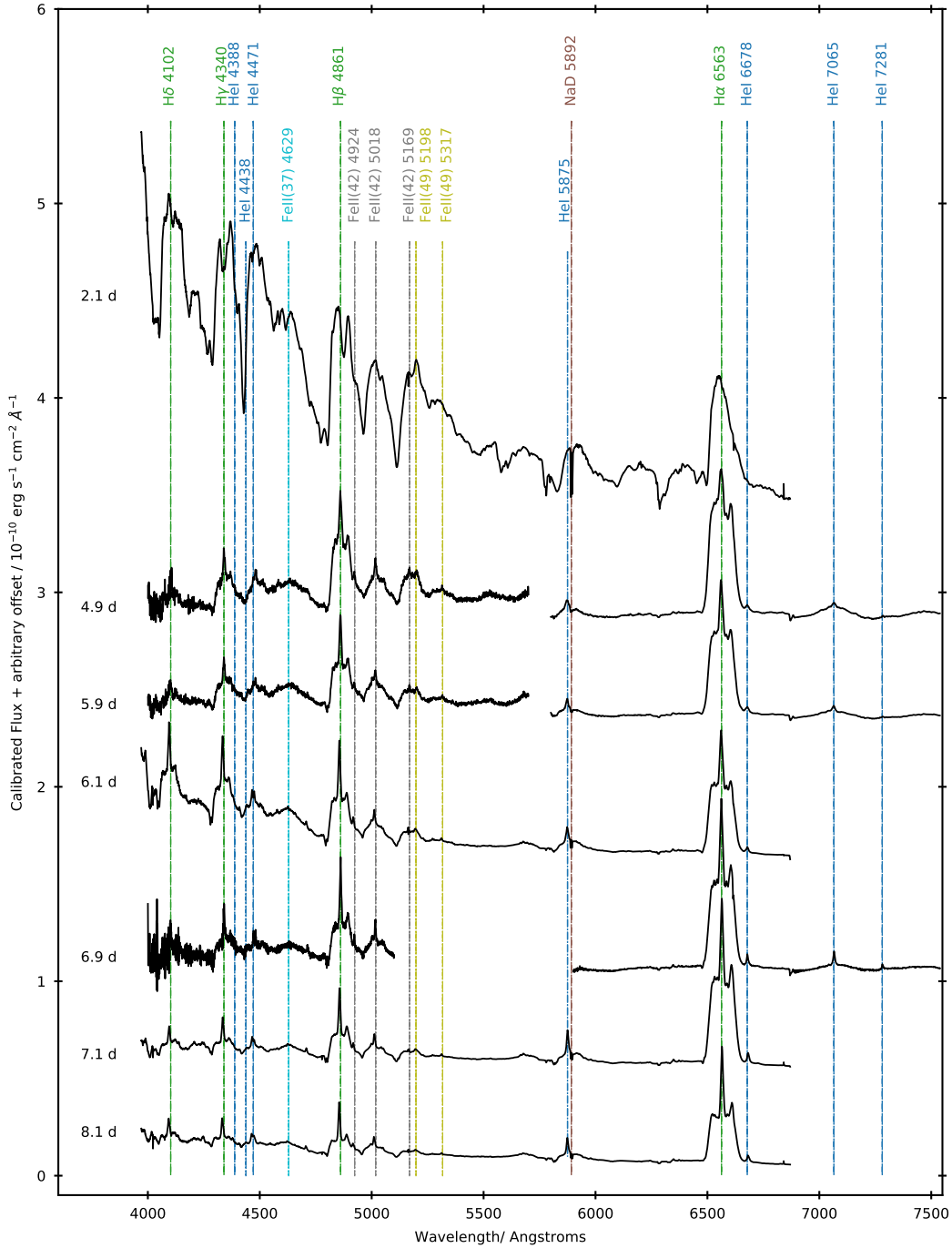
Figure 5. Pre-first Sun constraint spectra of V392 Per, from 2.1–8.1 days post-eruption. Here we present flux calibrated (but offset) dereddened spectra from the LT (SPRAT and FRODOSpec) and the Hiltner 2.4 m. These early spectra are becoming progressively less optically thick. Prominent spectral features are labelled. Spectra are available online.

we propose that the softer emission seen between days 83–97 is the tail of the super-soft source (SSS) phase of V392 Per.

The right panel of Figure 8 presents a comparison between the *Swift*/UVOT uvw2 lightcurve and the XRT light curve; here the final decline in the near-UV is particularly evident. From ∼ 300 days post-eruption, the XRT count rate and uvw2 photometry appear roughly correlated. This suggests that the post-nova near-UV and X-ray emission have a similar origin.

4 SPECTRAL ANALYSIS

4.1 Balmer lines

High resolution Hα line profiles are shown in Figure 9, which presents Hiltner 2.4 m and the LT/FRODOSpec data. Our earliest spectrum (2.1 days post-eruption; Figure 9 top-left) reveals a single-peaked, optically thick, broad and asymmetric Hα line, with P Cygni absorptions at $-2560\,\mathrm{km\,s^{-1}}$ and $-4550\,\mathrm{km\,s^{-1}}$, and emission on
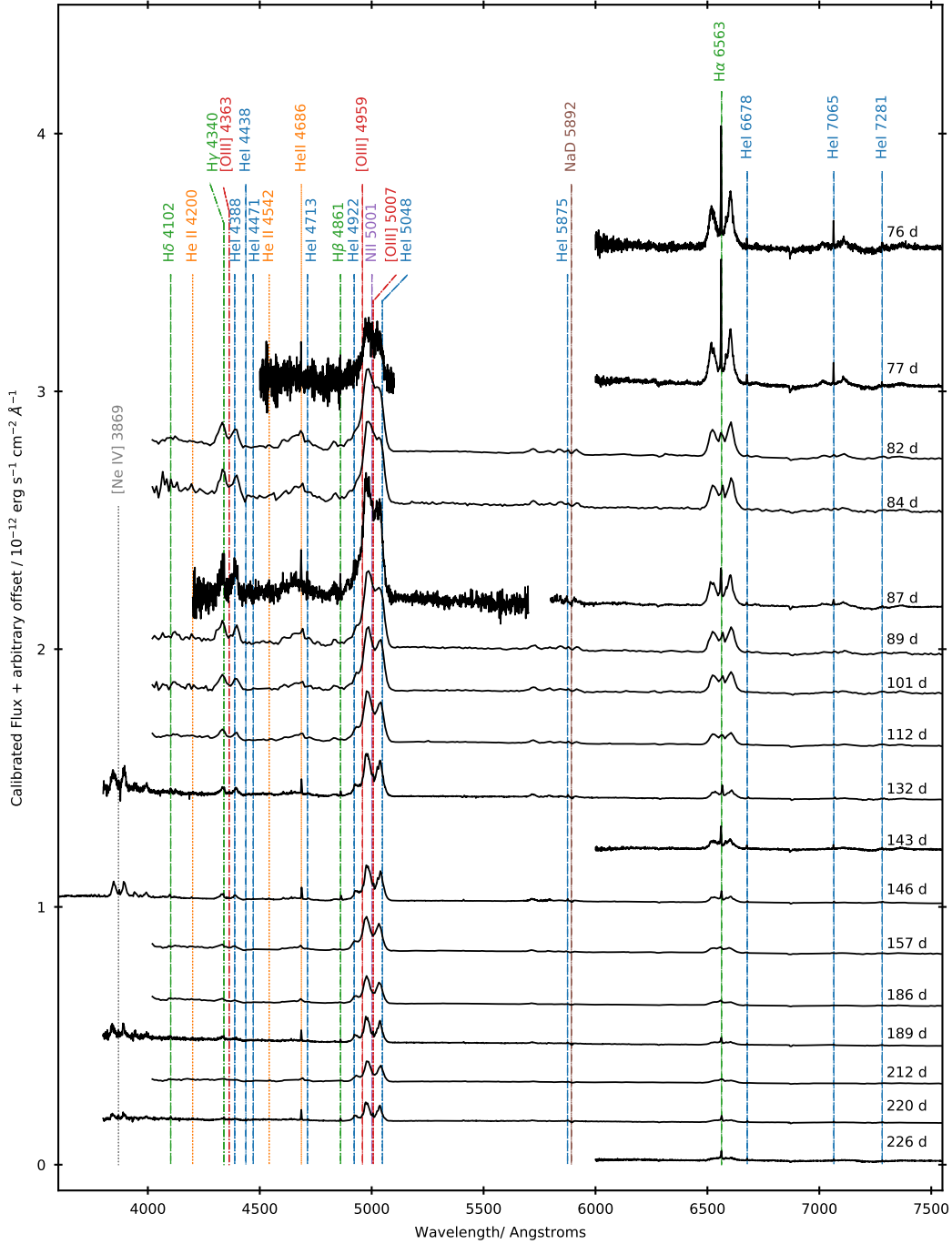
Figure 6. As Figure 5, displaying spectra from 76–226 days post-eruption and the nebular phase. Spectra are available online.

the red side out to $\sim 5000\,\mathrm{km\,s^{-1}}$. By the next spectrum (4.9 days post-eruption) the profile has developed a stronger and narrower central peak, and additional secondary peaks have started to develop at $\sim\pm2500\,\mathrm{km\,s^{-1}}$, the P Cygni absorption elements have weakened and possibly merged (see Section 4.2), and the high velocity redward wing has gone. Over the next week, as V392 Per approached the first Sun constraint, the central peak increased in intensity relative to the red- and blue-shifted secondary peaks, with the redward peak more sharply defined than its blue counterpart.

The subsequent spectrum was taken once V392 Per emerged

from the first Sun constraint, on day 76 (Figure 9 top-right). By this time the system had evolved to the nebular phase and the Hα line profile transitioned to a clear three-peaked structure with a bright, very narrow, central peak with measured FWHM of $57\,\mathrm{km\,s^{-1}}$. The velocity structure of the outer peaks are symmetric, but the redward peak is brighter. This morphology persisted until 220 days post-eruption, but the outer peak amplitude continued to weaken relative to the central peak.

From day 226 post-eruption (Figure 9 bottom-left), the amplitude of the central peak began to dominate and emission from the
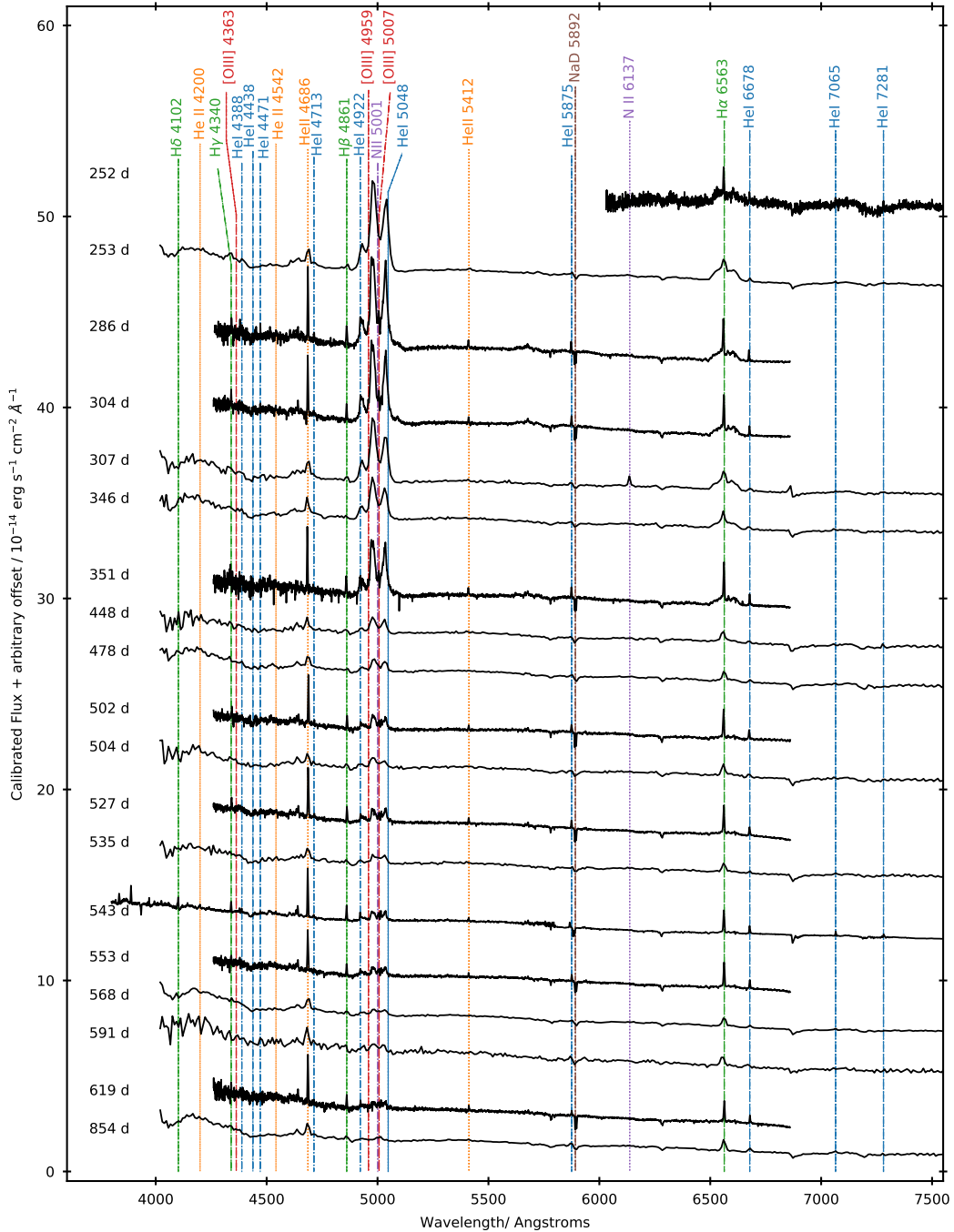
Figure 7. As Figure 5, displaying spectra from 252–854 days post-eruption, showing the transition from the late-nebular phase to the post-nova phase. Spectra are available online.

outer peaks began to wane more rapidly at higher velocities: the outer peaks appear to move inward toward the central peak – most likely an effect of decreasing emissivity as the ejecta thin. The fastest moving ejecta thin the fastest. As the outer peak flux decreased, nearby lines became more prominent, e.g., He I 6678 Å (+5165 km s^{-1}). Between days 351–448 (see Figure 7) all high velocity elements had disappeared, leaving just the narrow central line (Figure 9 bottom-right) — the post-nova profile.

In Figure 10 we compare the Hα profile with those of Hβ and Hγ. As expected, the Balmer line profiles evolve broadly similarly.

The P Cygni absorptions persist for longer in Hβ and Hγ, possibly up to day 7.1 (see Section 4.2). The central peak is stronger relative to the outer peaks in Hβ and Hγ than in Hα. This suggests there may be different recombination conditions in different ejecta components or stronger self-absorption in those components – both indicative of a complex geometry. During the nebular phase, Hβ and Hγ are severely blended with, and dominated by, the nebular and auroral [O III] lines, respectively. By the post-nova phase all three Balmer lines simply show a very narrow peak.

The Hα profile remains isolated from other lines and is one of
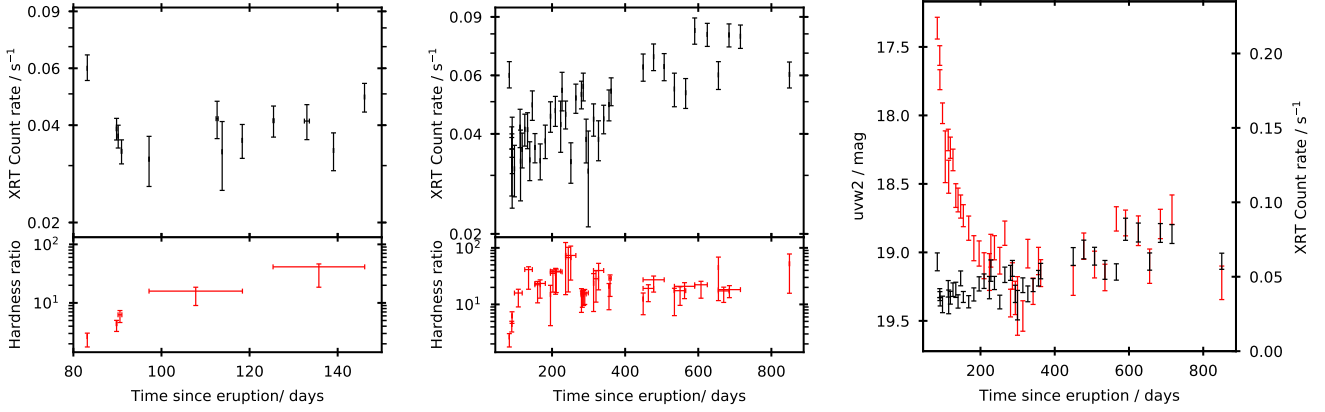
Figure 8. Left and centre: *Swift*/XRT observations of V392 Per. The upper panel shows the count rate, the lower panel shows the hardness ratio: counts(0.8–10 keV) / counts(0.3–0.8 keV). **Right:** *Swift*/XRT count rate (black) compared to the *Swift*/UVOT uvw2 photometry (red).
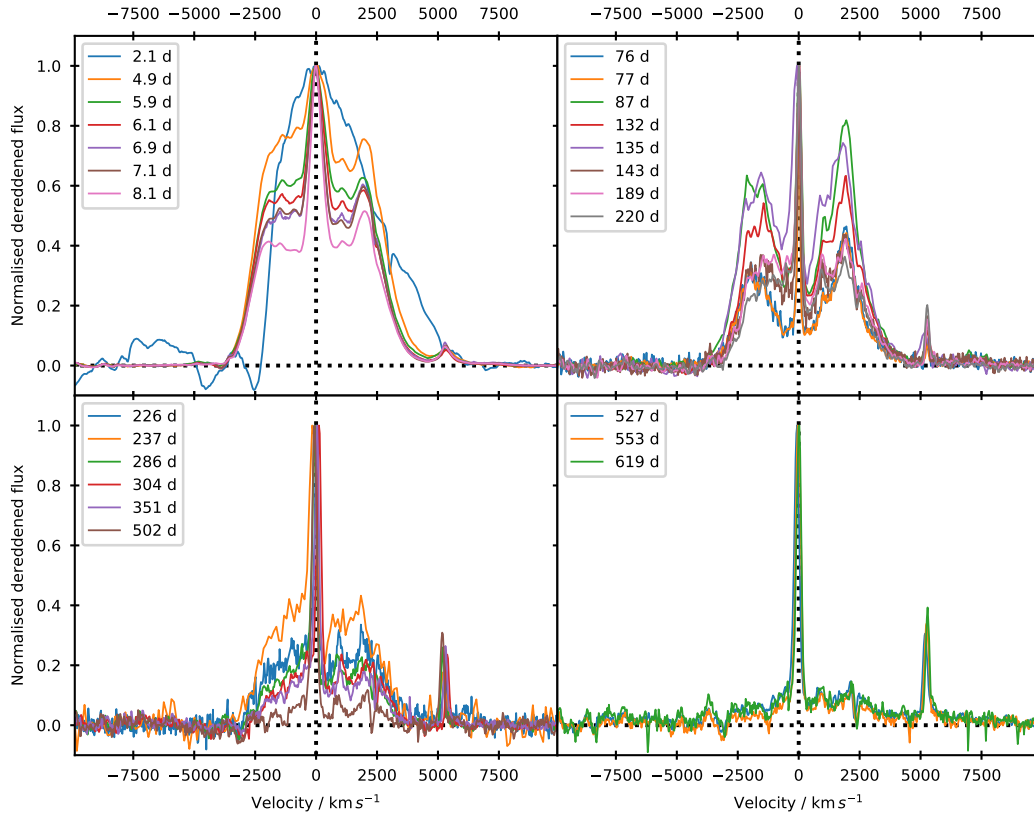
Figure 9. High resolution Hα line profiles from Hiltner OSMOS and FRODOSpec spectra. The spectra have been normalised to the flux of the Hα central peak. The horizontal dotted lines indicate a normalised dereddened flux value of 0. The vertical dotted line shows the rest wavelength of Hα.

the strongest lines in the spectra at all times, whereas other bright lines, e.g., other H ɪ, He ɪ-ɪɪ, and [O ɪɪɪ], were often severely blended. Thus, to measure the flux of the emission lines we used a triple-Gaussian profile, modelled around the Hα profile at each epoch, to estimate line fluxes and, where necessary, de-blend lines. Line fluxes are tabulated in Tables A7 and A8.

The flux evolution of the Hα line profile is shown in Figure 11 (left). Although the high amplitude of the central peak had appeared

to dominate from day 226, here we see that the integrated emission from the outer peaks (blue and red) dominates the overall line flux (brown) until day ~ 600. The decline of the outer peak fluxes are well described by a power-law with index −2.32 ± 0.04. The decay of the central peak (black) is steeper than the outer peaks and power-law-like until day ~ 100, however, from this point the central peak tends towards a constant flux of $(2.90 \pm 0.42) \times 10^{-12}$ erg s^{-1} cm^{-2}. Here we suggest that there are two system components contributing to the
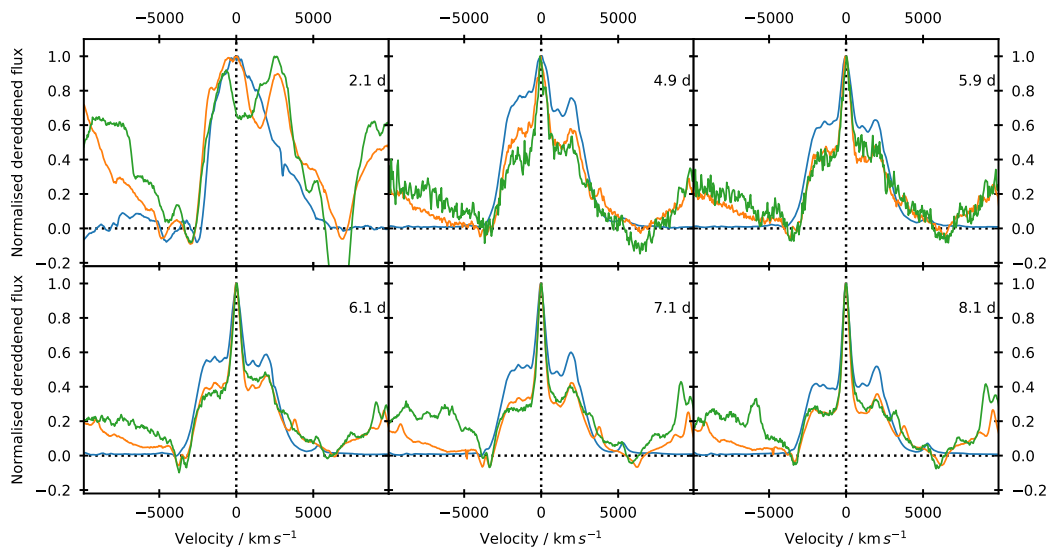
Figure 10. Comparison of Hα (blue), Hβ (orange), and Hγ (green) line profiles for pre-first Sun constraint epochs. Spectra have been normalised to the central peak flux.

Hα line, a triple-peaked ejecta profile, that decays as a power-law, and a constant single narrow peaked contribution from the central system. While the Hβ line is strong and isolated during the early spectra, once in the nebular phase the line is severely blended and dominated by [O III] 4959+5007 Å. As such, we can only reliably estimate the Hβ flux until day ~350. As shown in Figure 11, the Hβ flux declines following a similar power-law to Hα.

4.2 Multiple ejections?

In Figure 12 we show the velocity evolution of detected P Cygni absorption components from the Balmer lines. For illustrative purposes, we also show the Fermi-LAT γ-ray light curve and 95th percentile upper limits (Chomiuk et al. 2021a; Albert et al. 2022). Here we also utilise the ARAS spectra, some of which included very high resolution data for the Balmer lines. The first Hα P Cygni measurement is 1.9 days post-eruption and yielded two components $\sim -3000\,\mathrm{km\,s^{-1}}$ and $\sim -5000\,\mathrm{km\,s^{-1}}$. The Hα P Cygni absorptions appear to shift further blueward over the next three spectra. By day 3.85, the Hα profile only revealed a single P Cygni absorption at $\sim -4000\,\mathrm{km\,s^{-1}}$, with subsequent measurements showing similar P Cygni velocities. Most of the later Hα line profiles only contain a single P Cygni absorption, but a higher resolution spectrum taken 7.8 days post-eruption indicated that the absorption contained sub-structure with similar nearby minima of $\sim -3800\,\mathrm{km\,s^{-1}}$ and $\sim -4000\,\mathrm{km\,s^{-1}}$. The overall structure of the Balmer lines is complex and this led to systematic difficulties in the P Cygni measurement, and as such the scatter seen in the Hα measures from day 5 onward, is indicative of the associated systematic errors.

The first Fermi-LAT γ-ray detection occurred 2.5 days post-eruption (one day post-discovery), the second detection a day later had less than half the flux of the first detection, and the γ-ray flux had almost halved again by day 4.5. During this period of rapid γ-ray fading, we observe the apparent merger of two P Cygni absorptions, leaving a single absorption line with a velocity intermediate to the two. This scenario is consistent with that reported in Aydi et al. (2020a,b) for V906 Car and other CNe, where two constituents of a

multi-component ejecta merge, with the associated shocks driving γ-ray emission. Here, we propose that an initial $\sim 3000\,\mathrm{km\,s^{-1}}$ ejection merges with a subsequent $\sim 5000\,\mathrm{km\,s^{-1}}$ ejection, leaving a single component travelling at $\sim 4000\,\mathrm{km\,s^{-1}}$. With this merger seemingly occurring 2.5 ± 0.5 days after the initial eruption, the second ejection would have occurred at 1.0 ± 0.3 days post-eruption, i.e. around the time of optical maximum. Assuming that kinetic energy is largely conserved during the merger, the second ejection could have a mass up to 80% that of the first.

The equivalent Hβ and Hγ data appear richer, both showing evidence for the initial merger that drove the strong γ-ray peak. From day 5, there remains evidence for two absorption features at lower velocities ($\sim -3750\,\mathrm{km\,s^{-1}}$ and $\sim -3250\,\mathrm{km\,s^{-1}}$). These are markedly lower than P Cygni velocities seen in the Hα profile during the same epochs, but we note that the Hα line was already transitioning to an optically thin emission profile at this time. These data are admittedly noisy, but they hint at a second or on-going merger event; which may be driving the flat γ-ray emission during this time. The spectral coverage ends at day 10, but in this final spectrum there is a hint of a single, merged, P Cygni at $\sim -3550\,\mathrm{km\,s^{-1}}$. We note that this corresponds to the final Fermi-LAT detection, although V392 Per remained visible to Fermi beyond this time.

4.3 He I 6678 Å and 7065 Å

The He I 6678 Å profiles were fitted simultaneously with the Hα, and are shown in Figures 9 and 10 at $\sim 5250\,\mathrm{km\,s^{-1}}$. The flux evolution of He I 6678 Å is shown in the right panel of Figure 11. Due to its proximity to Hα, only the central peak of the He I 6678 Å was measured, and emission peaked 4.9 days post-eruption at $(5.30 \pm 0.01) \times 10^{-9}\,\mathrm{erg\,s^{-1}\,cm^{-2}}$. The He I 6678 Å flux follows a power law with index -2.69 ± 0.16, declining to a plateau of around $(1.01 \pm 0.03) \times 10^{-12}\,\mathrm{erg\,s^{-1}\,cm^{-2}}$, from day 253 post-eruption.

As He I 7065 Å is isolated from other strong lines, the profile was modelled using a three component Gaussian, as for Hα. The evolution of the total flux of He I 7065 Å is shown in the right panel of Figure 11. The first flux measurement of He I 7065 Å was
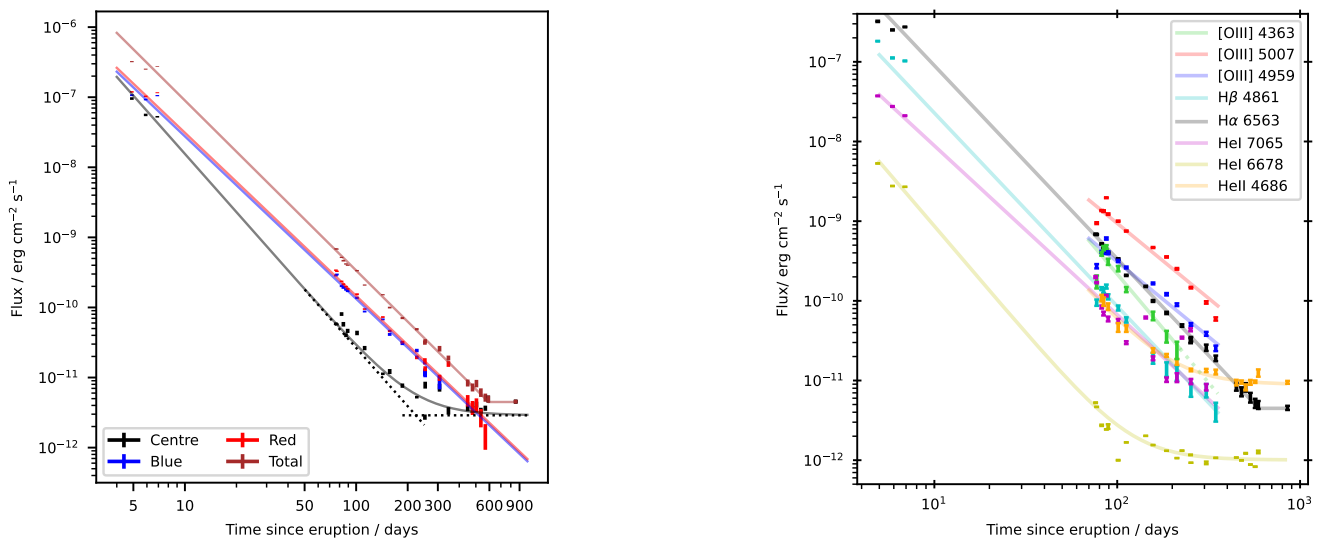
Figure 11. Left: Hα flux evolution from SPRAT and FRODOSpec spectra. The fluxes of the central, blueward and redward components are shown in black, blue and red, respectively. The total flux is shown in brown. **Right:** Flux evolution of prominent lines in the V392 Per spectra. Data for [O III] 4959 Å, [O III] 5007 Å, and Hβ are only shown up to day 346. The Hα flux from day 346 onward only includes the central and redward component, and for day 591 onward only the central component. Power law fits to these data are indicated by the solid lines, dotted lines are extrapolations of fits beyond the available data.
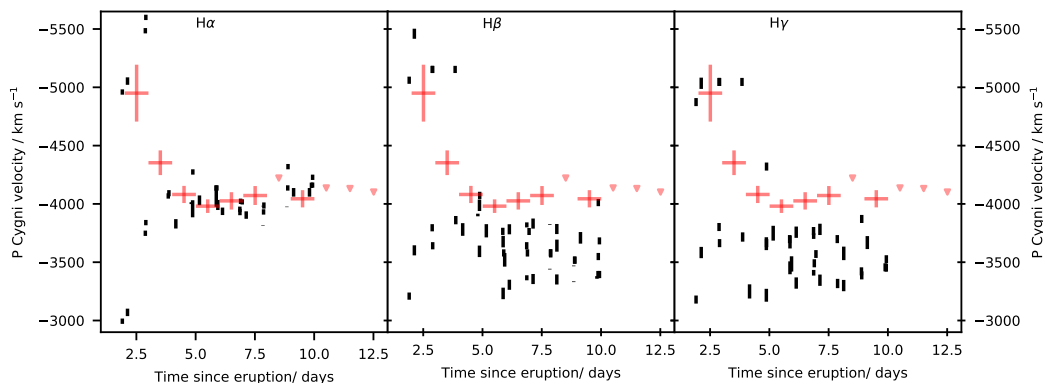
Figure 12. Velocity evolution of the Balmer line (left: Hα, centre: Hβ, right: Hγ) P Cygni absorption features (black). The red data points show the Fermi-LAT light curve for comparison, the red arrowheads are 95th percentile upper limits.

$(3.74 \pm 0.04) \times 10^{-8}$ erg s^{-1} cm^{-2}, 4.9 days post-eruption. The He I 7065 Å broadly follows a power law with index -2.12 ± 0.05, but there is no evidence for a flux plateau from the central component, as was seen in Hα and He I 6678 Å.

4.4 He II 4686 Å

He II 4686 Å normalized line profiles are shown in Figure 13 (left). The top panel shows profiles from the nebular phase following emergence from the initial Sun constraint 83–212 days post-eruption. During this stage, the He II emission strengthened relative to neighbouring permitted lines. The low resolution spectra are suggestive of broad He II emission associated with the nova ejecta, due to blending from neighbouring lines. However, the higher resolution data indicate that the He II emission is dominated by a narrow central peak, with hints of a faint, broad, contribution from the ejecta (± 2300 km s^{-1}) in spectra from days 132 and 189. The He II profiles toward the end

of the nebular phase and throughout the post-nova period, show only the narrow central peak.

Given the simplicity of the He II profile, we fitted the line using a single Gaussian. The flux evolution of He II 4686 Å is shown in Figure 13 (right). There is no significant detection of He II before the first Sun constraint. The first clear detection of He II occurs after emergence from this Sun constraint, on day 82. Here, the flux is $(1.09 \pm 0.10) \times 10^{-10}$ erg s^{-1} cm^{-2}. The evolution of the line flux is best described by the combination of a power law of index -2.54 ± 0.16 and a plateau of around $(9.02 \pm 0.37) \times 10^{-12}$ erg s^{-1} cm^{-2}. The flux evolution is compared with that of other species in Figures 11 (right), shown in Figure 13, and discussed further in Section 5.

4.5 Nebular [O III] 4959+5007 Å

The combined [O III] 4959+5007 Å nebular emission complex was visible from the initial post-first Sun constraint spectrum, and domi-
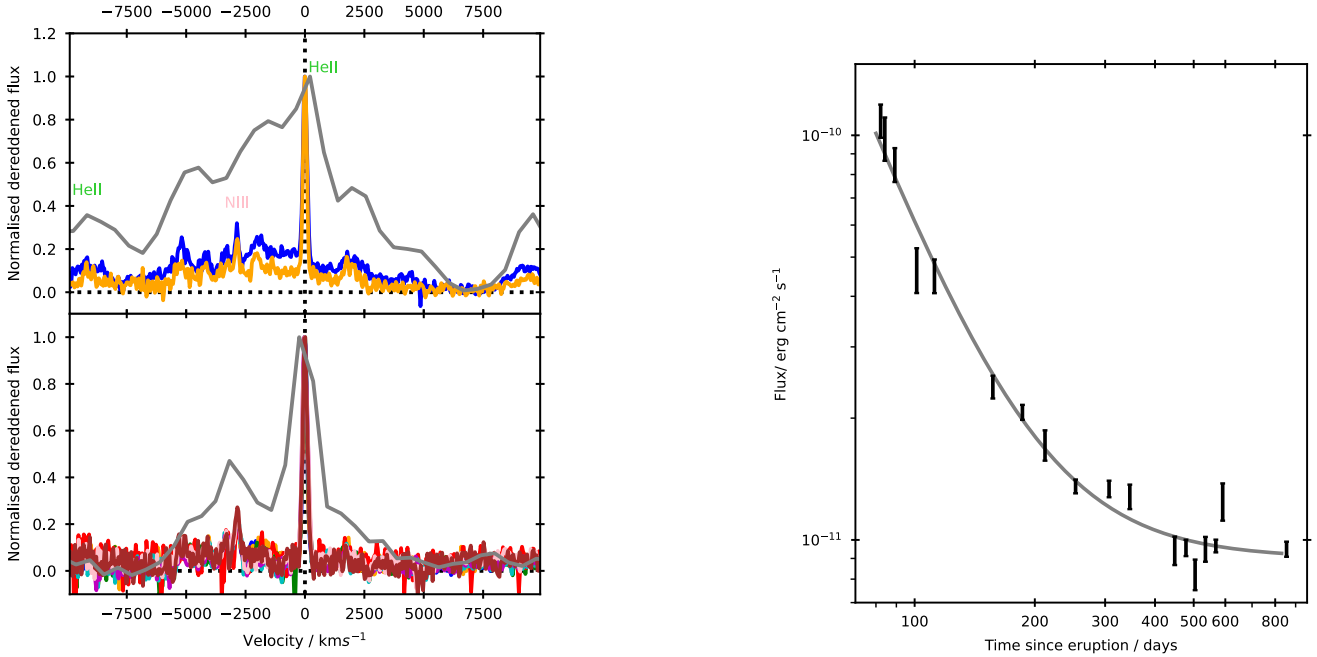
Figure 13. Left panels: He II 4686 Å line profile evolution: high resolution profiles are compared with time-averaged low resolution data (grey) from the same time interval. **Top:** spectra from 83–212 days post-eruption, high resolution data from 132 (blue) and 189 (orange) days post-eruption. **Bottom:** spectra from 253–854 days post-eruption. **Right:** He II 4686 Å flux evolution, where the solid line indicates a power-law plus plateau fit to the data.

nant throughout the nebular phase (see Figures 6 and 7). Although appearing to mirror the triple-peaked Hα profile, the [O III] complex consists of a pair of overlapping double-peaked line profiles, the brighter centred at 5007 Å the fainter at 4959 Å (see Figures 14 and 15). There is no evidence for a central component and, by this time, the central component seen in the permitted lines was only $\sim 60\,\mathrm{km\,s^{-1}}$ wide and therefore not associated with the ejecta.

The nebular [O III] flux was measured by modelling the 5007 Å component with a symmetric pair of Gaussians offset equally either side of the rest wavelength. The 4959 Å was simultaneously modelled by scaling the 5007 Å profile. The blueward peak from the 4959 Å profile overlaps with the redward outer peak of Hβ. Thus, to de-blend [O III] and Hβ, we included Hβ (based on the Hα profile) in the nebular [O III] model (see Section 4.1). In addition, we incorporated N II 5001 Å and He I 5016 Å lines using single Gaussians with widths matching the central Hα peak.

Figure 14 shows the evolution of the nebular [O III] 4959+5007 Å profile (days 77–212 post-eruption) as it transitions toward the 'frozen-in' state. Initially, the space between the two 5007 Å peaks was 'filled' by emission from N II 5001 Å and He I 5016 Å. As the relative strength of [O III] increased the impact of N II and He I diminished.

The left hand panel of Figure 15 presents the nebular [O III] profile in higher resolution. The top plot shows the pre-frozen evolution seen in Figure 14. The middle plot shows the frozen-in phase between days 220–351. The bottom plot (days 448–854) shows weakened [O III] (blue; with N II, He I, and Hβ again evident). Here, the orange line shows the low resolution profile obtained 854 days post-eruption, when [O III] was no longer detectable.

The flux evolution of [O III] 4959 Å and [O III] 5007 Å is shown in Figure 11. The first flux measurements are from day 77, yielding $(2.72 \pm 0.17) \times 10^{-10}\,\mathrm{erg\,s^{-1}\,cm^{-2}}$ and $(9.45 \pm 0.26) \times$

$10^{-10}\,\mathrm{erg\,s^{-1}\,cm^{-2}}$ for 4959 Å and 5007 Å, respectively (a ratio of 3.5 ± 0.2). We fit the flux of both the 4959 Å and 5007 Å contributions by linking both to a power law with index -1.88 ± 0.10. From day 346, the rate of decline steepened and the flux ratio between the components began to decrease.

4.6 Auroral [O III] 4363 Å

Similar to its nebular cousins, auroral [O III] 4363 Å was visible in the initial post-first Sun constraint spectra, and this emission rivalled the Hα line. The line profile evolution is shown in the right-hand panels of Figure 15. The top plot presents days 82-212 and, unlike the nebular lines, the auroral profiles are already frozen-in. The signal-to-noise for the auroral profile rapidly diminished, as such, the middle and bottom panels simply show time averaged low- (red) and high-resolution (grey) spectra between days 220–351 and 448–854, respectively. While the low-resolution spectra suggest changes in the relative intensity of the two components, in the high-resolution spectra (days 220–351) we see that the auroral structure has faded with narrow Hγ emission becoming more dominant. By the post-nova phase, evidence for auroral [O III] has largely disappeared leaving just the narrow Hγ line.

The [O III] 4363 Å flux was measured by fitting the profile with a similar model to [O III] 5007 Å combined with a Hα-based profile for Hγ. We also incorporated He I 4388 Å emission using a single Gaussian matched to the width of the Hα central peak. The flux measurements for [O III] 4363 Å are shown in Figure 11. The first measurement (day 77) yielded $(1.76 \pm 0.33) \times 10^{-10}\,\mathrm{erg\,s^{-1}\,cm^{-2}}$, with the flux evolution described by a power law with index -2.72 ± 0.46.
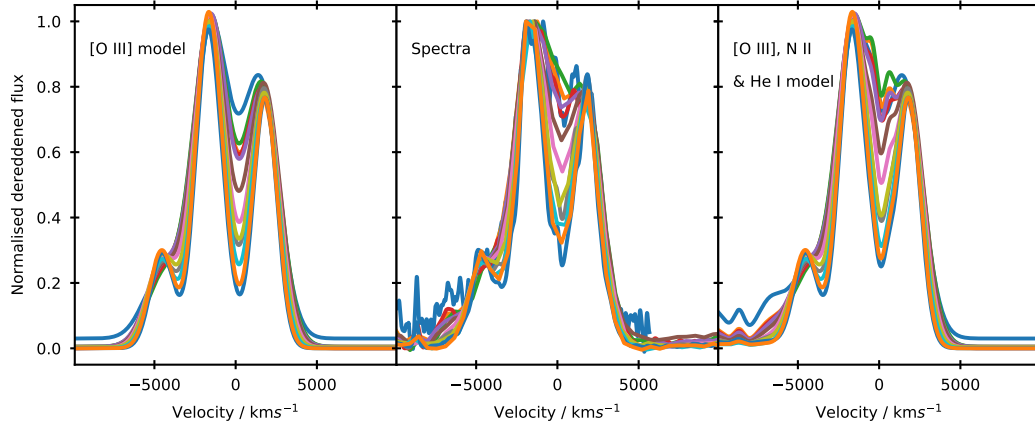
Figure 14. Evolution of the [O III] 4959+5007 Å profile from days 77–212 post-eruption. **Centre:** observed line profiles. **Left:** [O III] line profile models. **Right:** [O III] models including emission from N II 5001 Å, He I 5016 Å, and Hβ (−8727 km s^{-1}).
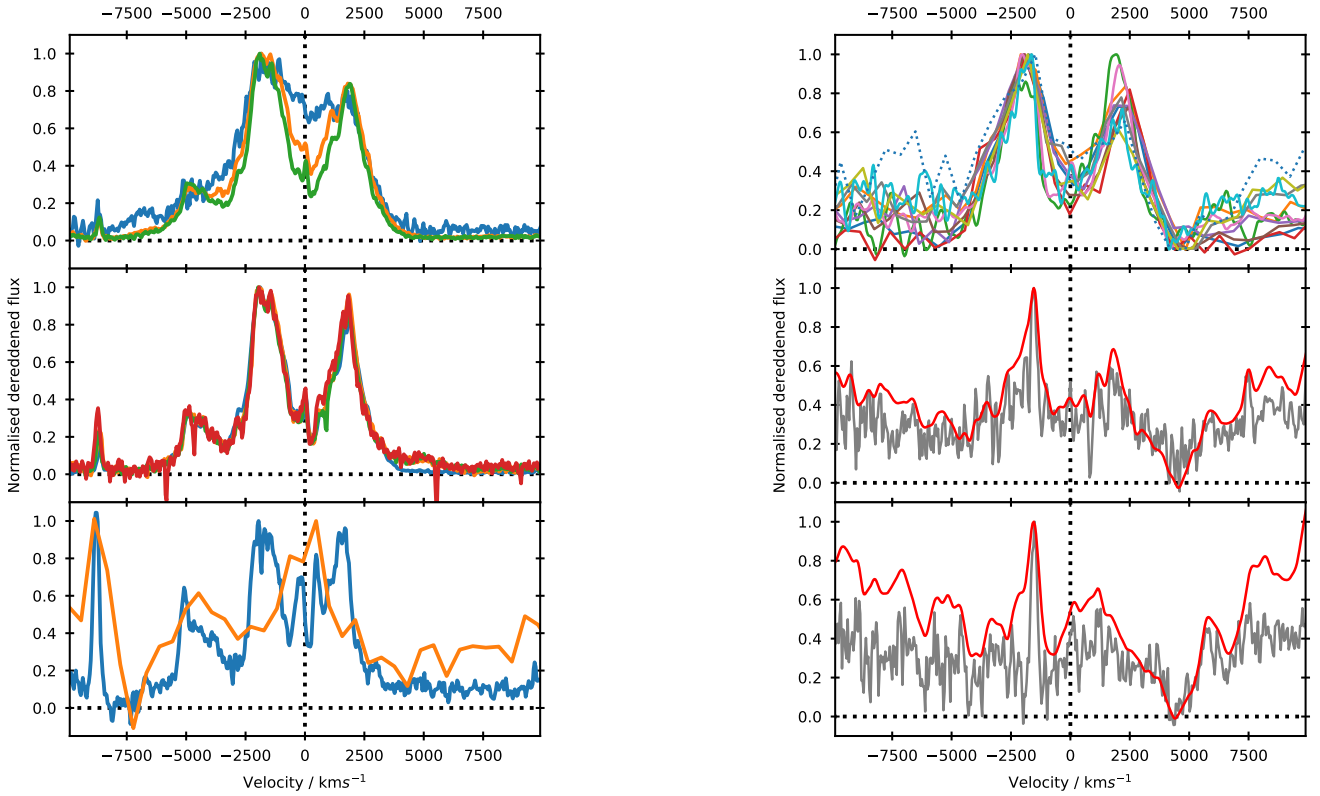
Figure 15. Left: Evolution of the high resolution [O III] 4959+5007 Å profile. Top panel, showing the transition to the 'frozen-in' state (as shown in low resolution in Figure 14). The middle panel shows profile 'frozen-in' between days 220-351 post-eruption. The bottom panel shows time-averaged data for the late nebular phase (blue), where Hβ (−8727 km s^{-1}) is now similar in strength to [O III] 5007 Å. The orange line shows the post-nova data from day 854, here only He I 5016 Å remains. **Right:** [O III] 4363 Å low resolution profile evolution, SPRAT data are shown at their native resolution, while Hiltner 2.4 m data have been Gaussian smoothed to match. The top panel shows data from days 82–212, where the profile is frozen-in. The middle and bottom panels show the average profile between days 220–351 and 448–854, respectively for the low resolution (red) and high resolution (grey) spectra. By this time, Hγ has reasserted its dominance (at ∼ −1600 km s^{-1}).

4.7 Other P-class neon novae

Four P-class novae listed in Strope et al. (2010) showed neon lines in their spectra, and their t_2 decline times ranged from 1 day (V838 Her) to 20 days (QU Vul). Fe II emission was present in the early spectra of QU Vul (Rosino et al. 1992) and V1974 Cyg (Chochol et al. 1993; Rafanelli et al. 1995). There was no mention of Fe II in the spectra of V838 Her (Vanlandingham et al. 1996), and spectra of V351 Pup were only available from 136 days after eruption (Saizar et al. 1996). Expansion velocities decreased with decline time, and ranged from $1700 - 4200 \, \text{km} \, \text{s}^{-1}$, with double P Cygni profiles evident in the Balmer lines in early spectra of QU Vul, V1974 Cyg and V838 Her (Chochol et al. 1993; Rafanelli et al. 1995; Rosino et al. 1992; Vanlandingham et al. 1996). V1974 Cyg is a proposed magnetic CV, with $P = 0.08 \, \text{d}$ (Chochol et al. 1997). During the early evolution, there are no substantial differences between the spectra of these four and V392 Per. However, there is no evidence for similar late-time, narrow-line, behaviour in these systems (see Section 5.2).

4.8 X-ray spectral modelling

Figure 16 shows *Swift*/XRT spectra from four epochs. For each epoch the upper panel shows the data (black) and best fit model (red), while the lower panel shows model residuals as a ratio. The XRT spectra were fitted using a combination of a black-body and collisionally excited plasma (APEC) components, where appropriate. All spectra were modelled using a fixed column ($N_{\text{H}} = 4.8 \times 10^{21} \, \text{cm}^{-2}$; equivalent to $E(B - V) = 0.7$, converted using Equation 1 from Güver & Özel 2009). Table 2 summarises the results of the fitting. We note that if N_{H} were permitted to vary freely, larger values ($\sim 10^{22} \, \text{cm}^{-2}$) were obtained (see Section 5.2). The choice of column makes little difference to the resulting findings.

The spectra at the top of Figure 16 show the XRT data taken 83 days post-eruption (left) and the combined spectra between days 89–97 (right), both taken after exiting from the first Sun constraint. On day 83, the count rate was $0.06 \, \text{s}^{-1}$ and the spectrum was relatively soft, with a HR of 2.7. By days 89–97 the count rate had dropped to $0.035 \pm 0.003 \, \text{s}^{-1}$, and the HR had hardened to 4.4 and then to 6.3. These spectra correspond to the first three data points in Figure 8 and are the softest X-ray spectra taken of V392 Per. These first two spectra show clear count rate excesses at low energies and, as such, we fitted the earliest spectrum using the combination of a black-body ($k_{\text{B}}T = 62^{+17}_{-14} \, \text{eV}$) and hot plasma, APEC, component. The day 89–97 spectra required an additional and hotter APEC component to account for the emission $> 5 \, \text{keV}$ that is not seen in the day 83 spectrum, likely due to the shorter integration. Given these spectra, the declining soft X-ray flux during this period, and the optical spectra at the time, we conclude that we are observing the tail of the super-soft source stage of V392 Per, and that the SSS ended at $97 \, \text{d} < t_{\text{SSS,off}} < 112 \, \text{d}$. The spectra at the bottom of Figure 16 show the XRT data between days 112–361 (left) and 449–849 (right). These are harder and clearly lack the SSS component. Here, both spectra are modelled using a pair of APEC components, with the best fit temperatures unchanged between the two epochs, although the count rate is higher at later times.

5 DISCUSSION

V392 Per is the first pre-known DN to be observed as a γ-ray bright CN. Here, we aggregate our reported observations to present a plausible description of the underlying system.

5.1 A shock-powered light curve?

The Fermi-LAT detection of γ-ray emission from V392 Per (Albert et al. 2022) followed soon after the optical detection. However, γ-ray emission might have been detected earlier were it not for technical problems with Fermi. In Figure 17 we directly compare the Fermi-LAT flux (from Albert et al. 2022) with the V-band flux (see Section 3.4). As has been reported for other γ-ray novae (Ackermann et al. 2014; Aydi et al. 2020a), there appears to be a clear correlation between the γ-ray and optical emission during the early evolution.

The early γ-ray and optical declines both follow similar power-laws until day ~ 5, when both fluxes plateau. As the optical plateau ends (day ~ 10) and the decline resumes, the Fermi-LAT detections cease (although observations continued). Here, we propose that the early (pre-first Sun constraint) optical light curve is driven by the evolution of shocks between and within multiple mass ejection components (as discussed in Gordon et al. 2021):

As reported in Section 4.2, there is evidence for multiple mass ejections, an initial event with $v \sim 3000 \, \text{km} \, \text{s}^{-1}$ being swept up and shocked 2.5 d post-eruption by a faster ejecta at $v \sim 5000 \, \text{km} \, \text{s}^{-1}$ — corresponding with the initial Fermi-LAT detection. These shocks will have accelerated ions to relativistic velocities, which emitted γ-rays while interacting with particles or photons in the surroundings (Martin et al. 2018; Aydi et al. 2020a). While γ-ray emission from novae can also be linked to the ejecta shocking and sweeping up pre-existing circumbinary material (e.g., a red giant wind; Cheung et al. 2014), here we see no evidence for the associated coronal emission lines (Rosino & Iijima 1987) or sustained bulk ejecta deceleration expected in such cases (Bode & Kahn 1985; Darnley et al. 2016). As such, we propose that the most likely source of the initial γ-ray emission is inter-ejecta shocks between these two components. With the lack of very early optical data, evidence for an additional, earlier, light curve peak corresponding to the initial ejection is unavailable.

The spectral evolution during the initial plateau is complex, and is additionally challenging due to the decreasing optical depth likely to be simultaneously occurring. The light curves of many novae enter quasi-plateau phases around t_3. For the recurrents, this has been proposed to be driven by a surviving, or rapidly reformed, accretion disk emerging from the receding photosphere, with the unveiling of the SSS occurring toward the end of the plateau as the inner disk is revealed. However, unlike recurrent nova plateaus (e.g., Henze et al. 2018), here we see no evidence for He II emission during the plateau – which would be expected from a disk. Indeed, He II emission is only seen after the first Sun constraint during the nebular phase. The plateau corresponds with the end of the clear 'bulk' ejecta merger, but there remains evidence for on-going 'minor' interaction. We tentatively propose that the γ-ray emission during the plateau is driven by intra-ejecta shocks following the major merger event.

5.2 X-ray emission and accretion

In Section 4.8 we presented evidence that the end of the SSS X-ray emission phase was caught just as V392 Per emerged from its first Sun-constraint. The relationships in Henze et al. (2014) predict a SSS turn-on time $t_{\text{SSS,on}} = 13^{+6}_{-4}$ days (based on t_2), a corresponding turn-off $t_{\text{SSS,off}} = 60^{+80}_{-40}$ days, and a SSS black-body parameterised temperature of $k_{\text{B}}T \sim 90 \, \text{eV}$. A caveat here is that the Henze et al. (2014) relationships are defined for the M 31 nova population, where deep X-ray observations are prohibitive due to distance, and as such they may systematically over- and under-predict $t_{\text{SSS,on}}$ and $t_{\text{SSS,off}}$, respectively, for Galactic novae. Nonetheless, these predictions are
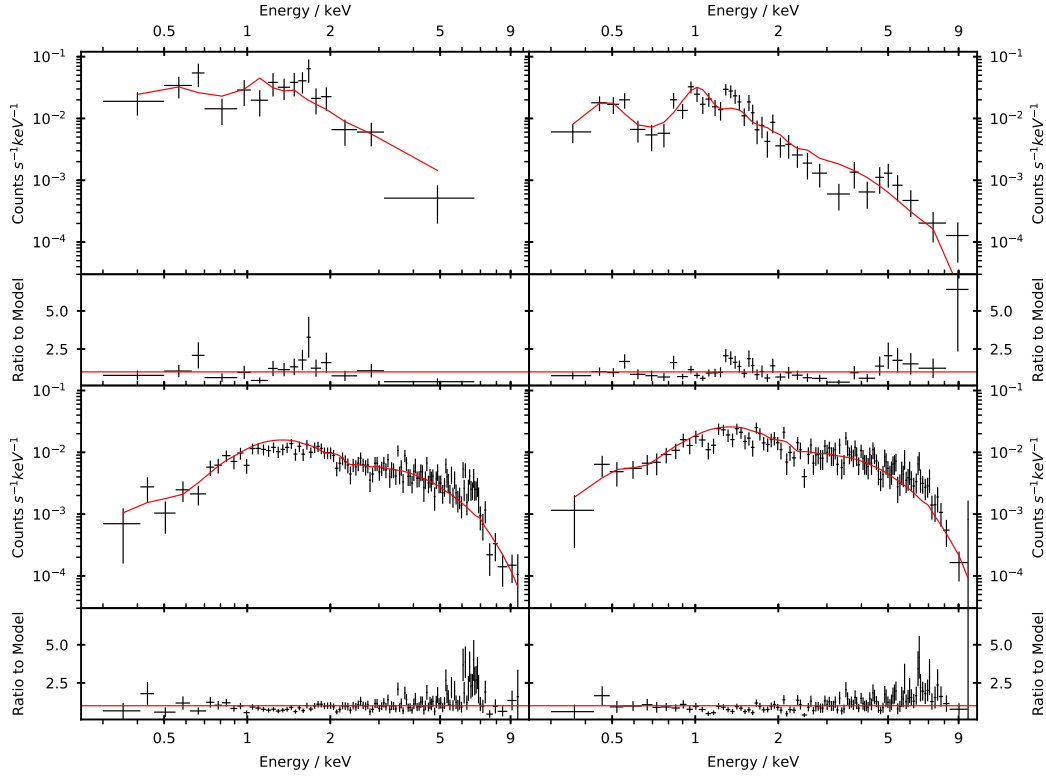
Figure 16. *Swift*/XRT spectra of V392 Per (black) and best-fit models (red), residuals included underneath. **Top left:** single observation, 83 days post-eruption. **Top right:** combination of observations 89–97 days post-eruption. **Bottom left:** days 112–361 days post-eruption. **Bottom right:** days 449–849 post-eruption.

Table 2. Fits to *Swift*/XRT spectra with $N_H = 4.8 \times 10^{21}$ cm^{-2}. The third column shows the required model components. Subsequent columns record the temperature and normalisation of the required components, black-body, first APEC, and second APEC, respectively. The final column reports the goodness of fit, the (modified) Cash statistic per degree of freedom (C stat / d.o.f.).

Time / days	Exp. time / ks	Components	kT_{BB} / eV	Norm$_{BB}$ / 10^{-3}	kT_{APEC1} / keV	Norm$_{APEC1}$ / 10^{-3}	kT_{APEC2} / keV	Norm$_{APEC2}$ / 10^{-3}	C stat / d.o.f.
83	1.6	bb+apec	62^{+17}_{-14}	$0.8^{+3.0}_{-0.6}$	$2.3^{+1.2}_{-0.5}$	$2.0^{+0.4}_{-0.4}$	...	...	87 / 74
89–97	12.0	bb+apec+apec	48^{+10}_{-8}	2^{+5}_{-1}	$1.2^{+0.2}_{-0.1}$	$0.5^{+0.2}_{-0.1}$	> 4.2	$0.5^{+0.2}_{-0.1}$	208 / 192
112–361	43.6	apec+apec	...	...	< 0.06	< 2000	> 58.3	$1.93^{+0.08}_{-0.08}$	667 / 587
449–849	19.8	apec+apec	...	...	$0.08^{+0.08}_{-0.05}$	14^{+757}_{-14}	> 57.2	$3.0^{+0.1}_{-0.1}$	548 / 537

compatible with the available X-ray observations of V392 Per. We again note that there was no associated optical spectral evidence of a SSS before the first Sun-constraint.

As is demonstrated in Figure 16, at all observed times, there is a substantial contribution to the X-ray luminosity by a harder component, that is well described by a single, or pair of, hot collisional plasma (APEC) models. Such emission is often associated with shocks. However, the consistency and longevity of the hard emission – from at least day 83 to beyond day 800 – reveals that this emission cannot be associated with an expanding ejecta. We do note that, unfortunately, there is no pre-eruption X-ray or UV data available for comparison.

During the post-nova phase, we see clear, strong, and very narrow emission from H I, He I, and especially He II, on top of a blue continuum – indicative of an accretion disk. However, the < 100 km s^{-1} width of these lines might imply a disk very close to face-on and would seemingly contradict the orbital modulation observed (see Section 3.6), which suggests an inclination closer to edge-on. At the same time, the SED of V392 Per (see Figure 3)

shows strong and consistent emission in the near-UV. As shown in Figure 8, the near-UV and X-ray emission appear correlated. We conclude from this that the UV and X-rays arise from the same system component and, given the shape of the SED, this will be from a reformed accretion disk. Most quiescent CNe do not show substantial X-ray emission, suggesting that V392 Per is a magnetic CV.

However, the potential orbital period ($P \simeq 3.2$ d; Section 3.6) is too long to be consistent with a tidally-locked polar configuration (Mukai 2017). Therefore, with APEC temperatures, perhaps, in excess of 50 keV, the X-ray emission is similar to that expected to emanate from the standing/standoff shocks observed in the accretion environment surrounding intermediate polars (IP); CVs with WD magnetic fields in the range $10^6 \lesssim B \lesssim 10^7$ G. A field of this strength would truncate the inner part of the accretion disk, causing the accreted material to flow along the magnetic field lines in accretion curtains onto the WD. Could the presence of an accretion curtain be behind the higher than expected column seen in the X-ray fits (see Section 4.8)? We note that neither our i'-band high cadence
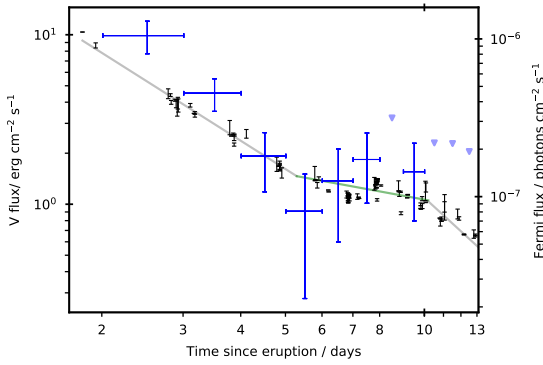
Figure 17. *V*-band light curve (in black), overlaid with Fermi-LAT γ-ray light curve (in blue).

data, or *Swift* data, are suitable for searching for a signal from the WD spin period – a key diagnostic of an IP.

We have linked the narrow emission line spectrum in the post-nova phase to active accretion in the system. As such, we restate that this disk spectrum was already visible once the system had exited the first Sun-constraint (e.g. Figure 13), while the nova ejecta was still fading, and while the SSS was still on. As such, the disk must have (at least) partially survived the eruption, or reformed during the SSS phase. From this we infer that there could have been active accretion during the SSS-phase, potentially 're-fuelling' the WD and prolonging the SSS phase (cf. Aydi et al. 2018; Henze et al. 2018).

5.3   Pre-nova versus post-nova

In Figure 2, we directly compared the 'steady state' post-nova luminosity with the pre-nova AAVSO light curve. The pre-nova state shows a quiescent baseline at $V \sim 17$ mag (low-state), punctuated with several 2–3 mag amplitude DN outbursts (high-state). The timescale of these DN outbursts are more akin to those seen in longer orbital period systems, such as GK Per. As also discussed by Munari et al. (2020a), V392 Per has not returned to its pre-nova quiescent level. The system has remained at an elevated high-state of $V \sim 15$ mag for (at least) two years post-eruption. During this time, the near-UV and X-ray luminosity continue to creep upwards (Figure 8) – i.e., there is no evidence so far that the system will return to the low-state. In DN systems, the majority of accretion onto the WD surface occurs when the disk is in a high state, i.e., during a DN outburst. Here, we infer that V392 Per is maintaining an elevated level of accretion post-nova, and that it is currently best classified as a nova-like variable, rather than a DN. It is unclear as to why V392 Per is remaining in this post-nova high-state. It may simply be that irradiation of the donor by the recent nova eruption is driving elevated mass loss from the companion (cf. T Pyx; Ginzburg & Quataert 2021). We are not currently in a position to predict when, or even if, the system will revert to its pre-nova state.

5.4   The underlying system

With a t_2 as short as 2 days and a SSS turn-off of ~ 100 days, the indications are that the WD in this system is particularly massive (see, e.g., Schwarz et al. 2011). Indeed, the V392 Per nova eruption is one of the fastest evolving on record, and the SSS phase may have been unusually extended through refuelling by a surviving or rapidly
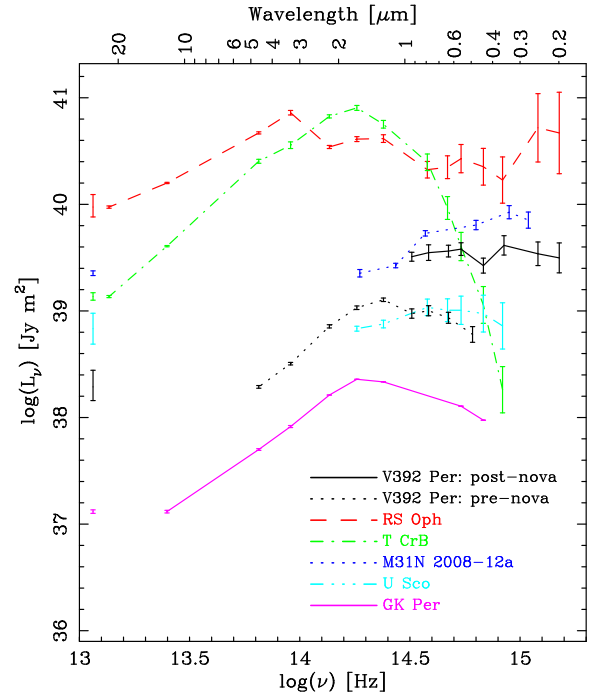
Figure 18. Distance and extinction corrected quiescent SEDs of V392 Per, RS Oph, T CrB, M31N 2008-12a, U Sco, and GK Per. Error bars include photometric and extinction uncertainties; distance uncertainties indicated to the left of the plot, lines are to aid the reader. Data from this work, Darnley et al. (2012, 2017), Evans et al. (2014), Gaia Collaboration et al. (2021), Munari et al. (2020a), Skrutskie et al. (2006), and Page et al. (2022).

reformed disk. Novae with similar parameters are expected to host WDs with masses in excess of $1.1\,M_\odot$, perhaps up to $1.3\,M_\odot$ (see Yaron et al. 2005; Osborne et al. 2011; Hillman et al. 2016, and references therein). The relatively high SSS black-body temperature ($k_B T \sim 50$ eV) seen even at the very end of the SSS phase is similarly suggestive of a massive WD. With strong forbidden Ne lines present in the spectra (see Section 3.7 and Munari et al. 2020b) there is a distinct possibility that V392 Per hosts a massive ONe WD.

In Figure 18 we present an updated V392 Per SED (cf. Darnley & Starrfield 2018). The dotted lower-luminosity black line shows the pre-nova SED, ranging from the Wise B2 band up to the *g*-band (data from Darnley & Starrfield 2018; Munari et al. 2020a, and references therein). As extensively discussed by Munari et al. (2020a), these pre-nova data suggest a warm and cool component. Munari et al. utilised these data to constrain the donor, arriving at a similar (albeit more detailed) conclusion to Darnley & Starrfield that the donor is likely a sub giant or low luminosity giant (specifically: G9 IV-III; $5.34\,R_\odot$; $1.35\,M_\odot$; $15\,L_\odot$; $T_{\rm eff} = 4875$ K; Munari et al. 2020a). With the addition of the Wise mid-IR data, we find that the pre-nova data are reasonably well represented by a single black-body, with $T_{\rm eff} = 5700 \pm 400$ (cf. $\simeq 5000$ K for GK Per; Álvarez-Hernández et al. 2021), $R = 7.8 \pm 0.6\,R_\odot$, and $L = 55^{+20}_{-18}\,L_\odot$.

The pre-nova SED is remarkably similar to that of GK Per (magenta data), albeit ~ 10 times as luminous. It is easy to draw comparisons between the two systems: both novae have evolved companions and long orbital periods; DN outbursts characterised by their month-long longevity; and like GK Per, V392 Per may be an IP. However, their post-nova behaviour is very different:

The post-nova SED is indicated by the solid black line in Figure 18, here the data span the *z'*-band to the *Swift*/UVOT uvw2

near-UV filter. It is clear that the post-nova emission is substantially greater than that seen pre-eruption (in the low states, at least). Here, the post-nova SED is reminiscent of, and indeed of similar luminosity to, the disk in M31N 2008-12a (Darnley et al. 2017). This implies that $\dot{M}$ during the post-nova phase may be very high, which may act to lessen the time toward the next eruption.

6 SUMMARY AND CONCLUSIONS

V392 Per is a known CV, which exhibited month-long GK Per-like DN outbursts, and its only known classical nova eruption was discovered on 2018 April 29. Panchromatic photometric and spectroscopic follow-up took place, with optical observations intensifying after the reported detection of γ-rays by Fermi-LAT, although the system was already in *Swift* Sun constraint at eruption. Post-Sun constraint, the eruption had entered the nebular spectral phase and *Swift* observations began. Since ~ 250 days post-eruption, V392 Per has remained in a high-state, consistently ~ 2 mag brighter than the pre-eruption quiescent minimum. Here we summarise our key findings:

(i) *Gaia* EDR3 astrometry indicates $d = 3.5^{+0.6}_{-0.5}$ kpc, and we derive $E(B - V) = 0.70^{+0.03}_{-0.02}$.

(ii) With $t_2 = 2.0 \pm 0.2$ days, the eruption is classed as 'very fast', indicative of a high mass WD.

(iii) The early spectra indicate that V392 Per is a rare Fe ɪɪ-broad class, with ejection velocities up to 5000 km s^{-1}.

(iv) Evolution of early-time H ɪ P Cygni profiles strongly suggest there were two distinct mass ejections, with the higher velocity second ejecta running into and shocking the first.

(v) These inter-ejecta, and subsequent intra-ejecta, shocks drove the γ-ray emission.

(vi) Distinct similarities between the γ-ray and early-optical evolution suggest that the early luminosity was powered by the shock emission.

(vii) The X-ray observations indicate the SSS was turning off as V392 Per emerged from Sun constraint on day 83.

(viii) Inferred SSS parameters along with forbidden Ne lines also suggest a high mass, perhaps ONe, WD.

(ix) Optical spectra show two distinct contributions: a broad initially triple, then double peaked fading ejecta spectrum; and a narrow lined and persistent accretion disk spectrum.

(x) Persistent hard X-ray emission, and post-nova near-UV luminosity, is consistent with continuing accretion, suggesting that V392 Per is an intermediate polar.

(xi) Post-nova high cadence i'-band data indicate an orbital period of $P = 3.230 \pm 0.003$ days.

(xii) The pre-nova mid-IR–optical SED suggests a sub-giant or low luminosity giant donor.

(xiii) The post-nova optical–NUV SED is substantially more luminous and is akin to an accretion disk.

In a follow-up work, we will use the extensive spectra published here to explore the underlying geometry and ionisation structure of the V392 Per ejecta. We leave V392 Per in a post-nova elevated high-state, with no indication that the system will return to its pre-nova low-state and DN behaviour. Our observations continue. . .

DATA AVAILABILITY

This work was funded by UKRI grants ST/S505559/1 and ST/V00087X/1. The Liverpool Telescope was funded by UKRI grants ST/S006176/1 and ST/T00147X/1. For the purpose of open access, the author has applied a Creative Commons Attribution (CC BY) licence to any Author Accepted Manuscript version arising. All data supporting this study are available from the respective telescope archives, in the supplementary information, or on reasonable request from the author.

REFERENCES

Abdo A. A., et al., 2010, Science, 329, 817
Ackermann M., et al., 2014, Science, 345, 554
Albert A., et al., 2022, arXiv e-prints, p. arXiv:2201.10644
Álvarez-Hernández A., et al., 2021, MNRAS, 507, 5805
Aydi E., et al., 2018, MNRAS, 474, 2679
Aydi E., et al., 2020a, Nature Astronomy, 4, 776
Aydi E., et al., 2020b, ApJ, 905, 62
Bailer-Jones C. A. L., Rybizki J., Fouesneau M., Demleitner M., Andrae R., 2021, AJ, 161, 147
Banerjee D. P. K., Joshi V., Venkataraman V., Ashok N. M., Marion G. H., Hsiao E. Y., Raj A., 2014, ApJ, 785, L11
Barnsley R. M., Smith R. J., Steele I. A., 2012, Astronomische Nachrichten, 333, 101

Bianchini A., Sabbadin F., Favero G. C., Dalmeri I., 1986, A&A, 160, 367
Blanton M. R., Roweis S., 2007, AJ, 133, 734
Bode M. F., Kahn F. D., 1985, MNRAS, 217, 205
Brown T. M., et al., 2013, PASP, 125, 1031
Burrows D. N., et al., 2005, Space Sci. Rev., 120, 165
Buson S., Jean P., Cheung C. C., 2019, ATel, 13114, 1
Chambers K. C., Pan-STARRS Team 2016, in American Astronomical Society Meeting Abstracts #227. p. 324.07
Cheung C. C., Jean P., Shore S. N., 2014, ATel, 5879, 1
Cheung C. C., Ciprini S., Johnson T. J., 2021, ATel, 14834, 1
Chochol D., Hric L., Urban Z., Komzik R., Grygar J., Papousek J., 1993, A&A, 277, 103
Chochol D., Grygar J., Pribulla T., Komzik R., Hric L., Elkin V., 1997, A&A, 318, 908
Chomiuk L., Metzger B. D., Shen K. J., 2021a, ARA&A, 59
Chomiuk L., et al., 2021b, ApJS, 257, 49
Darnley M. J., 2018a, ATel, 11846, 1
Darnley M. J., 2018b, ATel, 11872, 1
Darnley M. J., Starrfield S., 2018, RNAAS, 2, 24
Darnley M. J., Ribeiro V. A. R. M., Bode M. F., Hounsell R. A., Williams R. P., 2012, ApJ, 746, 61
Darnley M. J., et al., 2016, ApJ, 833, 149
Darnley M. J., et al., 2017, ApJ, 849, 96
Darnley M. J., Copperwheat C. M., Harvey E. J., Healy M. W., 2018a, ATel, 11601, 1
Darnley M. J., Page K. L., Beardmore A. P., Henze M., Starrfield S., 2018b, ATel, 11905, 1
Della Valle M., Izzo L., 2020, A&ARv, 28, 3
Downes R. A., Shara M. M., 1993, PASP, 105, 127
Evans P. A., et al., 2009, MNRAS, 397, 1177
Evans A., Gehrz R. D., Woodward C. E., Helton L. A., 2014, MNRAS, 444, 1683
Franckowiak A., Jean P., Wood M., Cheung C. C., Buson S., 2018, A&A, 609, A120
Gaia Collaboration et al., 2016, A&A, 595, A1
Gaia Collaboration et al., 2021, A&A, 649, A1
Gehrels N., et al., 2004, ApJ, 611, 1005
Ginzburg S., Quataert E., 2021, MNRAS, 507, 475
Gordon A. C., Aydi E., Page K. L., Li K.-L., Chomiuk L., Sokolovsky K. V., Mukai K., Seitz J., 2021, ApJ, 910, 134
Green G. M., Schlafly E., Zucker C., Speagle J. S., Finkbeiner D., 2019, ApJ, 887, 93
Güver T., Özel F., 2009, MNRAS, 400, 2050
Hachisu I., Kato M., 2006, ApJS, 167, 59
Henze M., et al., 2014, A&A, 563, A2
Henze M., et al., 2018, ApJ, 857, 68
Hill J. M., et al., 2008, in Stepp L. M., Gilmozzi R., eds, Society of Photo-Optical Instrumentation Engineers (SPIE) Conference Series Vol. 7012, Ground-based and Airborne Telescopes II. p. 701203, doi:10.1117/12.790065
Hillman Y., Prialnik D., Kovetz A., Shara M. M., 2016, ApJ, 819, 168
Honeycutt R. K., Robertson J. W., Kafka S., 2011, AJ, 141, 121
Kafka S., 2021, Observations from the AAVSO International Database, https://www.aavso.org
Kasliwal M. M., Cenko S. B., Kulkarni S. R., Ofek E. O., Quimby R., Rau A., 2011, ApJ, 735, 94
Kato T., Kojiguchi N., 2021, arXiv e-prints, p. arXiv:2107.07055
Li K.-L., Chomiuk L., Strader J., 2018, ATel, 11590, 1
Martin P., Dubus G., Jean P., Tatischeff V., Dosne C., 2018, A&A, 612, A38
Martini P., et al., 2011, PASP, 123, 187
Miszalski B., et al., 2016, MNRAS, 456, 633
Mróz P., et al., 2016, Nature, 537, 649
Mugrauer M., Gilbert H., Hoffmann S., 2018, ATel, 11617, 1
Mukai K., 2017, PASP, 129, 062001
Munari U., Ochner P., 2018, ATel, 11926, 1
Munari U., Moretti S., Maitan A., 2020a, A&A, 639, L10
Munari U., Moretti S., Maitan A., 2020b, ATel, 13381, 1
Oke J. B., 1990, AJ, 99, 1621

Osaki Y., 1996, PASP, 108, 39
Osborne J. P., et al., 2011, ApJ, 727, 124
Page K. L., et al., 2022, arXiv e-prints, p. arXiv:2205.03232
Payne-Gaposchkin C., 1964, The galactic novae. Dover Publication, New York
Piascik A. S., Steele I. A., Bates S. D., Mottram C. J., Smith R. J., Barnsley R. M., Bolton B., 2014, in Ramsay S. K., McLean I. S., Takami H., eds, Society of Photo-Optical Instrumentation Engineers (SPIE) Conference Series Vol. 9147, Ground-based and Airborne Instrumentation for Astronomy V. p. 91478H, doi:10.1117/12.2055117
Pogge R. W., et al., 2010, in McLean I. S., Ramsay S. K., Takami H., eds, Society of Photo-Optical Instrumentation Engineers (SPIE) Conference Series Vol. 7735, Ground-based and Airborne Instrumentation for Astronomy III. p. 77350A, doi:10.1117/12.857215
Rafanelli P., Rosino L., Radovich M., 1995, A&A, 294, 488
Roming P. W. A., et al., 2005, Space Sci. Rev., 120, 95
Rosino L., Iijima T., 1987, in Bode M. F., ed., RS Ophiuchi (1985) and the Recurrent Nova Phenomenon. VNU Science Press, Utrecht, p. 27
Rosino L., Iijima T., Benetti S., D'Ambrosio V., di Paolantonio A., Kolotilov E. A., 1992, A&A, 257, 603
Saizar P., Pachoulakis I., Shore S. N., Starrfield S., Williams R. E., Rothschild E., Sonneborn G., 1996, MNRAS, 279, 280
Schaefer B. E., 2021, Research Notes of the American Astronomical Society, 5, 150
Schmidt R. E., 2020, Journal of the American Association of Variable Star Observers, 48, 53
Schwarz G. J., et al., 2011, ApJS, 197, 31
Science Software Branch at STScI 2012, PyRAF: Python alternative for IRAF (ascl:1207.011)
Shara M. M., et al., 2007, Nature, 446, 159
Shara M. M., Mizusawa T., Wehinger P., Zurek D., Martin C. D., Neill J. D., Forster K., Seibert M., 2012, ApJ, 758, 121
Shara M. M., et al., 2016, ApJS, 227, 1
Shara M. M., et al., 2017, Nature, 548, 558
Skrutskie M. F., et al., 2006, AJ, 131, 1163
Smak J., 1983, ApJ, 272, 234
Smith R., Steele I., 2017, Liverpool Telescope Technical Note 1: Telescope and IO:O Throughput, doi:10.6084/m9.figshare.4659421.v1, http://researchonline.ljmu.ac.uk/id/eprint/5699/
Starrfield S., 1989, in Classical Novae. pp 39–60
Starrfield S., Sparks W. M., Truran J. W., 1976, in Eggleton P., Mitton S., Whelan J., eds, IAU Symposium Vol. 73, Structure and Evolution of Close Binary Systems. p. 155
Starrfield S., Iliadis C., Hix W. R., 2016, PASP, 128, 051001
Steele I. A., et al., 2004, in Oschmann Jacobus M. J., ed., Society of Photo-Optical Instrumentation Engineers (SPIE) Conference Series Vol. 5489, Ground-based Telescopes. pp 679–692, doi:10.1117/12.551456
Stone R. P. S., 1977, ApJ, 218, 767
Stoyanov K. A., Tomov T., Stateva I., Georgiev S., 2020, Bulgarian Astronomical Journal, 32, 63
Strope R. J., Schaefer B. E., Henden A. A., 2010, AJ, 140, 34
Teyssier F., 2019, Contributions of the Astronomical Observatory Skalnate Pleso, 49, 217
Tody D., 1986, in Crawford D. L., ed., Society of Photo-Optical Instrumentation Engineers (SPIE) Conference Series Vol. 627, Instrumentation in astronomy VI. p. 733, doi:10.1117/12.968154
Tomov T., Stateva I., Georgiev S., Konstantinova-Antova R., Stoyanov K., 2018, ATel, 11605, 1
Tonry J. L., et al., 2012, The Astrophysical Journal, 750, 99
Vanlandingham K. M., Starrfield S., Wagner R. M., Shore S. N., Sonneborn G., 1996, MNRAS, 282, 563
Wagner R. M., Terndrup D., Darnley M. J., Starrfield S., Woodward C. E., Henze M., 2018, ATel, 11588
Warner B., 1995, Cambridge Astrophysics Series, 28
Yaron O., Prialnik D., Shara M. M., Kovetz A., 2005, ApJ, 623, 398
Zemko P., Orio M., Luna G. J. M., Mukai K., Evans P. A., Bianchini A., 2017, MNRAS, 469, 476
Zwitter T., Munari U., 1994, A&AS, 107, 503

APPENDIX A: SUPPLEMENTARY ON-LINE ONLY MATERIAL

Table A1: Log of spectral observations of V392 Per. For FRODOSpec and LBT/MODS observations, the resolution of the red arm and the blue arm are both given.

Δt (d)	Date (UT)	Telescope/ instrument	Resolution ~R	Exp. time (s)
1.9	2018-04-29.898	RLE /THO-UK	527	703
2.1	2018-04-30.116	Hiltner/OSMOS	1600	7×40
2.9	2018-04-30.868	RLE /THO-UK	530	636
2.9	2018-04-30.889	RLE /THO-UK	530	636
3.8	2018-05-01.836	EBE/SSO-FR	503	1235
3.9	2018-05-01.863	DDJ/LSS-FR	525	770
4.2	2018-05-02.154	JPE/DHO-US	...	838
4.8	2018-05-02.794	BER/BVO-IT	3975	484
4.8	2018-05-02.807	BER/BVO-IT	5713	1303
4.9	2018-05-02.863	LT/FRODOSpec	2200/2600	5×60
4.9	2018-05-02.871	RLE /THO-UK	507	1820
5.2	2018-05-03.152	JPE/DHO-US	5713	763
5.9	2018-05-03.846	EBE/SSO-FR	514	1739
5.9	2018-05-03.860	LT/FRODOSpec	2200/2600	5×60
5.9	2018-05-03.886	CBO/OCT-FR	515	2111
5.9	2018-05-03.926	YBGM/OSM-FR	945	1821
6.1	2018-05-04.123	Hiltner/OSMOS	1600	4×75
6.9	2018-05-04.854	EBE/SSO-FR	521	2452
6.9	2018-05-04.859	LT/FRODOSpec	5300/5500	3×60
6.9	2018-05-04.886	CBO/OCT-FR	509	2111
7.0	2018-05-04.955	JMO/CAL-FR	646	3284
7.1	2018-05-05.123	Hiltner/OSMOS	1600	6×90
7.9	2018-05-05.830	OGA/OTO-FR	11000	2410
7.9	2018-05-05.868	DDJ/LSS-FR	522	4327
7.9	2018-05-05.855	EBE/SSO-FR	509	1817
8.1	2018-05-06.124	Hiltner/OSMOS	1600	7×90
8.1	2018-05-06.128	JPE/TEX-US	...	786
8.8	2018-05-06.838	OGA/OTO-FR	11000	3617
8.9	2018-05-06.874	CBO/OCT-FR	505	3016
8.9	2018-05-06.886	RLE /THO-UK	531	2982
9.1	2018-05-07.122	JPE/TEX-US	...	1253
9.8	2018-05-07.792	BER/BVO-IT	5915	1506
9.8	2018-05-07.816	BER/BVO-IT	3996	2013
9.9	2018-05-07.863	EBE/SSO-FR	506	1607
9.9	2018-05-07.875	CBO/OCT-FR	506	3016
9.9	2018-05-07.922	JMO/CAL-FR	641	3696
9.9	2018-05-07.924	RLE /THO-UK	513	1517
76	2018-07-12.213	LT/FRODOSpec	5300/5500	3×180
77	2018-07-13.219	LT/FRODOSpec	5300/5500	3×300
82	2018-07-18.219	LT/SPRAT	350	3×600
84	2018-07-20.221	LT/SPRAT	350	3×300
87	2018-07-23.215	LT/FRODOSpec	2200/2600	3×600
89	2018-07-25.209	LT/SPRAT	350	3×300
101	2018-08-06.185	LT/SPRAT	350	3×300
112	2018-08-17.138	LT/SPRAT	350	3×300
132	2018-09-07.474	Hiltner/OSMOS	1600	2×300
143	2018-09-17.159	LT/FRODOSpec	5300/5500	3×600
146	2018-09-21.048	LBT/MODS	2300/1850	2×300
157	2018-10-01.036	LT/SPRAT	350	3×600
186	2018-10-30.166	LT/SPRAT	350	3×600
189	2018-11-03.257	Hiltner/OSMOS	1600	2×600
212	2018-11-25.082	LT/SPRAT	350	3×600
220	2018-11-28.237	Hiltner/OSMOS	1600	2×1200

Table A1 – continued from previous page

Δt (d)	Date (UT)	Telescope/ instrument	Resolution $\sim R$	Exp. time (s)
226	2018-12-09.101	LT/FRODOSpec	5300/5500	3×900
252	2019-01-04.981	LT/FRODOSpec	5300/5500	5×1080
253	2019-01-05.984	LT/SPRAT	350	3×1200
286	2019-02-05.170	Hiltner/OSMOS	1600	3×1200
304	2019-02-23.119	Hiltner/OSMOS	1600	3×1200
307	2019-02-28.852	LT/SPRAT	350	2×900
346	2019-04-08.890	LT/SPRAT	350	3×600
351	2019-04-10.121	Hiltner/OSMOS	1600	3×1200
448	2019-07-19.204	LT/SPRAT	350	3×600
478	2019-08-18.220	LT/SPRAT	350	3×600
502	2019-09-12.442	Hiltner/OSMOS	1600	3×1200
504	2019-09-13.087	LT/SPRAT	350	3×600
527	2019-10-07.435	Hiltner/OSMOS	1600	3×1200
535	2019-10-14.003	LT/SPRAT	350	3×600
543	2019-10-23.243	LBT/MODS	2300/1850	6×600
553	2019-11-02.342	Hiltner/OSMOS	1600	3×1200
568	2019-11-16.097	LT/SPRAT	350	3×600
591	2019-12-09.940	LT/SPRAT	350	3×900
619	2020-01-07.100	Hiltner/OSMOS	1600	3×1200
854	2021-02-01.206	LT/SPRAT	350	3×1200

ARAS Observers: BER: Paolo Berardi — CBO: Christophe Boussin — DDJ: Daniel Dejean — EBE: Etienne Bertrand — JMO: Jacques Montier — JPE: Jim Edlin — OGA: Olivier Garde — RLE: Robin Leadbeater — YBGM: Yolande Buchet & Gérard Martineau.

Table A2: The Pan-STARRS reference stars used to calibrate the photometry of V392 Per. The *Swift*/UVOT *U* magnitude of #15 is included. Errors on magnitudes for *BVr′i′z′* are ±0.034, ±0.012, ±0.004, ±0.005 and ±0.010, respectively.

Reference Star no	Pan-STARRS Object ID	*U* / mag	*B* / mag	*V* / mag	*r′* / mag	*i′* / mag	*z′* / mag
1	164840708125355000	. . .	18.95	17.72	17.29	16.82	16.51
2	164800708138869000	. . .	20.16	18.96	18.54	18.08	17.70
3	164810708164722000	. . .	20.02	18.60	18.08	17.47	17.03
4	164830708184131000	. . .	19.38	18.07	17.60	17.03	16.64
5	164820708189789000	. . .	21.72	20.22	19.68	19.02	18.56
6	164830708206900000	. . .	22.53	21.01	20.46	19.77	19.23
7	164830708274029000	. . .	19.59	17.98	17.38	16.71	16.24
8	164810708286245000	. . .	19.29	18.00	17.54	17.01	16.63
9	164840708297440000	. . .	21.28	19.90	19.41	18.76	18.33
10	164830708300909000	. . .	21.00	19.27	18.64	17.92	17.41
11	164830708331564000	. . .	21.58	20.00	19.42	18.75	18.28
12	164810708363800000	. . .	20.31	18.83	18.29	17.66	17.21
13	164850708381906000	. . .	19.90	18.17	17.53	16.75	16.21
14	164850708384241000	. . .	18.29	17.27	16.92	16.53	16.26
15	164830708391402000	16.70	16.03	15.10	14.80	14.51	14.33
16	164850708400482000	. . .	20.41	19.06	18.58	18.01	17.59
17	164820708400455000	. . .	21.98	20.30	19.68	18.98	18.47
18	164860708402161000	. . .	21.12	19.59	19.03	18.37	17.91
19	164840708431519000	. . .	18.82	17.65	17.24	16.77	16.45
20	164860708441271000	. . .	20.39	19.19	18.77	18.23	17.85
21	164820708501862000	. . .	18.90	17.68	17.25	16.75	16.41
22	164810708517219000	. . .	18.96	17.70	17.25	16.74	16.38
23	164820708606127000	. . .	17.17	15.95	15.52	15.10	14.84
24	164850708622792000	. . .	19.11	17.68	17.16	16.53	16.14
25	164810708639843000	. . .	19.61	18.28	17.80	17.27	16.90

Table A3: u'BV$r'i'z'$ and *Swift*/UVOT photometry of V392 Per (AB magnitudes).

Date (UT)	Δ t / days	Telescope & Instrument	Filter	Exposure time /s	Photometry /mag
2018 Jul 21.192	84.202	LT IO:O	u'	3 × 30	14.751 ± 0.011
2018 Jul 22.217	85.227	LT IO:O	u'	3 × 30	14.838 ± 0.008
2018 Jul 23.194	86.204	LT IO:O	u'	3 × 30	14.900 ± 0.009
2018 Jul 24.185	87.195	LT IO:O	u'	3 × 30	14.865 ± 0.012
2018 Jul 25.182	88.192	LT IO:O	u'	3 × 30	14.973 ± 0.013
2018 Jul 26.190	89.200	LT IO:O	u'	3 × 30	14.898 ± 0.015
2018 Jul 27.182	90.192	LT IO:O	u'	3 × 30	14.832 ± 0.013
2018 Jul 28.175	91.185	LT IO:O	u'	3 × 30	15.122 ± 0.012
2018 Jul 29.174	92.184	LT IO:O	u'	3 × 30	15.013 ± 0.026
2018 Jul 31.169	94.179	LT IO:O	u'	3 × 30	15.096 ± 0.016
2018 Aug 01.184	95.194	LT IO:O	u'	3 × 30	14.980 ± 0.016
2018 Aug 02.159	96.169	LT IO:O	u'	3 × 30	15.034 ± 0.012
2018 Aug 03.157	97.167	LT IO:O	u'	3 × 30	15.144 ± 0.015
2018 Aug 06.148	100.158	LT IO:O	u'	3 × 30	15.170 ± 0.015
2018 Aug 08.164	102.174	LT IO:O	u'	3 × 30	15.237 ± 0.012
2018 Aug 10.171	104.181	LT IO:O	u'	3 × 30	15.345 ± 0.010
2018 Aug 16.122	110.132	LT IO:O	u'	3 × 30	15.426 ± 0.013
2018 Aug 19.165	113.175	LT IO:O	u'	3 × 30	15.430 ± 0.010
2018 Aug 22.217	116.227	LT IO:O	u'	3 × 30	15.326 ± 0.008
2018 Aug 25.097	119.107	LT IO:O	u'	3 × 30	15.587 ± 0.016
2018 Aug 28.107	122.117	LT IO:O	u'	3 × 30	15.448 ± 0.015
2018 Aug 31.085	125.095	LT IO:O	u'	3 × 30	15.391 ± 0.018
2018 Sep 03.073	128.083	LT IO:O	u'	3 × 30	15.525 ± 0.015
2018 Sep 06.066	131.076	LT IO:O	u'	3 × 30	15.483 ± 0.015
2018 Sep 09.054	134.064	LT IO:O	u'	3 × 30	15.714 ± 0.018
2018 Sep 12.062	137.072	LT IO:O	u'	3 × 30	15.811 ± 0.016
2018 Sep 18.086	143.096	LT IO:O	u'	3 × 30	15.763 ± 0.013
2018 Sep 23.018	148.028	LT IO:O	u'	3 × 30	16.090 ± 0.052
2018 Sep 26.014	151.024	LT IO:O	u'	3 × 30	16.003 ± 0.027
2018 Sep 29.057	154.067	LT IO:O	u'	3 × 30	15.849 ± 0.014
2018 Oct 02.012	157.022	LT IO:O	u'	3 × 30	16.010 ± 0.016
2018 Nov 01.111	187.121	LT IO:O	u'	3 × 30	16.329 ± 0.014
2018 Nov 08.159	194.169	LT IO:O	u'	3 × 30	16.307 ± 0.014
2018 Nov 16.117	202.127	LT IO:O	u'	3 × 30	16.341 ± 0.014
2018 Nov 26.024	212.034	LT IO:O	u'	3 × 30	16.210 ± 0.019
2018 Dec 10.064	226.074	LT IO:O	u'	3 × 30	16.228 ± 0.014
2018 Dec 15.963	231.973	LT IO:O	u'	3 × 30	16.333 ± 0.019
2018 Dec 22.839	238.849	LT IO:O	u'	3 × 30	16.413 ± 0.034
2018 Dec 28.894	244.904	LT IO:O	u'	3 × 30	16.585 ± 0.041
2019 Jan 04.919	251.929	LT IO:O	u'	3 × 30	16.450 ± 0.017
2019 Jan 10.973	257.983	LT IO:O	u'	3 × 30	16.419 ± 0.015
2019 Jan 19.987	266.997	LT IO:O	u'	3 × 30	16.341 ± 0.019
2019 Jan 25.903	272.912	LT IO:O	u'	3 × 30	16.256 ± 0.015
2019 Jan 31.939	278.949	LT IO:O	u'	3 × 30	16.145 ± 0.013
2019 Feb 06.888	284.898	LT IO:O	u'	3 × 30	16.342 ± 0.018
2019 Feb 12.874	290.884	LT IO:O	u'	3 × 30	16.465 ± 0.016
2019 Feb 28.888	306.898	LT IO:O	u'	3 × 30	16.565 ± 0.018
2019 Mar 16.846	322.856	LT IO:O	u'	3 × 30	16.335 ± 0.016
2019 Apr 08.859	345.869	LT IO:O	u'	3 × 30	16.480 ± 0.018
2019 Apr 25.851	362.861	LT IO:O	u'	3 × 30	16.294 ± 0.043
2019 Jul 19.215	447.225	LT IO:O	u'	3 × 30	16.334 ± 0.028
2019 Aug 01.218	460.228	LT IO:O	u'	3 × 30	16.393 ± 0.026
2019 Aug 19.125	478.135	LT IO:O	u'	3 × 30	16.499 ± 0.044
2019 Sep 14.113	504.123	LT IO:O	u'	3 × 60	16.322 ± 0.016
2019 Oct 14.977	534.987	LT IO:O	u'	3 × 60	16.372 ± 0.019
2019 Nov 16.937	567.947	LT IO:O	u'	3 × 60	15.834 ± 0.009
2019 Dec 09.905	590.915	LT IO:O	u'	3 × 60	16.357 ± 0.018

Continued on next page

Table A3 – continued from previous page

Date (UT)	Δ t / days	Telescope & Instrument	Filter	Exposure time /s	Photometry /mag
2020 Aug 31.152	856.162	LT IO:O	u'	3×120	16.624 ± 0.007
2021 Feb 02.865	1011.875	LT IO:O	u'	3×180	16.127 ± 0.005
2018 Apr 29.942	1.952	AAVSO MIW	B		7.398 ± 0.088
2018 Apr 30.807	2.817	AAVSO VMAG	B		7.972 ± 0.030
2018 Apr 30.870	2.880	AAVSO EHEA	B		8.097 ± 0.020
2018 Apr 30.889	2.899	AAVSO MIW	B		8.059 ± 0.036
2018 Apr 30.904	2.914	AAVSO BDG	B		8.099 ± 0.087
2018 Apr 30.913	2.923	AAVSO BDG	B		8.063 ± 0.079
2018 Apr 30.919	2.929	AAVSO BDG	B		8.095 ± 0.064
2018 May 01.101	3.110	AAVSO SDM	B		8.240 ± 0.048
2018 May 01.152	3.162	AAVSO SSTA	B		8.153 ± 0.001
2018 May 01.189	3.199	AAVSO STYA	B		8.157 ± 0.002
2018 May 01.190	3.200	AAVSO RBRB	B		8.171 ± 0.001
2018 May 01.867	3.877	AAVSO EHEA	B		8.609 ± 0.030
2018 May 02.106	4.115	AAVSO SDM	B		8.738 ± 0.199
2018 May 02.848	4.858	AAVSO ETOA	B		9.054 ± 0.027
2018 May 02.849	4.859	AAVSO ETOA	B		9.059 ± 0.012
2018 May 02.850	4.860	AAVSO ETOA	B		9.076 ± 0.034
2018 May 02.851	4.861	AAVSO ETOA	B		9.032 ± 0.020
2018 May 02.919	4.929	AAVSO MIW	B		9.127 ± 0.023
2018 May 03.896	5.906	AAVSO EHEA	B		9.297 ± 0.025
2018 May 04.192	6.202	AAVSO JDAD	B		9.326 ± 0.001
2018 May 04.210	6.220	AAVSO RBRB	B		9.306 ± 0.001
2018 May 04.808	6.818	AAVSO VMAG	B		9.480 ± 0.030
2018 May 04.827	6.837	AAVSO ETOA	B		9.504 ± 0.006
2018 May 04.828	6.838	AAVSO ETOA	B		9.529 ± 0.042
2018 May 04.829	6.839	AAVSO ETOA	B		9.537 ± 0.022
2018 May 04.830	6.839	AAVSO ETOA	B		9.520 ± 0.016
2018 May 04.874	6.884	AAVSO EHEA	B		9.596 ± 0.035
2018 May 05.204	7.214	AAVSO RBRB	B		9.387 ± 0.005
2018 May 05.225	7.235	AAVSO STYA	B		9.434 ± 0.003
2018 May 05.878	7.888	AAVSO OAR	B		9.229 ± 0.003
2018 May 05.878	7.888	AAVSO OAR	B		9.227 ± 0.003
2018 May 05.878	7.888	AAVSO OAR	B		9.279 ± 0.003
2018 May 05.879	7.889	AAVSO OAR	B		9.260 ± 0.003
2018 May 05.879	7.889	AAVSO OAR	B		9.225 ± 0.003
2018 May 05.884	7.894	AAVSO MIW	B		9.315 ± 0.023
2018 May 05.893	7.903	AAVSO OAR	B		9.235 ± 0.003
2018 May 05.894	7.904	AAVSO OAR	B		9.183 ± 0.002
2018 May 05.895	7.905	AAVSO OAR	B		9.244 ± 0.002
2018 May 05.895	7.905	AAVSO OAR	B		9.246 ± 0.002
2018 May 05.896	7.906	AAVSO OAR	B		9.162 ± 0.002
2018 May 05.906	7.916	AAVSO EHEA	B		9.353 ± 0.040
2018 May 06.044	8.054	AAVSO LDJ	B		9.292 ± 0.010
2018 May 06.873	8.883	AAVSO EHEA	B		9.629 ± 0.030
2018 May 06.884	8.894	AAVSO MIW	B		9.518 ± 0.045
2018 May 07.180	9.190	AAVSO STYA	B		9.428 ± 0.003
2018 May 07.208	9.217	AAVSO RBRB	B		9.419 ± 0.003
2018 May 07.208	9.218	AAVSO RRIB	B		9.413 ± 0.003
2018 May 07.803	9.813	AAVSO VMAG	B		9.626 ± 0.030
2018 May 07.887	9.897	AAVSO MIW	B		9.595 ± 0.032
2018 May 08.050	10.060	AAVSO LDJ	B		9.543 ± 0.005
2018 May 10.185	12.195	AAVSO RBRB	B		10.033 ± 0.005
2018 May 10.185	12.195	AAVSO STYA	B		10.034 ± 0.004
2018 May 12.178	14.188	AAVSO SSTA	B		10.489 ± 0.003
2018 May 12.804	14.814	AAVSO VMAG	B		10.595 ± 0.030
2018 May 12.846	14.856	AAVSO ETOA	B		10.651 ± 0.032
2018 May 12.848	14.858	AAVSO ETOA	B		10.622 ± 0.023

Table A3 – continued from previous page

Date (UT)	Δ t / days	Telescope & Instrument	Filter	Exposure time /s	Photometry /mag
2018 May 12.850	14.860	AAVSO ETOA	*B*		10.619 ± 0.003
2018 May 12.852	14.862	AAVSO ETOA	*B*		10.653 ± 0.030
2018 May 12.854	14.864	AAVSO ETOA	*B*		10.630 ± 0.026
2018 May 13.206	15.215	AAVSO RBRB	*B*		10.655 ± 0.005
2018 May 13.206	15.215	AAVSO LRCA	*B*		10.653 ± 0.004
2018 May 13.209	15.219	AAVSO STYA	*B*		10.673 ± 0.004
2018 May 14.175	16.185	AAVSO STYA	*B*		10.833 ± 0.011
2018 May 14.210	16.219	AAVSO RBRB	*B*		10.858 ± 0.033
2018 May 15.042	17.051	AAVSO LDJ	*B*		10.954 ± 0.005
2018 May 16.194	18.204	AAVSO RBRB	*B*		11.024 ± 0.034
2018 May 21.212	23.221	AAVSO RBRB	*B*		11.567 ± 0.017
2018 Jul 07.363	70.373	AAVSO MRV	*B*		14.052 ± 0.098
2018 Jul 14.359	77.369	AAVSO MRV	*B*		14.362 ± 0.130
2018 Jul 14.479	77.488	AAVSO SGEA	*B*		13.892 ± 0.121
2018 Jul 17.474	80.484	AAVSO SGEA	*B*		14.152 ± 0.118
2018 Jul 17.501	80.511	AAVSO SGEA	*B*		14.452 ± 0.126
2018 Jul 18.479	81.489	AAVSO SGEA	*B*		14.302 ± 0.031
2018 Jul 18.497	81.507	AAVSO SGEA	*B*		14.128 ± 0.082
2018 Jul 19.352	82.362	AAVSO CDJA	*B*		14.422 ± 0.023
2018 Jul 19.353	82.363	AAVSO CDJA	*B*		14.453 ± 0.023
2018 Jul 19.355	82.365	AAVSO CDJA	*B*		14.452 ± 0.024
2018 Jul 21.189	84.199	LT IO:O	*B*	3 × 30	14.675 ± 0.015
2018 Jul 21.456	84.466	AAVSO SGEA	*B*		14.331 ± 0.056
2018 Jul 22.213	85.223	LT IO:O	*B*	3 × 30	14.746 ± 0.013
2018 Jul 23.190	86.200	LT IO:O	*B*	3 × 30	14.722 ± 0.012
2018 Jul 24.181	87.191	LT IO:O	*B*	3 × 30	14.730 ± 0.016
2018 Jul 25.178	88.188	LT IO:O	*B*	3 × 30	14.927 ± 0.016
2018 Jul 26.186	89.196	LT IO:O	*B*	3 × 30	15.027 ± 0.032
2018 Jul 27.178	90.188	LT IO:O	*B*	3 × 30	14.795 ± 0.027
2018 Jul 28.171	91.181	LT IO:O	*B*	3 × 30	14.887 ± 0.024
2018 Jul 29.170	92.180	LT IO:O	*B*	3 × 30	15.060 ± 0.053
2018 Jul 31.165	94.175	LT IO:O	*B*	3 × 30	15.072 ± 0.019
2018 Aug 01.179	95.189	LT IO:O	*B*	3 × 30	14.993 ± 0.020
2018 Aug 02.155	96.165	LT IO:O	*B*	3 × 30	14.918 ± 0.015
2018 Aug 02.345	96.355	AAVSO CDJA	*B*		14.902 ± 0.021
2018 Aug 02.347	96.357	AAVSO CDJA	*B*		14.895 ± 0.020
2018 Aug 02.348	96.358	AAVSO CDJA	*B*		14.878 ± 0.019
2018 Aug 02.489	96.498	AAVSO SGEA	*B*		14.587 ± 0.054
2018 Aug 03.153	97.163	LT IO:O	*B*	3 × 30	15.131 ± 0.019
2018 Aug 03.486	97.496	AAVSO SGEA	*B*		14.818 ± 0.038
2018 Aug 04.152	98.162	AAVSO MRV	*B*		14.970 ± 0.110
2018 Aug 06.145	100.155	LT IO:O	*B*	3 × 30	15.071 ± 0.018
2018 Aug 06.419	100.429	AAVSO DKS	*B*		15.048 ± 0.047
2018 Aug 06.495	100.505	AAVSO SGEA	*B*		14.820 ± 0.023
2018 Aug 07.419	101.429	AAVSO DKS	*B*		15.175 ± 0.047
2018 Aug 08.160	102.170	LT IO:O	*B*	3 × 30	15.131 ± 0.013
2018 Aug 09.319	103.329	AAVSO BMSA	*B*		15.069 ± 0.028
2018 Aug 09.320	103.330	AAVSO BMSA	*B*		14.977 ± 0.025
2018 Aug 09.321	103.331	AAVSO BMSA	*B*		15.031 ± 0.026
2018 Aug 10.167	104.177	LT IO:O	*B*	3 × 30	15.247 ± 0.011
2018 Aug 10.483	104.493	AAVSO SGEA	*B*		14.822 ± 0.050
2018 Aug 13.169	107.179	LT IO:O	*B*	3 × 30	15.356 ± 0.066
2018 Aug 13.330	107.340	AAVSO BMSA	*B*		15.235 ± 0.033
2018 Aug 13.331	107.341	AAVSO BMSA	*B*		15.255 ± 0.033
2018 Aug 13.334	107.344	AAVSO BMSA	*B*		15.271 ± 0.032
2018 Aug 13.475	107.485	AAVSO SGEA	*B*		14.983 ± 0.031
2018 Aug 14.421	108.431	AAVSO SGEA	*B*		14.925 ± 0.034
2018 Aug 15.449	109.459	AAVSO SGEA	*B*		14.964 ± 0.027

Table A3 – continued from previous page

Date (UT)	Δ t / days	Telescope & Instrument	Filter	Exposure time /s	Photometry /mag
2018 Aug 15.511	109.521	AAVSO SGEA	*B*		14.804 ± 0.030
2018 Aug 16.118	110.128	LT IO:O	*B*	3 × 30	15.270 ± 0.013
2018 Aug 16.451	110.461	AAVSO SGEA	*B*		15.112 ± 0.027
2018 Aug 17.444	111.454	AAVSO SGEA	*B*		14.999 ± 0.025
2018 Aug 17.503	111.512	AAVSO SGEA	*B*		14.800 ± 0.017
2018 Aug 18.412	112.421	AAVSO SGEA	*B*		14.978 ± 0.027
2018 Aug 18.503	112.513	AAVSO SGEA	*B*		14.863 ± 0.018
2018 Aug 19.161	113.171	LT IO:O	*B*	3 × 30	15.268 ± 0.010
2018 Aug 19.449	113.459	AAVSO SGEA	*B*		15.009 ± 0.026
2018 Aug 19.482	113.492	AAVSO SGEA	*B*		14.886 ± 0.018
2018 Aug 20.190	114.200	AAVSO MRV	*B*		15.121 ± 0.058
2018 Aug 20.419	114.429	AAVSO SGEA	*B*		15.009 ± 0.025
2018 Aug 20.487	114.497	AAVSO SGEA	*B*		14.875 ± 0.016
2018 Aug 21.434	115.444	AAVSO SGEA	*B*		14.927 ± 0.026
2018 Aug 21.507	115.517	AAVSO SGEA	*B*		14.846 ± 0.017
2018 Aug 22.213	116.223	LT IO:O	*B*	3 × 30	15.207 ± 0.012
2018 Aug 22.443	116.453	AAVSO SGEA	*B*		14.934 ± 0.025
2018 Aug 22.522	116.532	AAVSO SGEA	*B*		14.897 ± 0.036
2018 Aug 23.474	117.484	AAVSO SGEA	*B*		15.029 ± 0.025
2018 Aug 23.510	117.520	AAVSO SGEA	*B*		14.905 ± 0.018
2018 Aug 25.094	119.104	LT IO:O	*B*	3 × 30	15.326 ± 0.019
2018 Aug 26.517	120.527	AAVSO SGEA	*B*		15.054 ± 0.034
2018 Aug 27.111	121.120	AAVSO MRV	*B*		15.176 ± 0.046
2018 Aug 27.517	121.527	AAVSO SGEA	*B*		15.010 ± 0.032
2018 Aug 28.104	122.113	LT IO:O	*B*	3 × 30	15.195 ± 0.017
2018 Aug 28.524	122.534	AAVSO SGEA	*B*		15.060 ± 0.044
2018 Aug 29.514	123.524	AAVSO SGEA	*B*		15.193 ± 0.034
2018 Aug 30.521	124.531	AAVSO SGEA	*B*		14.947 ± 0.041
2018 Aug 31.081	125.091	LT IO:O	*B*	3 × 30	15.315 ± 0.025
2018 Aug 31.517	125.527	AAVSO SGEA	*B*		14.978 ± 0.030
2018 Sep 01.528	126.538	AAVSO SGEA	*B*		15.049 ± 0.068
2018 Sep 02.518	127.528	AAVSO SGEA	*B*		15.109 ± 0.040
2018 Sep 02.520	127.530	AAVSO SGEA	*B*		15.110 ± 0.003
2018 Sep 03.069	128.079	LT IO:O	*B*	3 × 30	15.391 ± 0.015
2018 Sep 03.509	128.519	AAVSO SGEA	*B*		15.092 ± 0.033
2018 Sep 04.521	129.531	AAVSO SGEA	*B*		15.132 ± 0.032
2018 Sep 05.514	130.524	AAVSO SGEA	*B*		15.179 ± 0.033
2018 Sep 05.521	130.531	AAVSO SGEA	*B*		14.989 ± 0.022
2018 Sep 06.062	131.072	LT IO:O	*B*	3 × 30	15.269 ± 0.152
2018 Sep 06.504	131.514	AAVSO SGEA	*B*		15.155 ± 0.027
2018 Sep 06.511	131.521	AAVSO SGEA	*B*		14.971 ± 0.018
2018 Sep 07.498	132.508	AAVSO SGEA	*B*		15.196 ± 0.030
2018 Sep 08.511	133.521	AAVSO SGEA	*B*		15.262 ± 0.028
2018 Sep 08.525	133.535	AAVSO SGEA	*B*		15.227 ± 0.023
2018 Sep 09.050	134.060	LT IO:O	*B*	3 × 30	15.459 ± 0.015
2018 Sep 09.532	134.542	AAVSO SGEA	*B*		15.153 ± 0.043
2018 Sep 09.535	134.545	AAVSO SGEA	*B*		15.018 ± 0.035
2018 Sep 11.532	136.542	AAVSO SGEA	*B*		15.268 ± 0.045
2018 Sep 12.058	137.068	LT IO:O	*B*	3 × 30	15.549 ± 0.014
2018 Sep 13.208	138.217	AAVSO MDYA	*B*		15.292 ± 0.033
2018 Sep 13.209	138.219	AAVSO MDYA	*B*		15.304 ± 0.033
2018 Sep 13.210	138.220	AAVSO MDYA	*B*		15.392 ± 0.033
2018 Sep 13.528	138.538	AAVSO SGEA	*B*		15.173 ± 0.032
2018 Sep 13.530	138.540	AAVSO SGEA	*B*		15.049 ± 0.022
2018 Sep 18.082	143.092	LT IO:O	*B*	3 × 30	15.642 ± 0.011
2018 Sep 23.014	148.024	LT IO:O	*B*	3 × 30	15.667 ± 0.028
2018 Sep 26.010	151.020	LT IO:O	*B*	3 × 30	15.725 ± 0.018
2018 Sep 29.053	154.063	LT IO:O	*B*	3 × 30	15.627 ± 0.015

Continued on next page

Table A3 – continued from previous page

Date (UT)	Δ t / days	Telescope & Instrument	Filter	Exposure time /s	Photometry /mag
2018 Oct 02.008	157.018	LT IO:O	*B*	3 × 30	15.767 ± 0.012
2018 Oct 08.283	163.293	AAVSO SGEA	*B*		14.987 ± 0.064
2018 Nov 01.107	187.117	LT IO:O	*B*	3 × 30	16.135 ± 0.012
2018 Nov 01.516	187.526	AAVSO SGEA	*B*		15.599 ± 0.067
2018 Nov 03.468	189.478	AAVSO SGEA	*B*		15.388 ± 0.047
2018 Nov 05.154	191.164	AAVSO MRV	*B*		16.026 ± 0.036
2018 Nov 07.566	193.576	AAVSO SGEA	*B*		15.405 ± 0.140
2018 Nov 08.156	194.165	LT IO:O	*B*	3 × 30	16.084 ± 0.012
2018 Nov 16.113	202.123	LT IO:O	*B*	3 × 30	16.059 ± 0.011
2018 Nov 26.020	212.030	LT IO:O	*B*	3 × 30	16.008 ± 0.018
2018 Nov 26.315	212.325	AAVSO MRV	*B*		16.038 ± 0.043
2018 Dec 10.061	226.071	LT IO:O	*B*	3 × 30	16.111 ± 0.012
2018 Dec 15.960	231.970	LT IO:O	*B*	3 × 30	16.133 ± 0.016
2018 Dec 22.836	238.846	LT IO:O	*B*	3 × 30	16.163 ± 0.024
2018 Dec 28.890	244.900	LT IO:O	*B*	3 × 30	16.176 ± 0.022
2018 Dec 28.969	244.979	AAVSO MRV	*B*		16.053 ± 0.034
2019 Jan 04.916	251.926	LT IO:O	*B*	3 × 30	16.213 ± 0.012
2019 Jan 10.969	257.979	LT IO:O	*B*	3 × 30	16.167 ± 0.012
2019 Jan 11.075	258.085	AAVSO MRV	*B*		16.070 ± 0.029
2019 Jan 19.984	266.993	LT IO:O	*B*	3 × 30	16.182 ± 0.015
2019 Jan 25.899	272.909	LT IO:O	*B*	3 × 30	16.046 ± 0.013
2019 Jan 31.907	278.917	AAVSO MRV	*B*		15.811 ± 0.027
2019 Jan 31.935	278.945	LT IO:O	*B*	3 × 30	15.916 ± 0.011
2019 Feb 06.885	284.894	LT IO:O	*B*	3 × 30	16.156 ± 0.017
2019 Feb 12.870	290.880	LT IO:O	*B*	3 × 30	16.216 ± 0.013
2019 Feb 12.948	290.958	AAVSO MRV	*B*		16.124 ± 0.041
2019 Feb 19.895	297.905	LT IO:O	*B*	3 × 30	16.225 ± 0.118
2019 Feb 28.885	306.894	LT IO:O	*B*	3 × 30	16.226 ± 0.014
2019 Mar 04.966	310.976	AAVSO MRV	*B*		16.123 ± 0.024
2019 Mar 16.843	322.853	LT IO:O	*B*	3 × 30	16.247 ± 0.013
2019 Apr 08.855	345.865	LT IO:O	*B*	3 × 30	16.253 ± 0.017
2019 Apr 25.847	362.857	LT IO:O	*B*	3 × 30	16.251 ± 0.060
2019 Jul 19.211	447.221	LT IO:O	*B*	3 × 30	16.155 ± 0.018
2019 Aug 01.214	460.224	LT IO:O	*B*	3 × 30	16.224 ± 0.014
2019 Aug 19.122	478.131	LT IO:O	*B*	3 × 30	16.222 ± 0.020
2019 Sep 14.107	504.117	LT IO:O	*B*	3 × 60	16.180 ± 0.028
2019 Oct 14.971	534.981	LT IO:O	*B*	3 × 60	16.175 ± 0.015
2019 Nov 16.931	567.941	LT IO:O	*B*	3 × 60	15.815 ± 0.013
2019 Dec 09.899	590.909	LT IO:O	*B*	3 × 60	16.036 ± 0.020
2020 Aug 31.157	856.167	LT IO:O	*B*	3 × 120	16.380 ± 0.009
2021 Feb 02.851	1011.861	LT IO:O	*B*	3 × 120	15.989 ± 0.008
2018 Apr 29.806	1.816	AAVSO TRT	*V*		6.360 ± 0.002
2018 Apr 29.930	1.940	AAVSO MIW	*V*		6.557 ± 0.037
2018 Apr 30.775	2.785	AAVSO PMAK	*V*		7.268 ± 0.070
2018 Apr 30.807	2.817	AAVSO VMAG	*V*		7.290 ± 0.020
2018 Apr 30.817	2.827	AAVSO VOL	*V*		7.397 ± 0.028
2018 Apr 30.870	2.880	AAVSO EHEA	*V*		7.366 ± 0.015
2018 Apr 30.888	2.898	AAVSO MIW	*V*		7.417 ± 0.057
2018 Apr 30.904	2.914	AAVSO BDG	*V*		7.472 ± 0.115
2018 Apr 30.913	2.923	AAVSO BDG	*V*		7.406 ± 0.083
2018 Apr 30.919	2.929	AAVSO BDG	*V*		7.439 ± 0.093
2018 May 01.099	3.109	AAVSO SDM	*V*		7.440 ± 0.026
2018 May 01.158	3.168	AAVSO SSTA	*V*		7.560 ± 0.001
2018 May 01.172	3.182	AAVSO RBRB	*V*		7.571 ± 0.001
2018 May 01.172	3.182	AAVSO STYA	*V*		7.574 ± 0.040
2018 May 01.777	3.787	AAVSO PMAK	*V*		7.765 ± 0.100
2018 May 01.807	3.817	AAVSO TRT	*V*		7.894 ± 0.002
2018 May 01.844	3.854	AAVSO NRNA	*V*		7.860 ± 0.010

Continued on next page

Table A3 – continued from previous page

Date (UT)	Δ t / days	Telescope & Instrument	Filter	Exposure time /s	Photometry /mag
2018 May 01.861	3.871	AAVSO ATE	V		8.020 ± 0.023
2018 May 01.861	3.871	AAVSO WKL	V		7.920 ± 0.040
2018 May 01.867	3.877	AAVSO EHEA	V		7.881 ± 0.015
2018 May 02.104	4.114	AAVSO SDM	V		7.860 ± 0.062
2018 May 02.778	4.788	AAVSO PMAK	V		8.306 ± 0.100
2018 May 02.825	4.835	AAVSO NRNA	V		8.338 ± 0.005
2018 May 02.848	4.858	AAVSO ETOA	V		8.323 ± 0.059
2018 May 02.849	4.859	AAVSO ETOA	V		8.356 ± 0.038
2018 May 02.851	4.861	AAVSO ETOA	V		8.352 ± 0.055
2018 May 02.852	4.862	AAVSO ETOA	V		8.358 ± 0.035
2018 May 02.900	4.910	AAVSO MIW	V		8.436 ± 0.073
2018 May 03.778	5.788	AAVSO PMAK	V		8.443 ± 0.100
2018 May 03.795	5.805	AAVSO TRT	V		8.540 ± 0.002
2018 May 03.798	5.808	AAVSO TRT	V		8.551 ± 0.002
2018 May 03.850	5.860	AAVSO WKL	V		8.620 ± 0.040
2018 May 03.896	5.906	AAVSO EHEA	V		8.521 ± 0.025
2018 May 04.181	6.191	AAVSO JDAD	V		8.691 ± 0.001
2018 May 04.193	6.203	AAVSO RBRB	V		8.718 ± 0.001
2018 May 04.775	6.785	AAVSO PMAK	V		8.756 ± 0.050
2018 May 04.808	6.818	AAVSO VMAG	V		8.756 ± 0.020
2018 May 04.820	6.830	AAVSO ETOA	V		8.798 ± 0.067
2018 May 04.821	6.831	AAVSO ETOA	V		8.816 ± 0.030
2018 May 04.827	6.837	AAVSO ETOA	V		8.828 ± 0.040
2018 May 04.828	6.838	AAVSO ETOA	V		8.809 ± 0.010
2018 May 04.829	6.839	AAVSO ETOA	V		8.841 ± 0.032
2018 May 04.830	6.840	AAVSO ETOA	V		8.832 ± 0.051
2018 May 04.854	6.864	AAVSO AFSA	V		8.766 ± 0.008
2018 May 04.855	6.865	AAVSO AFSA	V		8.764 ± 0.006
2018 May 04.855	6.865	AAVSO AFSA	V		8.795 ± 0.006
2018 May 04.855	6.865	AAVSO AFSA	V		8.754 ± 0.006
2018 May 04.855	6.865	AAVSO AFSA	V		8.757 ± 0.005
2018 May 04.874	6.884	AAVSO EHEA	V		8.831 ± 0.020
2018 May 05.149	7.159	AAVSO GJED	V		8.787 ± 0.040
2018 May 05.193	7.203	AAVSO RBRB	V		8.797 ± 0.002
2018 May 05.208	7.218	AAVSO STYA	V		8.815 ± 0.002
2018 May 05.782	7.792	AAVSO PMAK	V		8.595 ± 0.090
2018 May 05.822	7.832	AAVSO NRNA	V		8.614 ± 0.004
2018 May 05.824	7.834	AAVSO VOL	V		8.653 ± 0.022
2018 May 05.873	7.883	AAVSO AFSA	V		8.598 ± 0.005
2018 May 05.873	7.883	AAVSO AFSA	V		8.658 ± 0.005
2018 May 05.873	7.883	AAVSO AFSA	V		8.529 ± 0.005
2018 May 05.880	7.890	AAVSO OAR	V		8.568 ± 0.001
2018 May 05.881	7.891	AAVSO OAR	V		8.564 ± 0.001
2018 May 05.881	7.891	AAVSO OAR	V		8.611 ± 0.001
2018 May 05.881	7.891	AAVSO OAR	V		8.575 ± 0.001
2018 May 05.882	7.892	AAVSO OAR	V		8.574 ± 0.001
2018 May 05.889	7.899	AAVSO MIW	V		8.836 ± 0.018
2018 May 05.897	7.907	AAVSO OAR	V		8.524 ± 0.001
2018 May 05.898	7.908	AAVSO OAR	V		8.559 ± 0.001
2018 May 05.898	7.908	AAVSO OAR	V		8.537 ± 0.001
2018 May 05.898	7.908	AAVSO OAR	V		8.522 ± 0.001
2018 May 05.899	7.909	AAVSO OAR	V		8.531 ± 0.001
2018 May 05.906	7.916	AAVSO EHEA	V		8.544 ± 0.010
2018 May 06.044	8.054	AAVSO LDJ	V		8.624 ± 0.010
2018 May 06.780	8.790	AAVSO PMAK	V		8.625 ± 0.070
2018 May 06.794	8.804	AAVSO TRT	V		8.715 ± 0.002
2018 May 06.816	8.826	AAVSO VOL	V		8.749 ± 0.035
2018 May 06.873	8.883	AAVSO EHEA	V		8.717 ± 0.010

Continued on next page

Table A3 – continued from previous page

Date (UT)	Δ t / days	Telescope & Instrument	Filter	Exposure time /s	Photometry /mag
2018 May 06.890	8.900	AAVSO MIW	V		9.033 ± 0.021
2018 May 07.169	9.179	AAVSO STYA	V		8.806 ± 0.001
2018 May 07.197	9.207	AAVSO RRIB	V		8.760 ± 0.004
2018 May 07.197	9.207	AAVSO RBRB	V		8.760 ± 0.004
2018 May 07.803	9.813	AAVSO VMAG	V		8.901 ± 0.020
2018 May 07.805	9.815	AAVSO TRT	V		8.963 ± 0.002
2018 May 07.819	9.829	AAVSO VOL	V		8.948 ± 0.027
2018 May 07.878	9.888	AAVSO EHEA	V		8.818 ± 0.030
2018 May 07.892	9.902	AAVSO MIW	V		8.927 ± 0.036
2018 May 08.044	10.054	AAVSO SHS	V		8.694 ± 0.133
2018 May 08.056	10.066	AAVSO LDJ	V		8.872 ± 0.005
2018 May 08.068	10.078	AAVSO FRL	V		8.651 ± 0.065
2018 May 08.789	10.799	AAVSO TRT	V		9.105 ± 0.002
2018 May 08.820	10.830	AAVSO VOL	V		9.170 ± 0.050
2018 May 08.881	10.891	AAVSO EHEA	V		9.118 ± 0.030
2018 May 08.889	10.899	AAVSO MIW	V		9.134 ± 0.018
2018 May 09.048	11.058	AAVSO SFRA	V		8.937 ± 0.074
2018 May 09.051	11.061	AAVSO SHS	V		8.930 ± 0.172
2018 May 09.795	11.805	AAVSO PMAK	V		9.042 ± 0.070
2018 May 09.879	11.889	AAVSO EHEA	V		9.110 ± 0.025
2018 May 10.177	12.187	AAVSO RBRB	V		9.342 ± 0.002
2018 May 10.178	12.188	AAVSO STYA	V		9.351 ± 0.003
2018 May 10.787	12.797	AAVSO PMAK	V		9.339 ± 0.060
2018 May 10.885	12.895	AAVSO AFSA	V		9.349 ± 0.009
2018 May 10.885	12.895	AAVSO AFSA	V		9.374 ± 0.009
2018 May 11.819	13.829	AAVSO TRT	V		9.714 ± 0.005
2018 May 12.039	14.049	AAVSO SHS	V		9.651 ± 0.055
2018 May 12.170	14.180	AAVSO SSTA	V		9.824 ± 0.003
2018 May 12.798	14.808	AAVSO TRT	V		9.898 ± 0.003
2018 May 12.804	14.814	AAVSO VMAG	V		9.872 ± 0.020
2018 May 12.847	14.857	AAVSO ETOA	V		9.848 ± 0.004
2018 May 12.849	14.859	AAVSO ETOA	V		9.895 ± 0.009
2018 May 12.851	14.861	AAVSO ETOA	V		9.889 ± 0.014
2018 May 12.853	14.863	AAVSO ETOA	V		9.886 ± 0.017
2018 May 12.854	14.864	AAVSO ETOA	V		9.916 ± 0.005
2018 May 12.859	14.869	AAVSO AFSA	V		9.797 ± 0.009
2018 May 12.860	14.870	AAVSO AFSA	V		9.876 ± 0.009
2018 May 12.860	14.870	AAVSO AFSA	V		9.818 ± 0.009
2018 May 13.193	15.203	AAVSO RBRB	V		10.025 ± 0.004
2018 May 13.194	15.204	AAVSO LRCA	V		10.030 ± 0.017
2018 May 13.197	15.207	AAVSO STYA	V		10.097 ± 0.002
2018 May 13.800	15.810	AAVSO TRT	V		10.144 ± 0.003
2018 May 13.824	15.834	AAVSO MMAO	V		10.145 ± 0.022
2018 May 14.042	16.052	AAVSO LDJ	V		10.163 ± 0.005
2018 May 14.188	16.198	AAVSO STYA	V		10.257 ± 0.012
2018 May 14.204	16.214	AAVSO RBRB	V		10.241 ± 0.004
2018 May 14.828	16.838	AAVSO MMAO	V		10.286 ± 0.024
2018 May 14.865	16.875	AAVSO AFSA	V		10.277 ± 0.011
2018 May 14.865	16.875	AAVSO AFSA	V		10.277 ± 0.011
2018 May 14.865	16.875	AAVSO AFSA	V		10.255 ± 0.011
2018 May 14.865	16.875	AAVSO AFSA	V		10.255 ± 0.011
2018 May 14.865	16.875	AAVSO AFSA	V		10.298 ± 0.011
2018 May 14.865	16.875	AAVSO AFSA	V		10.298 ± 0.011
2018 May 14.890	16.900	AAVSO EHEA	V		10.364 ± 0.035
2018 May 15.042	17.052	AAVSO SHS	V		10.153 ± 0.123
2018 May 15.043	17.053	AAVSO LDJ	V		10.396 ± 0.005
2018 May 15.838	17.848	AAVSO MMAO	V		10.492 ± 0.028
2018 May 16.220	18.230	AAVSO RBRB	V		10.562 ± 0.006

Continued on next page

Table A3 – continued from previous page

Date (UT)	Δ t / days	Telescope & Instrument	Filter	Exposure time /s	Photometry /mag
2018 May 16.826	18.836	AAVSO MMAO	V		10.666 ± 0.032
2018 May 18.830	20.840	AAVSO MMAO	V		11.030 ± 0.040
2018 May 18.838	20.848	AAVSO NRNA	V		11.081 ± 0.012
2018 May 19.046	21.056	AAVSO LDJ	V		11.142 ± 0.009
2018 May 19.088	21.098	AAVSO SHS	V		10.975 ± 0.170
2018 May 19.201	21.211	AAVSO RBRB	V		11.126 ± 0.005
2018 May 20.846	22.856	AAVSO NRNA	V		11.198 ± 0.032
2018 May 21.197	23.207	AAVSO RBRB	V		11.214 ± 0.012
2018 May 22.857	24.867	AAVSO NRNA	V		11.647 ± 0.017
2018 May 31.870	33.880	AAVSO AFSA	V		11.827 ± 0.034
2018 May 31.870	33.880	AAVSO AFSA	V		12.011 ± 0.037
2018 May 31.870	33.880	AAVSO AFSA	V		11.713 ± 0.031
2018 Jun 12.373	45.383	AAVSO MRV	V		12.377 ± 0.174
2018 Jun 14.377	47.387	AAVSO MRV	V		12.445 ± 0.213
2018 Jun 26.361	59.371	AAVSO MRV	V		12.966 ± 0.160
2018 Jun 26.370	59.380	AAVSO MRV	V		13.006 ± 0.190
2018 Jun 30.368	63.378	AAVSO MRV	V		13.204 ± 0.084
2018 Jul 07.357	70.367	AAVSO MRV	V		13.271 ± 0.052
2018 Jul 08.202	71.212	AAVSO SHS	V		13.354 ± 0.164
2018 Jul 09.360	72.370	AAVSO MRV	V		13.507 ± 0.058
2018 Jul 14.352	77.362	AAVSO MRV	V		13.593 ± 0.116
2018 Jul 14.477	77.487	AAVSO SGEA	V		13.640 ± 0.035
2018 Jul 16.497	79.507	AAVSO SGEA	V		13.819 ± 0.088
2018 Jul 17.472	80.482	AAVSO SGEA	V		13.850 ± 0.028
2018 Jul 17.500	80.510	AAVSO SGEA	V		13.765 ± 0.122
2018 Jul 18.476	81.486	AAVSO SGEA	V		13.842 ± 0.058
2018 Jul 18.495	81.505	AAVSO SGEA	V		13.922 ± 0.040
2018 Jul 19.349	82.359	AAVSO CDJA	V		13.714 ± 0.012
2018 Jul 19.350	82.360	AAVSO CDJA	V		13.751 ± 0.011
2018 Jul 19.351	82.361	AAVSO CDJA	V		13.714 ± 0.011
2018 Jul 19.353	82.363	AAVSO MRV	V		13.849 ± 0.047
2018 Jul 21.191	84.201	LT IO:O	V	3 × 30	13.830 ± 0.010
2018 Jul 21.453	84.463	AAVSO SGEA	V		13.900 ± 0.030
2018 Jul 22.215	85.225	LT IO:O	V	3 × 30	13.874 ± 0.009
2018 Jul 23.192	86.202	LT IO:O	V	3 × 30	13.880 ± 0.009
2018 Jul 24.183	87.193	LT IO:O	V	3 × 30	13.903 ± 0.009
2018 Jul 25.180	88.190	LT IO:O	V	3 × 30	13.990 ± 0.010
2018 Jul 26.188	89.198	LT IO:O	V	3 × 30	14.020 ± 0.012
2018 Jul 27.180	90.190	LT IO:O	V	3 × 30	13.923 ± 0.011
2018 Jul 28.173	91.183	LT IO:O	V	3 × 30	14.034 ± 0.012
2018 Jul 29.172	92.182	LT IO:O	V	3 × 30	14.082 ± 0.018
2018 Jul 31.167	94.177	LT IO:O	V	3 × 30	14.141 ± 0.011
2018 Aug 01.181	95.191	LT IO:O	V	3 × 30	14.092 ± 0.010
2018 Aug 02.157	96.167	LT IO:O	V	3 × 30	14.023 ± 0.009
2018 Aug 02.342	96.352	AAVSO CDJA	V		14.075 ± 0.010
2018 Aug 02.343	96.353	AAVSO CDJA	V		14.059 ± 0.010
2018 Aug 02.344	96.354	AAVSO CDJA	V		14.057 ± 0.010
2018 Aug 02.486	96.496	AAVSO SGEA	V		14.148 ± 0.029
2018 Aug 03.155	97.165	LT IO:O	V	3 × 30	14.198 ± 0.011
2018 Aug 03.196	97.206	AAVSO MUY	V		14.200 ± 0.040
2018 Aug 03.484	97.494	AAVSO SGEA	V		14.314 ± 0.035
2018 Aug 04.150	98.160	AAVSO MRV	V		14.260 ± 0.037
2018 Aug 06.128	100.138	AAVSO SHS	V		14.340 ± 0.307
2018 Aug 06.146	100.156	LT IO:O	V	3 × 30	14.178 ± 0.011
2018 Aug 06.416	100.426	AAVSO DKS	V		14.261 ± 0.014
2018 Aug 06.493	100.503	AAVSO SGEA	V		14.251 ± 0.022
2018 Aug 07.416	101.426	AAVSO DKS	V		14.349 ± 0.018
2018 Aug 08.162	102.172	LT IO:O	V	3 × 30	14.220 ± 0.009

Continued on next page

Table A3 – continued from previous page

Date (UT)	Δ t / days	Telescope & Instrument	Filter	Exposure time /s	Photometry /mag
2018 Aug 09.311	103.321	AAVSO BMSA	V		14.166 ± 0.011
2018 Aug 09.312	103.322	AAVSO BMSA	V		14.121 ± 0.010
2018 Aug 09.314	103.324	AAVSO BMSA	V		14.117 ± 0.010
2018 Aug 10.169	104.179	LT IO:O	V	3 × 30	14.287 ± 0.008
2018 Aug 10.480	104.490	AAVSO SGEA	V		14.320 ± 0.045
2018 Aug 13.171	107.181	LT IO:O	V	3 × 30	14.260 ± 0.020
2018 Aug 13.320	107.330	AAVSO MRV	V		14.512 ± 0.055
2018 Aug 13.325	107.335	AAVSO BMSA	V		14.398 ± 0.017
2018 Aug 13.326	107.336	AAVSO BMSA	V		14.403 ± 0.018
2018 Aug 13.327	107.337	AAVSO BMSA	V		14.453 ± 0.018
2018 Aug 13.472	107.482	AAVSO SGEA	V		14.425 ± 0.028
2018 Aug 14.419	108.429	AAVSO SGEA	V		14.336 ± 0.029
2018 Aug 14.519	108.529	AAVSO SGEA	V		14.509 ± 0.043
2018 Aug 15.447	109.457	AAVSO SGEA	V		14.377 ± 0.026
2018 Aug 15.510	109.520	AAVSO SGEA	V		14.349 ± 0.019
2018 Aug 16.120	110.130	LT IO:O	V	3 × 30	14.296 ± 0.011
2018 Aug 16.449	110.459	AAVSO SGEA	V		14.529 ± 0.027
2018 Aug 17.442	111.452	AAVSO SGEA	V		14.403 ± 0.025
2018 Aug 17.501	111.511	AAVSO SGEA	V		14.291 ± 0.015
2018 Aug 18.409	112.419	AAVSO SGEA	V		14.335 ± 0.026
2018 Aug 18.502	112.512	AAVSO SGEA	V		14.355 ± 0.016
2018 Aug 19.163	113.173	LT IO:O	V	3 × 30	14.327 ± 0.009
2018 Aug 19.447	113.457	AAVSO SGEA	V		14.383 ± 0.024
2018 Aug 19.481	113.491	AAVSO SGEA	V		14.346 ± 0.017
2018 Aug 20.188	114.198	AAVSO MRV	V		14.341 ± 0.037
2018 Aug 20.223	114.233	AAVSO MUY	V		14.400 ± 0.055
2018 Aug 20.417	114.427	AAVSO SGEA	V		14.333 ± 0.023
2018 Aug 20.486	114.496	AAVSO SGEA	V		14.341 ± 0.015
2018 Aug 21.430	115.440	AAVSO SGEA	V		14.331 ± 0.023
2018 Aug 21.506	115.516	AAVSO SGEA	V		14.370 ± 0.026
2018 Aug 22.215	116.225	LT IO:O	V	3 × 30	14.243 ± 0.008
2018 Aug 22.440	116.450	AAVSO SGEA	V		14.390 ± 0.025
2018 Aug 22.521	116.531	AAVSO SGEA	V		14.309 ± 0.021
2018 Aug 23.472	117.482	AAVSO SGEA	V		14.417 ± 0.024
2018 Aug 23.508	117.518	AAVSO SGEA	V		14.352 ± 0.015
2018 Aug 25.095	119.105	LT IO:O	V	3 × 30	14.389 ± 0.009
2018 Aug 26.514	120.524	AAVSO SGEA	V		14.392 ± 0.030
2018 Aug 27.109	121.119	AAVSO MRV	V		14.334 ± 0.027
2018 Aug 27.515	121.525	AAVSO SGEA	V		14.407 ± 0.028
2018 Aug 28.105	122.115	LT IO:O	V	3 × 30	14.315 ± 0.010
2018 Aug 28.522	122.532	AAVSO SGEA	V		14.369 ± 0.029
2018 Aug 29.511	123.521	AAVSO SGEA	V		14.524 ± 0.030
2018 Aug 30.519	124.529	AAVSO SGEA	V		14.415 ± 0.037
2018 Aug 31.083	125.093	LT IO:O	V	3 × 30	14.282 ± 0.011
2018 Aug 31.515	125.525	AAVSO SGEA	V		14.410 ± 0.027
2018 Aug 31.529	125.539	AAVSO SGEA	V		14.442 ± 0.029
2018 Sep 01.525	126.535	AAVSO SGEA	V		14.433 ± 0.037
2018 Sep 02.516	127.526	AAVSO SGEA	V		14.588 ± 0.034
2018 Sep 02.519	127.529	AAVSO SGEA	V		14.514 ± 0.024
2018 Sep 03.071	128.081	LT IO:O	V	3 × 30	14.426 ± 0.010
2018 Sep 03.507	128.517	AAVSO SGEA	V		14.433 ± 0.028
2018 Sep 04.519	129.529	AAVSO SGEA	V		14.575 ± 0.028
2018 Sep 05.512	130.522	AAVSO SGEA	V		14.548 ± 0.027
2018 Sep 05.519	130.529	AAVSO SGEA	V		14.446 ± 0.018
2018 Sep 06.064	131.074	LT IO:O	V	3 × 30	14.431 ± 0.011
2018 Sep 06.502	131.512	AAVSO SGEA	V		14.486 ± 0.024
2018 Sep 06.510	131.520	AAVSO SGEA	V		14.446 ± 0.016
2018 Sep 07.496	132.506	AAVSO SGEA	V		14.606 ± 0.029

Continued on next page

Table A3 – continued from previous page

Date (UT)	Δt / days	Telescope & Instrument	Filter	Exposure time /s	Photometry /mag
2018 Sep 08.509	133.519	AAVSO SGEA	V		14.628 ± 0.025
2018 Sep 08.524	133.534	AAVSO SGEA	V		14.650 ± 0.020
2018 Sep 09.052	134.062	LT IO:O	V	3 × 30	14.534 ± 0.009
2018 Sep 09.530	134.540	AAVSO SGEA	V		14.561 ± 0.031
2018 Sep 09.533	134.543	AAVSO SGEA	V		14.458 ± 0.023
2018 Sep 10.074	135.084	AAVSO SHS	V		14.578 ± 0.126
2018 Sep 10.279	135.289	AAVSO VRG	V		14.487 ± 0.013
2018 Sep 10.280	135.290	AAVSO VRG	V		14.482 ± 0.015
2018 Sep 10.283	135.293	AAVSO VRG	V		14.489 ± 0.016
2018 Sep 10.285	135.295	AAVSO VRG	V		14.512 ± 0.017
2018 Sep 10.286	135.296	AAVSO VRG	V		14.516 ± 0.016
2018 Sep 10.290	135.300	AAVSO VRG	V		14.553 ± 0.017
2018 Sep 10.294	135.304	AAVSO VRG	V		14.577 ± 0.019
2018 Sep 10.297	135.307	AAVSO VRG	V		14.500 ± 0.017
2018 Sep 10.298	135.308	AAVSO VRG	V		14.555 ± 0.018
2018 Sep 10.302	135.312	AAVSO VRG	V		14.497 ± 0.020
2018 Sep 11.529	136.539	AAVSO SGEA	V		14.555 ± 0.030
2018 Sep 12.060	137.070	LT IO:O	V	3 × 30	14.572 ± 0.010
2018 Sep 13.203	138.213	AAVSO MDYA	V		14.633 ± 0.014
2018 Sep 13.204	138.214	AAVSO MDYA	V		14.630 ± 0.014
2018 Sep 13.205	138.215	AAVSO MDYA	V		14.651 ± 0.015
2018 Sep 13.526	138.536	AAVSO SGEA	V		14.593 ± 0.027
2018 Sep 13.529	138.539	AAVSO SGEA	V		14.450 ± 0.019
2018 Sep 14.039	139.049	AAVSO SHS	V		14.496 ± 0.092
2018 Sep 14.538	139.548	AAVSO SGEA	V		14.650 ± 0.047
2018 Sep 15.265	140.275	AAVSO MRV	V		14.703 ± 0.044
2018 Sep 16.540	141.550	AAVSO SGEA	V		14.511 ± 0.038
2018 Sep 18.084	143.094	LT IO:O	V	3 × 30	14.622 ± 0.009
2018 Sep 23.016	148.026	LT IO:O	V	3 × 30	14.676 ± 0.020
2018 Sep 26.012	151.022	LT IO:O	V	3 × 30	14.739 ± 0.011
2018 Sep 29.055	154.065	LT IO:O	V	3 × 30	14.663 ± 0.009
2018 Oct 02.010	157.020	LT IO:O	V	3 × 30	14.734 ± 0.009
2018 Oct 08.282	163.292	AAVSO SGEA	V		14.627 ± 0.048
2018 Oct 28.559	183.569	AAVSO SGEA	V		15.004 ± 0.179
2018 Nov 01.109	187.119	LT IO:O	V	3 × 30	15.036 ± 0.009
2018 Nov 01.515	187.525	AAVSO SGEA	V		14.967 ± 0.054
2018 Nov 03.467	189.477	AAVSO SGEA	V		14.829 ± 0.038
2018 Nov 05.152	191.162	AAVSO MRV	V		14.942 ± 0.045
2018 Nov 07.565	193.575	AAVSO SGEA	V		14.926 ± 0.081
2018 Nov 08.042	194.052	AAVSO SHS	V		15.358 ± 0.157
2018 Nov 08.157	194.167	LT IO:O	V	3 × 30	15.071 ± 0.010
2018 Nov 16.115	202.125	LT IO:O	V	3 × 30	15.067 ± 0.008
2018 Nov 26.022	212.032	LT IO:O	V	3 × 30	15.049 ± 0.010
2018 Nov 26.316	212.326	AAVSO MRV	V		15.138 ± 0.026
2018 Dec 03.962	219.972	AAVSO ODEA	V		15.075 ± 0.116
2018 Dec 03.965	219.975	AAVSO ODEA	V		15.069 ± 0.132
2018 Dec 03.968	219.978	AAVSO ODEA	V		15.111 ± 0.136
2018 Dec 10.062	226.072	LT IO:O	V	3 × 30	15.076 ± 0.008
2018 Dec 15.961	231.971	LT IO:O	V	3 × 30	15.134 ± 0.011
2018 Dec 22.838	238.848	LT IO:O	V	3 × 30	15.148 ± 0.015
2018 Dec 28.892	244.902	LT IO:O	V	3 × 30	15.383 ± 0.023
2018 Dec 28.967	244.977	AAVSO MRV	V		15.199 ± 0.018
2019 Jan 04.918	251.928	LT IO:O	V	3 × 30	15.182 ± 0.009
2019 Jan 10.971	257.981	LT IO:O	V	3 × 30	15.170 ± 0.010
2019 Jan 11.073	258.083	AAVSO MRV	V		15.181 ± 0.018
2019 Jan 19.985	266.995	LT IO:O	V	3 × 30	15.133 ± 0.010
2019 Jan 25.901	272.911	LT IO:O	V	3 × 30	15.097 ± 0.009
2019 Jan 31.905	278.915	AAVSO MRV	V		14.981 ± 0.024

Continued on next page

Table A3 – continued from previous page

Date (UT)	Δ t / days	Telescope & Instrument	Filter	Exposure time /s	Photometry /mag
2019 Jan 31.937	278.947	LT IO:O	V	3×30	14.991 ± 0.008
2019 Feb 06.886	284.896	LT IO:O	V	3×30	15.140 ± 0.009
2019 Feb 12.872	290.882	LT IO:O	V	3×30	15.209 ± 0.009
2019 Feb 12.945	290.955	AAVSO MRV	V		15.236 ± 0.016
2019 Feb 19.897	297.907	LT IO:O	V	3×30	15.184 ± 0.040
2019 Feb 26.857	304.867	AAVSO RZD	V		15.032 ± 0.067
2019 Feb 28.886	306.896	LT IO:O	V	3×30	15.289 ± 0.008
2019 Mar 04.964	310.974	AAVSO MRV	V		15.214 ± 0.020
2019 Mar 16.844	322.854	LT IO:O	V	3×30	15.245 ± 0.009
2019 Apr 08.857	345.867	LT IO:O	V	3×30	15.240 ± 0.009
2019 Apr 25.849	362.859	LT IO:O	V	3×30	15.261 ± 0.013
2019 Jul 19.213	447.223	LT IO:O	V	3×30	15.201 ± 0.010
2019 Aug 01.216	460.226	LT IO:O	V	3×30	15.238 ± 0.009
2019 Aug 19.123	478.133	LT IO:O	V	3×30	15.236 ± 0.010
2019 Sep 14.110	504.120	LT IO:O	V	3×60	15.182 ± 0.012
2019 Oct 14.974	534.984	LT IO:O	V	3×60	15.195 ± 0.012
2019 Nov 16.934	567.944	LT IO:O	V	3×60	14.877 ± 0.009
2019 Dec 09.902	590.912	LT IO:O	V	3×60	15.188 ± 0.012
2020 Aug 31.162	856.172	LT IO:O	V	3×120	15.383 ± 0.008
2021 Feb 02.858	1011.868	LT IO:O	V	3×180	15.027 ± 0.007
2018 Apr 30.807	2.817	AAVSO VMAG	r'		6.500 ± 0.020
2018 May 01.029	3.039	AAVSO KHAB	r'		6.743 ± 0.070
2018 May 01.029	3.039	AAVSO KHAB	r'		6.682 ± 0.070
2018 May 01.029	3.039	AAVSO KHAB	r'		6.837 ± 0.070
2018 May 01.029	3.039	AAVSO KHAB	r'		6.797 ± 0.070
2018 May 01.848	3.858	AAVSO NRNA	r'		7.265 ± 0.031
2018 May 01.848	3.858	AAVSO NRNA	r'		6.949 ± 0.009
2018 May 01.877	3.887	AAVSO BRIA	r'		7.959 ± 0.117
2018 May 01.880	3.890	AAVSO BRIA	r'		7.989 ± 0.121
2018 May 01.882	3.892	AAVSO BRIA	r'		7.926 ± 0.127
2018 May 01.884	3.894	AAVSO BRIA	r'		7.959 ± 0.114
2018 May 01.887	3.897	AAVSO BRIA	r'		8.041 ± 0.073
2018 May 01.889	3.899	AAVSO BRIA	r'		7.957 ± 0.119
2018 May 01.892	3.902	AAVSO BRIA	r'		7.939 ± 0.133
2018 May 01.894	3.904	AAVSO BRIA	r'		7.919 ± 0.155
2018 May 01.896	3.906	AAVSO BRIA	r'		8.013 ± 0.089
2018 May 01.899	3.909	AAVSO BRIA	r'		8.024 ± 0.070
2018 May 01.901	3.911	AAVSO BRIA	r'		7.921 ± 0.099
2018 May 01.903	3.913	AAVSO BRIA	r'		8.034 ± 0.109
2018 May 01.905	3.915	AAVSO BRIA	r'		7.947 ± 0.057
2018 May 01.907	3.917	AAVSO BRIA	r'		7.959 ± 0.084
2018 May 01.910	3.920	AAVSO BRIA	r'		7.985 ± 0.063
2018 May 01.912	3.922	AAVSO BRIA	r'		7.875 ± 0.125
2018 May 01.916	3.926	AAVSO BRIA	r'		7.901 ± 0.154
2018 May 01.918	3.928	AAVSO BRIA	r'		7.901 ± 0.083
2018 May 02.782	4.792	AAVSO JPG	r'		7.584 ± 0.040
2018 May 02.846	4.856	AAVSO NRNA	r'		7.295 ± 0.004
2018 May 02.849	4.859	AAVSO NRNA	r'		7.564 ± 0.003
2018 May 03.849	5.859	AAVSO BRIA	r'		8.548 ± 0.078
2018 May 03.851	5.861	AAVSO BRIA	r'		8.495 ± 0.092
2018 May 03.854	5.864	AAVSO BRIA	r'		8.524 ± 0.038
2018 May 03.856	5.866	AAVSO BRIA	r'		8.485 ± 0.033
2018 May 03.858	5.868	AAVSO BRIA	r'		8.509 ± 0.058
2018 May 03.861	5.871	AAVSO BRIA	r'		8.457 ± 0.077
2018 May 03.863	5.873	AAVSO BRIA	r'		8.543 ± 0.069
2018 May 03.865	5.875	AAVSO BRIA	r'		8.463 ± 0.119
2018 May 03.868	5.878	AAVSO BRIA	r'		8.524 ± 0.043
2018 May 03.870	5.880	AAVSO BRIA	r'		8.486 ± 0.088

Continued on next page

Table A3 – continued from previous page

Date (UT)	Δ t / days	Telescope & Instrument	Filter	Exposure time /s	Photometry /mag
2018 May 03.873	5.883	AAVSO BRIA	r'		8.512 ± 0.097
2018 May 04.808	6.818	AAVSO VMAG	r'		7.756 ± 0.020
2018 May 04.820	6.830	AAVSO ETOA	r'		7.745 ± 0.002
2018 May 04.820	6.830	AAVSO ETOA	r'		7.765 ± 0.002
2018 May 04.821	6.831	AAVSO ETOA	r'		7.723 ± 0.011
2018 May 04.827	6.837	AAVSO ETOA	r'		7.767 ± 0.035
2018 May 04.828	6.838	AAVSO ETOA	r'		7.730 ± 0.027
2018 May 04.829	6.839	AAVSO ETOA	r'		7.756 ± 0.020
2018 May 04.830	6.840	AAVSO ETOA	r'		7.714 ± 0.009
2018 May 04.854	6.864	AAVSO AFSA	r'		7.995 ± 0.005
2018 May 04.854	6.864	AAVSO AFSA	r'		7.989 ± 0.005
2018 May 04.854	6.864	AAVSO AFSA	r'		7.967 ± 0.005
2018 May 04.854	6.864	AAVSO AFSA	r'		7.965 ± 0.005
2018 May 05.215	7.225	AAVSO RBRB	r'		7.777 ± 0.002
2018 May 05.824	7.834	AAVSO NRNA	r'		7.861 ± 0.002
2018 May 05.828	7.838	AAVSO NRNA	r'		8.089 ± 0.002
2018 May 05.858	7.868	AAVSO BRIA	r'		8.710 ± 0.051
2018 May 05.860	7.870	AAVSO BRIA	r'		8.747 ± 0.049
2018 May 05.863	7.873	AAVSO BRIA	r'		8.775 ± 0.073
2018 May 05.863	7.873	AAVSO DPA	r'		7.662 ± 0.029
2018 May 05.865	7.875	AAVSO BRIA	r'		8.741 ± 0.065
2018 May 05.867	7.877	AAVSO BRIA	r'		8.698 ± 0.035
2018 May 05.869	7.879	AAVSO BRIA	r'		8.766 ± 0.029
2018 May 05.871	7.881	AAVSO AFSA	r'		7.945 ± 0.005
2018 May 05.871	7.881	AAVSO AFSA	r'		7.973 ± 0.006
2018 May 05.871	7.881	AAVSO AFSA	r'		7.906 ± 0.005
2018 May 05.871	7.881	AAVSO AFSA	r'		7.944 ± 0.005
2018 May 05.871	7.881	AAVSO BRIA	r'		8.679 ± 0.084
2018 May 05.873	7.883	AAVSO BRIA	r'		8.724 ± 0.048
2018 May 05.876	7.886	AAVSO BRIA	r'		8.739 ± 0.084
2018 May 05.878	7.888	AAVSO BRIA	r'		8.754 ± 0.035
2018 May 05.880	7.890	AAVSO BRIA	r'		8.746 ± 0.043
2018 May 05.882	7.892	AAVSO BRIA	r'		8.765 ± 0.061
2018 May 05.886	7.896	AAVSO BRIA	r'		8.679 ± 0.071
2018 May 05.888	7.898	AAVSO BRIA	r'		8.723 ± 0.093
2018 May 05.890	7.900	AAVSO BRIA	r'		8.744 ± 0.073
2018 May 05.892	7.902	AAVSO BRIA	r'		8.679 ± 0.028
2018 May 06.012	8.022	AAVSO KHAB	r'		7.858 ± 0.070
2018 May 06.849	8.859	AAVSO BRIA	r'		8.887 ± 0.074
2018 May 06.851	8.861	AAVSO BRIA	r'		8.879 ± 0.155
2018 May 06.853	8.863	AAVSO BRIA	r'		8.911 ± 0.052
2018 May 06.855	8.865	AAVSO BRIA	r'		8.911 ± 0.048
2018 May 06.857	8.867	AAVSO BRIA	r'		8.865 ± 0.059
2018 May 06.859	8.869	AAVSO BRIA	r'		8.851 ± 0.073
2018 May 06.861	8.871	AAVSO BRIA	r'		8.845 ± 0.046
2018 May 06.864	8.874	AAVSO BRIA	r'		8.884 ± 0.077
2018 May 06.866	8.876	AAVSO BRIA	r'		8.887 ± 0.072
2018 May 06.868	8.878	AAVSO BRIA	r'		8.891 ± 0.031
2018 May 06.870	8.880	AAVSO BRIA	r'		8.877 ± 0.054
2018 May 06.872	8.882	AAVSO BRIA	r'		8.876 ± 0.056
2018 May 06.874	8.884	AAVSO BRIA	r'		8.841 ± 0.034
2018 May 06.876	8.886	AAVSO BRIA	r'		8.875 ± 0.062
2018 May 06.879	8.889	AAVSO BRIA	r'		8.890 ± 0.060
2018 May 06.881	8.891	AAVSO BRIA	r'		8.826 ± 0.087
2018 May 06.883	8.893	AAVSO BRIA	r'		8.884 ± 0.060
2018 May 06.886	8.896	AAVSO BRIA	r'		8.867 ± 0.042
2018 May 07.007	9.017	AAVSO KHAB	r'		8.122 ± 0.070
2018 May 07.188	9.198	AAVSO STYA	r'		7.887 ± 0.002

Table A3 – continued from previous page

Date (UT)	Δ t / days	Telescope & Instrument	Filter	Exposure time /s	Photometry /mag
2018 May 07.221	9.231	AAVSO RRIB	r'		7.943 ± 0.003
2018 May 07.221	9.231	AAVSO RBRB	r'		7.962 ± 0.003
2018 May 07.803	9.813	AAVSO VMAG	r'		8.137 ± 0.020
2018 May 07.845	9.855	AAVSO BRIA	r'		9.019 ± 0.068
2018 May 07.847	9.857	AAVSO BRIA	r'		8.946 ± 0.032
2018 May 07.849	9.859	AAVSO BRIA	r'		8.981 ± 0.052
2018 May 07.851	9.861	AAVSO BRIA	r'		9.020 ± 0.079
2018 May 07.853	9.863	AAVSO DPA	r'		7.976 ± 0.043
2018 May 07.853	9.863	AAVSO BRIA	r'		9.011 ± 0.055
2018 May 07.855	9.865	AAVSO BRIA	r'		8.939 ± 0.023
2018 May 07.857	9.867	AAVSO BRIA	r'		8.991 ± 0.083
2018 May 07.859	9.869	AAVSO BRIA	r'		9.003 ± 0.077
2018 May 07.862	9.872	AAVSO BRIA	r'		8.993 ± 0.035
2018 May 07.864	9.874	AAVSO BRIA	r'		8.956 ± 0.071
2018 May 08.849	10.859	AAVSO BRIA	r'		9.172 ± 0.107
2018 May 08.851	10.861	AAVSO BRIA	r'		9.133 ± 0.049
2018 May 08.853	10.863	AAVSO BRIA	r'		9.292 ± 0.120
2018 May 08.855	10.865	AAVSO BRIA	r'		9.314 ± 0.074
2018 May 08.862	10.872	AAVSO BRIA	r'		9.233 ± 0.069
2018 May 08.865	10.875	AAVSO BRIA	r'		9.262 ± 0.105
2018 May 08.868	10.878	AAVSO BRIA	r'		9.183 ± 0.067
2018 May 08.870	10.880	AAVSO BRIA	r'		9.194 ± 0.029
2018 May 09.858	11.868	AAVSO BRIA	r'		9.348 ± 0.154
2018 May 09.860	11.870	AAVSO BRIA	r'		9.172 ± 0.111
2018 May 09.862	11.872	AAVSO BRIA	r'		9.223 ± 0.135
2018 May 09.864	11.874	AAVSO BRIA	r'		9.204 ± 0.087
2018 May 09.866	11.876	AAVSO BRIA	r'		9.328 ± 0.135
2018 May 09.868	11.878	AAVSO BRIA	r'		9.245 ± 0.149
2018 May 10.190	12.200	AAVSO RBRB	r'		8.392 ± 0.004
2018 May 10.190	12.200	AAVSO STYA	r'		8.402 ± 0.004
2018 May 10.886	12.896	AAVSO AFSA	r'		8.790 ± 0.007
2018 May 10.887	12.897	AAVSO AFSA	r'		8.674 ± 0.007
2018 May 10.887	12.897	AAVSO AFSA	r'		8.645 ± 0.007
2018 May 12.184	14.194	AAVSO SSTA	r'		8.794 ± 0.009
2018 May 12.804	14.814	AAVSO VMAG	r'		8.950 ± 0.020
2018 May 12.847	14.857	AAVSO ETOA	r'		8.947 ± 0.014
2018 May 12.849	14.859	AAVSO ETOA	r'		8.907 ± 0.055
2018 May 12.851	14.861	AAVSO ETOA	r'		8.901 ± 0.055
2018 May 12.853	14.863	AAVSO ETOA	r'		8.878 ± 0.007
2018 May 12.855	14.865	AAVSO ETOA	r'		8.897 ± 0.035
2018 May 12.860	14.870	AAVSO AFSA	r'		9.030 ± 0.006
2018 May 12.860	14.870	AAVSO AFSA	r'		9.091 ± 0.006
2018 May 12.860	14.870	AAVSO AFSA	r'		9.025 ± 0.006
2018 May 12.865	14.875	AAVSO BRIA	r'		9.953 ± 0.216
2018 May 13.217	15.227	AAVSO LRCA	r'		9.012 ± 0.009
2018 May 13.217	15.227	AAVSO LRCA	r'		8.809 ± 0.004
2018 May 13.218	15.228	AAVSO RBRB	r'		9.027 ± 0.003
2018 May 13.219	15.229	AAVSO STYA	r'		8.988 ± 0.002
2018 May 13.905	15.915	AAVSO BRIA	r'		10.099 ± 0.074
2018 May 13.907	15.917	AAVSO BRIA	r'		10.101 ± 0.150
2018 May 13.911	15.921	AAVSO BRIA	r'		10.135 ± 0.022
2018 May 13.913	15.923	AAVSO BRIA	r'		10.123 ± 0.108
2018 May 13.916	15.926	AAVSO BRIA	r'		10.083 ± 0.060
2018 May 13.918	15.928	AAVSO BRIA	r'		10.148 ± 0.087
2018 May 14.201	16.211	AAVSO STYA	r'		9.146 ± 0.002
2018 May 14.208	16.218	AAVSO RBRB	r'		8.992 ± 0.002
2018 May 14.857	16.867	AAVSO BRIA	r'		10.241 ± 0.059
2018 May 14.864	16.874	AAVSO AFSA	r'		9.480 ± 0.008

Table A3 – continued from previous page

Date (UT)	Δ t / days	Telescope & Instrument	Filter	Exposure time /s	Photometry /mag
2018 May 14.864	16.874	AAVSO AFSA	r'		9.480 ± 0.008
2018 May 14.864	16.874	AAVSO AFSA	r'		9.367 ± 0.007
2018 May 14.864	16.874	AAVSO AFSA	r'		9.367 ± 0.007
2018 May 14.864	16.874	AAVSO AFSA	r'		9.384 ± 0.007
2018 May 14.864	16.874	AAVSO AFSA	r'		9.384 ± 0.007
2018 May 14.868	16.878	AAVSO BRIA	r'		10.273 ± 0.055
2018 May 18.840	20.850	AAVSO NRNA	r'		10.096 ± 0.006
2018 May 18.843	20.853	AAVSO NRNA	r'		10.336 ± 0.006
2018 May 19.206	21.216	AAVSO RBRB	r'		10.045 ± 0.007
2018 May 20.848	22.858	AAVSO NRNA	r'		10.389 ± 0.024
2018 May 20.877	22.887	AAVSO BRIA	r'		11.084 ± 0.138
2018 May 21.222	23.232	AAVSO RBRB	r'		10.264 ± 0.005
2018 May 22.855	24.865	AAVSO NRNA	r'		10.697 ± 0.007
2018 May 31.869	33.879	AAVSO AFSA	r'		11.266 ± 0.024
2018 May 31.870	33.880	AAVSO AFSA	r'		11.041 ± 0.022
2018 May 31.870	33.880	AAVSO AFSA	r'		11.201 ± 0.023
2018 Jul 14.370	77.380	AAVSO MRV	r'		13.154 ± 0.059
2018 Jul 14.477	77.487	AAVSO SGEA	r'		13.103 ± 0.052
2018 Jul 16.497	79.507	AAVSO SGEA	r'		13.314 ± 0.076
2018 Jul 17.472	80.482	AAVSO SGEA	r'		13.446 ± 0.026
2018 Jul 18.477	81.487	AAVSO SGEA	r'		13.434 ± 0.030
2018 Jul 19.345	82.355	AAVSO CDJA	r'		13.335 ± 0.008
2018 Jul 19.346	82.356	AAVSO CDJA	r'		13.344 ± 0.008
2018 Jul 19.347	82.357	AAVSO CDJA	r'		13.315 ± 0.008
2018 Jul 19.363	82.373	AAVSO MRV	r'		13.460 ± 0.039
2018 Jul 21.194	84.204	LT IO:O	r'	3 × 30	13.525 ± 0.007
2018 Jul 21.454	84.464	AAVSO SGEA	r'		13.540 ± 0.024
2018 Jul 22.219	85.229	LT IO:O	r'	3 × 30	13.594 ± 0.007
2018 Jul 23.196	86.206	LT IO:O	r'	3 × 30	13.598 ± 0.006
2018 Jul 24.187	87.197	LT IO:O	r'	3 × 30	13.610 ± 0.007
2018 Jul 25.184	88.194	LT IO:O	r'	3 × 30	13.710 ± 0.007
2018 Jul 26.192	89.202	LT IO:O	r'	3 × 30	13.719 ± 0.010
2018 Jul 27.184	90.194	LT IO:O	r'	3 × 30	13.587 ± 0.009
2018 Jul 28.177	91.187	LT IO:O	r'	3 × 30	13.782 ± 0.008
2018 Jul 29.176	92.186	LT IO:O	r'	3 × 30	13.850 ± 0.011
2018 Jul 31.170	94.180	LT IO:O	r'	3 × 30	13.857 ± 0.007
2018 Aug 01.184	95.194	LT IO:O	r'	3 × 30	13.834 ± 0.008
2018 Aug 02.161	96.171	LT IO:O	r'	3 × 30	13.776 ± 0.007
2018 Aug 02.336	96.346	AAVSO CDJA	r'		13.751 ± 0.007
2018 Aug 02.337	96.347	AAVSO CDJA	r'		13.749 ± 0.007
2018 Aug 02.339	96.349	AAVSO CDJA	r'		13.731 ± 0.008
2018 Aug 02.487	96.497	AAVSO SGEA	r'		13.828 ± 0.028
2018 Aug 03.159	97.169	LT IO:O	r'	3 × 30	13.935 ± 0.007
2018 Aug 03.484	97.494	AAVSO SGEA	r'		13.886 ± 0.031
2018 Aug 04.149	98.159	AAVSO MRV	r'		13.977 ± 0.053
2018 Aug 06.150	100.160	LT IO:O	r'	3 × 30	13.934 ± 0.007
2018 Aug 06.494	100.504	AAVSO SGEA	r'		13.932 ± 0.023
2018 Aug 08.166	102.176	LT IO:O	r'	3 × 30	13.992 ± 0.007
2018 Aug 09.324	103.334	AAVSO BMSA	r'		13.908 ± 0.008
2018 Aug 09.325	103.335	AAVSO BMSA	r'		13.896 ± 0.008
2018 Aug 09.326	103.336	AAVSO BMSA	r'		13.900 ± 0.008
2018 Aug 10.172	104.182	LT IO:O	r'	3 × 30	14.038 ± 0.005
2018 Aug 10.481	104.491	AAVSO SGEA	r'		13.965 ± 0.045
2018 Aug 13.174	107.184	LT IO:O	r'	3 × 30	14.130 ± 0.017
2018 Aug 13.317	107.327	AAVSO BMSA	r'		14.119 ± 0.010
2018 Aug 13.318	107.328	AAVSO BMSA	r'		14.135 ± 0.011
2018 Aug 13.319	107.329	AAVSO BMSA	r'		14.125 ± 0.010
2018 Aug 13.337	107.347	AAVSO MRV	r'		14.081 ± 0.055

Continued on next page

Table A3 – continued from previous page

Date (UT)	Δ t / days	Telescope & Instrument	Filter	Exposure time /s	Photometry /mag
2018 Aug 13.473	107.483	AAVSO SGEA	r'		14.037 ± 0.028
2018 Aug 14.420	108.430	AAVSO SGEA	r'		14.024 ± 0.029
2018 Aug 15.448	109.458	AAVSO SGEA	r'		14.095 ± 0.029
2018 Aug 16.124	110.134	LT IO:O	r'	3×30	14.094 ± 0.007
2018 Aug 16.450	110.460	AAVSO SGEA	r'		14.242 ± 0.027
2018 Aug 17.443	111.453	AAVSO SGEA	r'		14.017 ± 0.025
2018 Aug 18.410	112.420	AAVSO SGEA	r'		14.041 ± 0.027
2018 Aug 19.167	113.177	LT IO:O	r'	3×30	14.080 ± 0.007
2018 Aug 19.448	113.458	AAVSO SGEA	r'		14.057 ± 0.025
2018 Aug 20.187	114.197	AAVSO MRV	r'		14.091 ± 0.047
2018 Aug 20.418	114.428	AAVSO SGEA	r'		13.986 ± 0.024
2018 Aug 22.219	116.229	LT IO:O	r'	3×30	14.031 ± 0.006
2018 Aug 22.441	116.451	AAVSO SGEA	r'		13.994 ± 0.024
2018 Aug 23.472	117.482	AAVSO SGEA	r'		14.011 ± 0.023
2018 Aug 25.099	119.109	LT IO:O	r'	3×30	14.157 ± 0.007
2018 Aug 26.515	120.525	AAVSO SGEA	r'		14.033 ± 0.028
2018 Aug 27.107	121.117	AAVSO MRV	r'		14.123 ± 0.039
2018 Aug 27.516	121.526	AAVSO SGEA	r'		14.047 ± 0.028
2018 Aug 28.109	122.119	LT IO:O	r'	3×30	14.049 ± 0.009
2018 Aug 28.522	122.532	AAVSO SGEA	r'		14.034 ± 0.031
2018 Aug 29.512	123.522	AAVSO SGEA	r'		14.174 ± 0.030
2018 Aug 30.520	124.530	AAVSO SGEA	r'		14.035 ± 0.040
2018 Aug 31.087	125.097	LT IO:O	r'	3×30	14.088 ± 0.009
2018 Aug 31.515	125.525	AAVSO SGEA	r'		13.953 ± 0.025
2018 Sep 02.517	127.527	AAVSO SGEA	r'		14.267 ± 0.034
2018 Sep 03.075	128.085	LT IO:O	r'	3×30	14.176 ± 0.007
2018 Sep 03.507	128.517	AAVSO SGEA	r'		14.077 ± 0.032
2018 Sep 04.520	129.530	AAVSO SGEA	r'		14.199 ± 0.029
2018 Sep 05.513	130.523	AAVSO SGEA	r'		14.132 ± 0.026
2018 Sep 06.067	131.077	LT IO:O	r'	3×30	14.180 ± 0.006
2018 Sep 06.503	131.513	AAVSO SGEA	r'		14.124 ± 0.026
2018 Sep 07.497	132.507	AAVSO SGEA	r'		14.212 ± 0.030
2018 Sep 08.510	133.520	AAVSO SGEA	r'		14.243 ± 0.026
2018 Sep 09.056	134.066	LT IO:O	r'	3×30	14.286 ± 0.007
2018 Sep 09.531	134.541	AAVSO SGEA	r'		14.160 ± 0.031
2018 Sep 11.530	136.540	AAVSO SGEA	r'		14.251 ± 0.035
2018 Sep 12.064	137.074	LT IO:O	r'	3×30	14.341 ± 0.007
2018 Sep 13.527	138.537	AAVSO SGEA	r'		14.213 ± 0.030
2018 Sep 15.291	140.301	AAVSO MRV	r'		14.417 ± 0.037
2018 Sep 16.540	141.550	AAVSO SGEA	r'		14.201 ± 0.048
2018 Sep 18.088	143.098	LT IO:O	r'	3×30	14.355 ± 0.006
2018 Sep 23.020	148.030	LT IO:O	r'	3×30	14.459 ± 0.012
2018 Sep 26.016	151.026	LT IO:O	r'	3×30	14.448 ± 0.007
2018 Sep 29.059	154.069	LT IO:O	r'	3×30	14.430 ± 0.007
2018 Oct 02.014	157.024	LT IO:O	r'	3×30	14.496 ± 0.007
2018 Nov 01.113	187.123	LT IO:O	r'	3×30	14.781 ± 0.006
2018 Nov 05.149	191.159	AAVSO MRV	r'		14.829 ± 0.037
2018 Nov 08.161	194.171	LT IO:O	r'	3×30	14.781 ± 0.006
2018 Nov 16.119	202.129	LT IO:O	r'	3×30	14.761 ± 0.007
2018 Nov 26.026	212.036	LT IO:O	r'	3×30	14.688 ± 0.008
2018 Dec 10.066	226.076	LT IO:O	r'	3×30	14.733 ± 0.006
2018 Dec 15.965	231.975	LT IO:O	r'	3×30	14.753 ± 0.006
2018 Dec 22.841	238.851	LT IO:O	r'	3×30	14.814 ± 0.012
2018 Dec 28.896	244.906	LT IO:O	r'	3×30	14.886 ± 0.011
2018 Dec 28.965	244.975	AAVSO MRV	r'		14.826 ± 0.033
2019 Jan 04.921	251.931	LT IO:O	r'	3×30	14.881 ± 0.007
2019 Jan 10.975	257.985	LT IO:O	r'	3×30	14.840 ± 0.006
2019 Jan 11.071	258.081	AAVSO MRV	r'		14.791 ± 0.030

Table A3 – continued from previous page

Date (UT)	Δ t / days	Telescope & Instrument	Filter	Exposure time /s	Photometry /mag
2019 Jan 19.989	266.999	LT IO:O	r'	3×30	14.820 ± 0.007
2019 Jan 25.904	272.914	LT IO:O	r'	3×30	14.749 ± 0.007
2019 Jan 31.903	278.913	AAVSO MRV	r'		14.629 ± 0.035
2019 Jan 31.940	278.950	LT IO:O	r'	3×30	14.629 ± 0.007
2019 Feb 06.890	284.900	LT IO:O	r'	3×30	14.808 ± 0.008
2019 Feb 12.876	290.886	LT IO:O	r'	3×30	14.869 ± 0.006
2019 Feb 12.943	290.953	AAVSO MRV	r'		14.811 ± 0.037
2019 Feb 19.901	297.911	LT IO:O	r'	3×30	14.890 ± 0.020
2019 Feb 28.890	306.900	LT IO:O	r'	3×30	14.925 ± 0.007
2019 Mar 04.962	310.972	AAVSO MRV	r'		14.812 ± 0.035
2019 Mar 16.848	322.858	LT IO:O	r'	3×30	14.849 ± 0.007
2019 Apr 08.861	345.871	LT IO:O	r'	3×30	14.892 ± 0.007
2019 Apr 25.853	362.863	LT IO:O	r'	3×30	14.878 ± 0.009
2019 Jul 19.217	447.227	LT IO:O	r'	3×30	14.823 ± 0.007
2019 Aug 01.220	460.230	LT IO:O	r'	3×30	14.856 ± 0.006
2019 Aug 19.127	478.137	LT IO:O	r'	3×30	14.843 ± 0.008
2019 Sep 14.116	504.126	LT IO:O	r'	3×60	14.799 ± 0.009
2019 Oct 14.980	534.990	LT IO:O	r'	3×60	14.770 ± 0.008
2019 Nov 16.940	567.950	LT IO:O	r'	3×60	14.438 ± 0.010
2019 Dec 09.908	590.918	LT IO:O	r'	3×60	14.760 ± 0.008
2020 Aug 31.172	856.182	LT IO:O	r'	3×120	14.968 ± 0.005
2021 Feb 02.872	1011.882	LT IO:O	r'	3×180	14.653 ± 0.005
2018 Apr 30.807	2.817	AAVSO VMAG	i'		5.730 ± 0.020
2018 May 01.148	3.158	AAVSO SSTA	i'		5.929 ± 0.002
2018 May 01.162	3.172	AAVSO STYA	i'		6.005 ± 0.001
2018 May 01.162	3.172	AAVSO RBRB	i'		6.016 ± 0.001
2018 May 01.860	3.870	AAVSO NRNA	i'		6.795 ± 0.011
2018 May 02.845	4.855	AAVSO NRNA	i'		7.524 ± 0.012
2018 May 04.168	6.178	AAVSO RBRB	i'		7.217 ± 0.001
2018 May 04.808	6.818	AAVSO VMAG	i'		7.356 ± 0.020
2018 May 04.821	6.831	AAVSO ETOA	i'		7.349 ± 0.174
2018 May 04.821	6.831	AAVSO ETOA	i'		7.365 ± 0.096
2018 May 04.827	6.837	AAVSO ETOA	i'		7.414 ± 0.091
2018 May 04.828	6.838	AAVSO ETOA	i'		7.399 ± 0.143
2018 May 04.829	6.839	AAVSO ETOA	i'		7.408 ± 0.089
2018 May 04.830	6.840	AAVSO ETOA	i'		7.394 ± 0.095
2018 May 05.180	7.190	AAVSO RBRB	i'		7.418 ± 0.002
2018 May 05.199	7.209	AAVSO STYA	i'		7.329 ± 0.002
2018 May 05.829	7.839	AAVSO NRNA	i'		7.902 ± 0.003
2018 May 05.867	7.877	AAVSO DPA	i'		7.246 ± 0.027
2018 May 05.896	7.906	AAVSO MIW	i'		7.787 ± 0.026
2018 May 06.892	8.902	AAVSO MIW	i'		7.999 ± 0.015
2018 May 07.162	9.172	AAVSO STYA	i'		7.535 ± 0.004
2018 May 07.185	9.195	AAVSO RRIB	i'		7.617 ± 0.001
2018 May 07.185	9.195	AAVSO RBRB	i'		7.619 ± 0.001
2018 May 07.803	9.813	AAVSO VMAG	i'		7.777 ± 0.020
2018 May 07.855	9.865	AAVSO DPA	i'		7.558 ± 0.070
2018 May 07.897	9.907	AAVSO MIW	i'		7.875 ± 0.035
2018 May 10.172	12.182	AAVSO RBRB	i'		8.084 ± 0.005
2018 May 10.172	12.182	AAVSO STYA	i'		8.084 ± 0.004
2018 May 12.165	14.175	AAVSO SSTA	i'		8.516 ± 0.003
2018 May 12.804	14.814	AAVSO VMAG	i'		8.732 ± 0.020
2018 May 12.848	14.858	AAVSO ETOA	i'		8.645 ± 0.125
2018 May 12.849	14.859	AAVSO ETOA	i'		8.676 ± 0.025
2018 May 12.851	14.861	AAVSO ETOA	i'		8.688 ± 0.015
2018 May 12.853	14.863	AAVSO ETOA	i'		8.605 ± 0.027
2018 May 12.855	14.865	AAVSO ETOA	i'		8.705 ± 0.017
2018 May 13.181	15.191	AAVSO RBRB	i'		8.820 ± 0.002

Continued on next page

Table A3 – continued from previous page

Date (UT)	Δ t / days	Telescope & Instrument	Filter	Exposure time /s	Photometry /mag
2018 May 13.181	15.191	AAVSO LRCA	i'		8.811 ± 0.003
2018 May 13.187	15.197	AAVSO STYA	i'		8.767 ± 0.001
2018 May 14.209	16.219	AAVSO RBRB	i'		9.038 ± 0.002
2018 May 14.211	16.221	AAVSO STYA	i'		8.995 ± 0.002
2018 May 16.230	18.240	AAVSO RBRB	i'		9.535 ± 0.007
2018 May 18.844	20.854	AAVSO NRNA	i'		10.439 ± 0.009
2018 May 19.222	21.232	AAVSO RBRB	i'		10.136 ± 0.005
2018 May 21.189	23.199	AAVSO RBRB	i'		10.262 ± 0.004
2018 Jun 30.374	63.384	AAVSO MRV	i'		12.471 ± 0.061
2018 Jul 07.369	70.379	AAVSO MRV	i'		12.531 ± 0.080
2018 Jul 09.365	72.375	AAVSO MRV	i'		12.711 ± 0.049
2018 Jul 14.365	77.375	AAVSO MRV	i'		12.895 ± 0.066
2018 Jul 14.478	77.488	AAVSO SGEA	i'		12.942 ± 0.058
2018 Jul 17.473	80.483	AAVSO SGEA	i'		13.168 ± 0.040
2018 Jul 18.478	81.488	AAVSO SGEA	i'		13.230 ± 0.052
2018 Jul 19.356	82.366	AAVSO CDJA	i'		12.989 ± 0.006
2018 Jul 19.357	82.367	AAVSO CDJA	i'		12.984 ± 0.006
2018 Jul 19.358	82.368	AAVSO CDJA	i'		12.989 ± 0.006
2018 Jul 19.359	82.369	AAVSO MRV	i'		13.140 ± 0.045
2018 Jul 21.196	84.206	LT IO:O	i'	3 × 30	13.316 ± 0.006
2018 Jul 21.455	84.465	AAVSO SGEA	i'		13.256 ± 0.033
2018 Jul 22.220	85.230	LT IO:O	i'	3 × 30	13.370 ± 0.006
2018 Jul 23.198	86.208	LT IO:O	i'	3 × 30	13.360 ± 0.006
2018 Jul 24.189	87.199	LT IO:O	i'	3 × 30	13.380 ± 0.006
2018 Jul 25.185	88.195	LT IO:O	i'	3 × 30	13.507 ± 0.007
2018 Jul 26.194	89.204	LT IO:O	i'	3 × 30	13.481 ± 0.009
2018 Jul 27.186	90.196	LT IO:O	i'	3 × 30	13.392 ± 0.009
2018 Jul 28.179	91.189	LT IO:O	i'	3 × 30	13.542 ± 0.006
2018 Jul 29.178	92.188	LT IO:O	i'	3 × 30	13.579 ± 0.008
2018 Jul 31.172	94.182	LT IO:O	i'	3 × 30	13.577 ± 0.008
2018 Aug 01.186	95.196	LT IO:O	i'	3 × 30	13.543 ± 0.009
2018 Aug 02.163	96.173	LT IO:O	i'	3 × 30	13.503 ± 0.008
2018 Aug 02.350	96.360	AAVSO CDJA	i'		13.353 ± 0.005
2018 Aug 02.352	96.362	AAVSO CDJA	i'		13.362 ± 0.005
2018 Aug 02.353	96.363	AAVSO CDJA	i'		13.355 ± 0.005
2018 Aug 02.488	96.498	AAVSO SGEA	i'		13.510 ± 0.027
2018 Aug 03.161	97.171	LT IO:O	i'	3 × 30	13.675 ± 0.007
2018 Aug 03.485	97.495	AAVSO SGEA	i'		13.560 ± 0.039
2018 Aug 06.152	100.162	LT IO:O	i'	3 × 30	13.683 ± 0.007
2018 Aug 06.494	100.504	AAVSO SGEA	i'		13.609 ± 0.033
2018 Aug 08.168	102.178	LT IO:O	i'	3 × 30	13.718 ± 0.006
2018 Aug 09.328	103.338	AAVSO BMSA	i'		13.499 ± 0.005
2018 Aug 09.329	103.339	AAVSO BMSA	i'		13.523 ± 0.005
2018 Aug 09.330	103.340	AAVSO BMSA	i'		13.519 ± 0.005
2018 Aug 10.174	104.184	LT IO:O	i'	3 × 30	13.746 ± 0.007
2018 Aug 10.482	104.492	AAVSO SGEA	i'		13.563 ± 0.037
2018 Aug 13.177	107.187	LT IO:O	i'	3 × 30	13.764 ± 0.015
2018 Aug 13.330	107.340	AAVSO MRV	i'		13.811 ± 0.041
2018 Aug 13.336	107.346	AAVSO BMSA	i'		13.717 ± 0.005
2018 Aug 13.337	107.347	AAVSO BMSA	i'		13.722 ± 0.005
2018 Aug 13.338	107.348	AAVSO BMSA	i'		13.701 ± 0.005
2018 Aug 13.474	107.484	AAVSO SGEA	i'		13.752 ± 0.039
2018 Aug 14.420	108.430	AAVSO SGEA	i'		13.702 ± 0.042
2018 Aug 15.449	109.459	AAVSO SGEA	i'		13.636 ± 0.038
2018 Aug 16.126	110.136	LT IO:O	i'	3 × 30	13.799 ± 0.007
2018 Aug 16.451	110.461	AAVSO SGEA	i'		13.828 ± 0.041
2018 Aug 17.443	111.453	AAVSO SGEA	i'		13.793 ± 0.037
2018 Aug 18.411	112.421	AAVSO SGEA	i'		13.753 ± 0.039

Continued on next page

Table A3 – continued from previous page

Date (UT)	Δ t / days	Telescope & Instrument	Filter	Exposure time /s	Photometry /mag
2018 Aug 19.169	113.179	LT IO:O	i'	3×30	13.778 ± 0.007
2018 Aug 19.448	113.458	AAVSO SGEA	i'		13.676 ± 0.040
2018 Aug 20.418	114.428	AAVSO SGEA	i'		13.630 ± 0.034
2018 Aug 21.433	115.443	AAVSO SGEA	i'		13.598 ± 0.042
2018 Aug 22.221	116.231	LT IO:O	i'	3×30	13.699 ± 0.006
2018 Aug 22.442	116.452	AAVSO SGEA	i'		13.671 ± 0.033
2018 Aug 23.473	117.483	AAVSO SGEA	i'		13.725 ± 0.035
2018 Aug 25.101	119.111	LT IO:O	i'	3×30	13.832 ± 0.006
2018 Aug 26.516	120.526	AAVSO SGEA	i'		13.680 ± 0.039
2018 Aug 27.516	121.526	AAVSO SGEA	i'		13.628 ± 0.037
2018 Aug 28.111	122.121	LT IO:O	i'	3×30	13.744 ± 0.009
2018 Aug 28.523	122.533	AAVSO SGEA	i'		13.726 ± 0.044
2018 Aug 29.513	123.523	AAVSO SGEA	i'		13.814 ± 0.043
2018 Aug 30.520	124.530	AAVSO SGEA	i'		13.611 ± 0.048
2018 Aug 31.088	125.098	LT IO:O	i'	3×30	13.776 ± 0.007
2018 Aug 31.516	125.526	AAVSO SGEA	i'		13.658 ± 0.036
2018 Sep 02.517	127.527	AAVSO SGEA	i'		13.776 ± 0.048
2018 Sep 03.077	128.087	LT IO:O	i'	3×30	13.815 ± 0.007
2018 Sep 03.508	128.518	AAVSO SGEA	i'		13.712 ± 0.043
2018 Sep 04.520	129.530	AAVSO SGEA	i'		13.783 ± 0.038
2018 Sep 05.513	130.523	AAVSO SGEA	i'		13.785 ± 0.039
2018 Sep 06.069	131.079	LT IO:O	i'	3×30	13.863 ± 0.006
2018 Sep 06.504	131.514	AAVSO SGEA	i'		13.746 ± 0.035
2018 Sep 07.497	132.507	AAVSO SGEA	i'		13.919 ± 0.046
2018 Sep 08.510	133.520	AAVSO SGEA	i'		13.892 ± 0.037
2018 Sep 09.058	134.068	LT IO:O	i'	3×30	13.957 ± 0.006
2018 Sep 09.532	134.542	AAVSO SGEA	i'		13.802 ± 0.043
2018 Sep 11.531	136.541	AAVSO SGEA	i'		13.793 ± 0.045
2018 Sep 12.066	137.076	LT IO:O	i'	3×30	13.987 ± 0.008
2018 Sep 13.527	138.537	AAVSO SGEA	i'		13.803 ± 0.040
2018 Sep 14.539	139.549	AAVSO SGEA	i'		13.872 ± 0.064
2018 Sep 15.278	140.288	AAVSO MRV	i'		13.957 ± 0.045
2018 Sep 18.090	143.100	LT IO:O	i'	3×30	14.022 ± 0.006
2018 Sep 23.022	148.032	LT IO:O	i'	3×30	14.056 ± 0.010
2018 Sep 26.017	151.027	LT IO:O	i'	3×30	14.099 ± 0.008
2018 Sep 29.061	154.071	LT IO:O	i'	3×30	14.093 ± 0.006
2018 Oct 02.016	157.026	LT IO:O	i'	3×30	14.151 ± 0.006
2018 Nov 01.115	187.125	LT IO:O	i'	3×30	14.371 ± 0.006
2018 Nov 08.163	194.173	LT IO:O	i'	3×30	14.364 ± 0.006
2018 Nov 16.121	202.131	LT IO:O	i'	3×30	14.340 ± 0.006
2018 Nov 26.027	212.037	LT IO:O	i'	3×30	14.270 ± 0.007
2018 Nov 26.318	212.328	AAVSO MRV	i'		14.247 ± 0.042
2018 Dec 10.068	226.078	LT IO:O	i'	3×30	14.313 ± 0.005
2018 Dec 15.967	231.977	LT IO:O	i'	3×30	14.336 ± 0.009
2018 Dec 22.843	238.853	LT IO:O	i'	3×30	14.427 ± 0.009
2018 Dec 28.897	244.907	LT IO:O	i'	3×30	14.396 ± 0.010
2019 Jan 04.923	251.933	LT IO:O	i'	3×30	14.423 ± 0.005
2019 Jan 10.976	257.986	LT IO:O	i'	3×30	14.404 ± 0.006
2019 Jan 19.991	267.001	LT IO:O	i'	3×30	14.365 ± 0.007
2019 Jan 25.906	272.916	LT IO:O	i'	3×30	14.320 ± 0.006
2019 Jan 31.942	278.952	LT IO:O	i'	3×30	14.168 ± 0.006
2019 Feb 06.892	284.902	LT IO:O	i'	3×30	14.370 ± 0.007
2019 Feb 12.878	290.888	LT IO:O	i'	3×30	14.431 ± 0.007
2019 Feb 19.903	297.913	LT IO:O	i'	3×30	14.433 ± 0.012
2019 Feb 28.892	306.902	LT IO:O	i'	3×30	14.480 ± 0.007
2019 Mar 16.850	322.860	LT IO:O	i'	3×30	14.402 ± 0.006
2019 Apr 08.863	345.873	LT IO:O	i'	3×30	14.456 ± 0.007
2019 Apr 25.855	362.865	LT IO:O	i'	3×30	14.372 ± 0.007

Table A3 – continued from previous page

Date (UT)	Δ t / days	Telescope & Instrument	Filter	Exposure time /s	Photometry /mag
2019 Jul 19.219	447.229	LT IO:O	i'	3×30	14.367 ± 0.008
2019 Aug 01.222	460.232	LT IO:O	i'	3×30	14.379 ± 0.006
2019 Aug 19.129	478.139	LT IO:O	i'	3×30	14.344 ± 0.008
2019 Sep 14.119	504.129	LT IO:O	i'	3×60	14.354 ± 0.009
2019 Oct 14.983	534.993	LT IO:O	i'	3×60	14.280 ± 0.007
2019 Nov 16.943	567.953	LT IO:O	i'	3×60	14.048 ± 0.006
2019 Nov 17.199	568.209	LCO	i'	1×180	13.892 ± 0.031
2019 Nov 17.201	568.211	LCO	i'	1×180	13.838 ± 0.025
2019 Nov 17.203	568.213	LCO	i'	1×180	13.900 ± 0.026
2019 Nov 17.206	568.216	LCO	i'	1×180	14.082 ± 0.021
2019 Nov 17.208	568.218	LCO	i'	1×180	14.124 ± 0.018
2019 Nov 17.211	568.221	LCO	i'	1×180	14.050 ± 0.022
2019 Nov 17.213	568.223	LCO	i'	1×180	14.171 ± 0.015
2019 Nov 17.215	568.225	LCO	i'	1×180	14.149 ± 0.015
2019 Nov 17.218	568.228	LCO	i'	1×180	14.139 ± 0.013
2019 Nov 17.220	568.230	LCO	i'	1×180	14.200 ± 0.009
2019 Nov 17.223	568.233	LCO	i'	1×180	14.191 ± 0.008
2019 Nov 17.225	568.235	LCO	i'	1×180	14.197 ± 0.008
2019 Nov 17.228	568.238	LCO	i'	1×300	13.131 ± 0.052
2019 Nov 17.231	568.241	LCO	i'	1×300	13.034 ± 0.049
2019 Nov 17.235	568.245	LCO	i'	1×300	13.149 ± 0.045
2019 Nov 18.287	569.297	LCO	i'	1×180	14.135 ± 0.006
2019 Nov 18.289	569.299	LCO	i'	1×180	14.137 ± 0.005
2019 Nov 18.291	569.301	LCO	i'	1×180	14.144 ± 0.005
2019 Nov 18.292	569.302	LCO	i'	1×180	14.140 ± 0.006
2019 Nov 18.294	569.304	LCO	i'	1×180	14.159 ± 0.006
2019 Nov 18.297	569.307	LCO	i'	1×180	14.148 ± 0.007
2019 Nov 18.320	569.330	LCO	i'	1×180	14.073 ± 0.007
2019 Nov 18.322	569.332	LCO	i'	1×180	14.092 ± 0.007
2019 Nov 18.325	569.335	LCO	i'	1×180	14.071 ± 0.007
2019 Nov 18.356	569.366	LCO	i'	1×180	14.057 ± 0.008
2019 Nov 18.358	569.368	LCO	i'	1×180	14.065 ± 0.008
2019 Nov 18.361	569.371	LCO	i'	1×180	14.062 ± 0.008
2019 Nov 18.456	569.466	LCO	i'	1×180	14.151 ± 0.008
2019 Nov 18.458	569.468	LCO	i'	1×180	14.148 ± 0.007
2019 Nov 18.461	569.471	LCO	i'	1×180	14.114 ± 0.007
2019 Nov 18.490	569.500	LCO	i'	1×180	14.110 ± 0.007
2019 Nov 18.493	569.503	LCO	i'	1×180	14.093 ± 0.008
2019 Nov 18.495	569.505	LCO	i'	1×180	14.113 ± 0.009
2019 Nov 19.168	570.178	LCO	i'	1×180	14.069 ± 0.006
2019 Nov 19.171	570.181	LCO	i'	1×180	14.078 ± 0.005
2019 Nov 19.173	570.183	LCO	i'	1×180	14.094 ± 0.007
2019 Nov 19.188	570.198	LCO	i'	1×180	14.154 ± 0.011
2019 Nov 19.191	570.201	LCO	i'	1×180	14.140 ± 0.009
2019 Nov 19.193	570.203	LCO	i'	1×143	14.128 ± 0.008
2019 Nov 19.237	570.247	LCO	i'	1×180	14.072 ± 0.007
2019 Nov 19.239	570.249	LCO	i'	1×180	14.113 ± 0.007
2019 Nov 19.241	570.251	LCO	i'	1×180	14.132 ± 0.006
2019 Nov 19.278	570.288	LCO	i'	1×180	14.132 ± 0.008
2019 Nov 19.280	570.290	LCO	i'	1×180	14.131 ± 0.007
2019 Nov 19.283	570.293	LCO	i'	1×180	14.131 ± 0.010
2019 Nov 19.320	570.330	LCO	i'	1×180	14.081 ± 0.007
2019 Nov 19.322	570.332	LCO	i'	1×180	14.119 ± 0.006
2019 Nov 19.325	570.335	LCO	i'	1×180	14.128 ± 0.006
2019 Nov 19.355	570.365	LCO	i'	1×180	14.131 ± 0.008
2019 Nov 19.357	570.367	LCO	i'	1×180	14.113 ± 0.007
2019 Nov 19.359	570.369	LCO	i'	1×180	14.077 ± 0.006
2019 Nov 19.396	570.406	LCO	i'	1×180	14.202 ± 0.007

Table A3 – continued from previous page

Date (UT)	Δ t / days	Telescope & Instrument	Filter	Exposure time /s	Photometry /mag
2019 Nov 19.398	570.408	LCO	i'	1×180	14.167 ± 0.008
2019 Nov 19.401	570.411	LCO	i'	1×180	14.153 ± 0.007
2019 Nov 19.406	570.416	LCO	i'	1×180	14.142 ± 0.008
2019 Nov 19.409	570.419	LCO	i'	1×180	14.117 ± 0.008
2019 Nov 19.411	570.421	LCO	i'	1×180	14.119 ± 0.007
2019 Nov 19.438	570.448	LCO	i'	1×180	14.097 ± 0.010
2019 Nov 19.440	570.450	LCO	i'	1×180	14.091 ± 0.011
2019 Nov 19.443	570.453	LCO	i'	1×180	14.075 ± 0.012
2019 Nov 19.459	570.469	LCO	i'	1×180	14.090 ± 0.009
2019 Nov 19.461	570.471	LCO	i'	1×180	14.091 ± 0.009
2019 Nov 19.463	570.473	LCO	i'	1×180	14.098 ± 0.007
2019 Nov 21.141	572.151	LCO	i'	1×180	14.219 ± 0.008
2019 Nov 21.144	572.154	LCO	i'	1×180	14.177 ± 0.009
2019 Nov 21.146	572.156	LCO	i'	1×180	14.194 ± 0.007
2019 Nov 21.157	572.167	LCO	i'	1×180	14.194 ± 0.008
2019 Nov 21.159	572.169	LCO	i'	1×180	14.223 ± 0.007
2019 Nov 21.161	572.171	LCO	i'	1×180	14.197 ± 0.007
2019 Nov 21.194	572.204	LCO	i'	1×180	14.262 ± 0.007
2019 Nov 21.196	572.206	LCO	i'	1×180	14.267 ± 0.007
2019 Nov 21.199	572.209	LCO	i'	1×180	14.249 ± 0.007
2019 Nov 21.295	572.305	LCO	i'	1×180	14.192 ± 0.006
2019 Nov 21.298	572.308	LCO	i'	1×180	14.185 ± 0.008
2019 Nov 21.300	572.310	LCO	i'	1×180	14.182 ± 0.007
2019 Nov 21.323	572.333	LCO	i'	1×180	14.265 ± 0.006
2019 Nov 21.326	572.336	LCO	i'	1×180	14.280 ± 0.006
2019 Nov 21.328	572.338	LCO	i'	1×180	14.290 ± 0.006
2019 Nov 21.354	572.364	LCO	i'	1×180	14.258 ± 0.006
2019 Nov 21.357	572.367	LCO	i'	1×180	14.125 ± 0.048
2019 Nov 21.359	572.369	LCO	i'	1×180	14.251 ± 0.006
2019 Nov 21.369	572.379	LCO	i'	1×180	14.256 ± 0.008
2019 Nov 21.371	572.381	LCO	i'	1×180	14.281 ± 0.006
2019 Nov 21.373	572.383	LCO	i'	1×180	14.269 ± 0.007
2019 Nov 21.396	572.406	LCO	i'	1×180	14.268 ± 0.007
2019 Nov 21.398	572.408	LCO	i'	1×180	14.271 ± 0.007
2019 Nov 21.401	572.411	LCO	i'	1×180	14.234 ± 0.007
2019 Nov 21.440	572.450	LCO	i'	1×180	14.220 ± 0.006
2019 Nov 21.443	572.453	LCO	i'	1×180	14.214 ± 0.007
2019 Nov 21.445	572.455	LCO	i'	1×180	14.206 ± 0.007
2019 Nov 21.462	572.472	LCO	i'	1×180	14.204 ± 0.007
2019 Nov 21.464	572.474	LCO	i'	1×180	14.192 ± 0.007
2019 Nov 21.467	572.477	LCO	i'	1×180	14.211 ± 0.007
2019 Nov 22.217	573.227	LCO	i'	1×180	14.137 ± 0.007
2019 Nov 22.219	573.229	LCO	i'	1×180	14.136 ± 0.007
2019 Nov 22.222	573.232	LCO	i'	1×180	14.132 ± 0.007
2019 Nov 23.137	574.147	LCO	i'	1×180	14.039 ± 0.007
2019 Nov 23.139	574.149	LCO	i'	1×180	14.034 ± 0.007
2019 Nov 23.141	574.151	LCO	i'	1×180	14.032 ± 0.008
2019 Nov 23.142	574.152	LCO	i'	1×180	14.030 ± 0.007
2019 Nov 23.145	574.155	LCO	i'	1×180	14.043 ± 0.007
2019 Nov 23.147	574.157	LCO	i'	1×180	14.069 ± 0.008
2019 Nov 23.182	574.192	LCO	i'	1×180	14.069 ± 0.006
2019 Nov 23.185	574.195	LCO	i'	1×180	14.038 ± 0.007
2019 Nov 23.187	574.197	LCO	i'	1×180	14.053 ± 0.006
2019 Nov 23.191	574.201	LCO	i'	1×180	14.067 ± 0.007
2019 Nov 23.193	574.203	LCO	i'	1×180	14.070 ± 0.007
2019 Nov 23.196	574.206	LCO	i'	1×180	14.084 ± 0.006
2019 Nov 23.271	574.281	LCO	i'	1×180	14.094 ± 0.006
2019 Nov 23.274	574.284	LCO	i'	1×180	14.114 ± 0.007

Continued on next page

Table A3 – continued from previous page

Date (UT)	Δ t / days	Telescope & Instrument	Filter	Exposure time /s	Photometry /mag
2019 Nov 23.276	574.286	LCO	i'	1×180	14.101 ± 0.006
2019 Nov 23.280	574.290	LCO	i'	1×180	14.047 ± 0.007
2019 Nov 23.282	574.292	LCO	i'	1×180	14.075 ± 0.006
2019 Nov 23.285	574.295	LCO	i'	1×180	14.085 ± 0.007
2019 Nov 23.295	574.305	LCO	i'	1×180	14.062 ± 0.006
2019 Nov 23.298	574.308	LCO	i'	1×180	14.070 ± 0.007
2019 Nov 23.300	574.310	LCO	i'	1×180	14.047 ± 0.007
2019 Nov 23.359	574.369	LCO	i'	1×180	14.021 ± 0.007
2019 Nov 23.361	574.371	LCO	i'	1×180	14.042 ± 0.006
2019 Nov 23.363	574.373	LCO	i'	1×180	14.084 ± 0.007
2019 Nov 23.447	574.457	LCO	i'	1×180	14.137 ± 0.006
2019 Nov 23.449	574.459	LCO	i'	1×180	14.146 ± 0.007
2019 Nov 23.451	574.461	LCO	i'	1×180	14.173 ± 0.007
2019 Nov 23.466	574.476	LCO	i'	1×180	14.116 ± 0.008
2019 Nov 23.468	574.478	LCO	i'	1×180	14.078 ± 0.006
2019 Nov 23.470	574.480	LCO	i'	1×180	14.106 ± 0.008
2019 Nov 23.897	574.907	LT IO:O	i'	1×120	14.356 ± 0.006
2019 Nov 23.899	574.909	LT IO:O	i'	1×120	14.297 ± 0.006
2019 Nov 23.901	574.911	LT IO:O	i'	1×120	14.528 ± 0.006
2019 Nov 23.951	574.961	LT IO:O	i'	1×120	14.257 ± 0.005
2019 Nov 23.953	574.963	LT IO:O	i'	1×120	14.269 ± 0.007
2019 Nov 23.954	574.964	LT IO:O	i'	1×120	14.318 ± 0.005
2019 Nov 24.011	575.021	LT IO:O	i'	1×120	14.503 ± 0.005
2019 Nov 24.013	575.023	LT IO:O	i'	1×120	14.679 ± 0.005
2019 Nov 24.014	575.024	LT IO:O	i'	1×120	14.680 ± 0.006
2019 Nov 24.108	575.118	LT IO:O	i'	1×120	14.350 ± 0.006
2019 Nov 24.110	575.120	LT IO:O	i'	1×120	14.439 ± 0.006
2019 Nov 24.112	575.122	LT IO:O	i'	1×120	14.534 ± 0.006
2019 Nov 24.159	575.169	LT IO:O	i'	1×120	14.297 ± 0.006
2019 Nov 24.160	575.170	LT IO:O	i'	1×120	14.346 ± 0.005
2019 Nov 24.162	575.172	LT IO:O	i'	1×120	14.328 ± 0.006
2019 Nov 24.211	575.221	LT IO:O	i'	1×120	14.435 ± 0.006
2019 Nov 24.213	575.223	LT IO:O	i'	1×120	14.549 ± 0.006
2019 Nov 24.215	575.225	LT IO:O	i'	1×120	14.445 ± 0.006
2019 Nov 24.261	575.271	LT IO:O	i'	1×120	14.380 ± 0.005
2019 Nov 24.262	575.272	LT IO:O	i'	1×120	14.295 ± 0.006
2019 Nov 24.264	575.274	LT IO:O	i'	1×120	14.292 ± 0.006
2019 Nov 24.882	575.892	LT IO:O	i'	1×120	14.130 ± 0.019
2019 Nov 24.884	575.894	LT IO:O	i'	1×120	14.126 ± 0.021
2019 Nov 24.885	575.895	LT IO:O	i'	1×120	14.359 ± 0.163
2019 Nov 25.020	576.030	LT IO:O	i'	1×120	14.125 ± 0.007
2019 Nov 25.021	576.031	LT IO:O	i'	1×120	14.094 ± 0.006
2019 Nov 25.023	576.033	LT IO:O	i'	1×120	14.089 ± 0.007
2019 Nov 25.069	576.079	LT IO:O	i'	1×120	14.044 ± 0.006
2019 Nov 25.071	576.081	LT IO:O	i'	1×120	14.057 ± 0.007
2019 Nov 25.072	576.082	LT IO:O	i'	1×120	14.046 ± 0.006
2019 Nov 25.118	576.128	LT IO:O	i'	1×120	14.146 ± 0.006
2019 Nov 25.120	576.130	LT IO:O	i'	1×120	14.144 ± 0.005
2019 Nov 25.122	576.132	LT IO:O	i'	1×120	14.143 ± 0.005
2019 Nov 25.170	576.180	LT IO:O	i'	1×120	14.275 ± 0.005
2019 Nov 25.172	576.182	LT IO:O	i'	1×120	14.146 ± 0.005
2019 Nov 25.174	576.184	LT IO:O	i'	1×120	14.098 ± 0.005
2019 Nov 25.234	576.244	LT IO:O	i'	1×120	14.051 ± 0.006
2019 Nov 25.236	576.246	LT IO:O	i'	1×120	14.093 ± 0.006
2019 Nov 25.237	576.247	LT IO:O	i'	1×120	14.076 ± 0.006
2019 Nov 25.886	576.896	LT IO:O	i'	1×120	14.093 ± 0.007
2019 Nov 25.888	576.898	LT IO:O	i'	1×120	14.145 ± 0.007
2019 Nov 25.890	576.900	LT IO:O	i'	1×120	14.140 ± 0.006

Table A3 – continued from previous page

Date (UT)	Δ t / days	Telescope & Instrument	Filter	Exposure time /s	Photometry /mag
2019 Nov 25.946	576.956	LT IO:O	i'	1 × 120	14.515 ± 0.005
2019 Nov 25.947	576.957	LT IO:O	i'	1 × 120	14.362 ± 0.005
2019 Nov 25.949	576.959	LT IO:O	i'	1 × 120	14.382 ± 0.005
2019 Nov 25.996	577.006	LT IO:O	i'	1 × 120	14.546 ± 0.005
2019 Nov 25.997	577.007	LT IO:O	i'	1 × 120	14.535 ± 0.006
2019 Nov 25.999	577.009	LT IO:O	i'	1 × 120	14.595 ± 0.006
2019 Nov 26.048	577.058	LT IO:O	i'	1 × 120	14.208 ± 0.006
2019 Nov 26.049	577.059	LT IO:O	i'	1 × 120	14.436 ± 0.006
2019 Nov 26.051	577.061	LT IO:O	i'	1 × 120	14.303 ± 0.006
2019 Nov 26.099	577.109	LT IO:O	i'	1 × 120	14.325 ± 0.006
2019 Nov 26.101	577.111	LT IO:O	i'	1 × 120	14.233 ± 0.006
2019 Nov 26.102	577.112	LT IO:O	i'	1 × 120	14.253 ± 0.005
2019 Nov 26.150	577.160	LT IO:O	i'	1 × 120	14.376 ± 0.006
2019 Nov 26.151	577.161	LT IO:O	i'	1 × 120	14.320 ± 0.006
2019 Nov 26.153	577.163	LT IO:O	i'	1 × 120	14.496 ± 0.006
2019 Nov 26.200	577.210	LT IO:O	i'	1 × 120	14.391 ± 0.006
2019 Nov 26.201	577.211	LT IO:O	i'	1 × 120	14.332 ± 0.006
2019 Nov 26.203	577.213	LT IO:O	i'	1 × 120	14.368 ± 0.005
2019 Nov 26.253	577.263	LT IO:O	i'	1 × 120	14.214 ± 0.006
2019 Nov 26.255	577.265	LT IO:O	i'	1 × 120	14.226 ± 0.006
2019 Nov 26.257	577.267	LT IO:O	i'	1 × 120	14.230 ± 0.006
2019 Nov 26.911	577.921	LT IO:O	i'	1 × 120	14.596 ± 0.006
2019 Nov 26.912	577.922	LT IO:O	i'	1 × 120	14.588 ± 0.006
2019 Nov 26.914	577.924	LT IO:O	i'	1 × 120	14.595 ± 0.005
2019 Nov 26.971	577.981	LT IO:O	i'	1 × 120	14.350 ± 0.005
2019 Nov 26.973	577.983	LT IO:O	i'	1 × 120	14.328 ± 0.005
2019 Nov 26.974	577.984	LT IO:O	i'	1 × 120	14.333 ± 0.005
2019 Nov 27.021	578.031	LT IO:O	i'	1 × 120	14.516 ± 0.007
2019 Nov 27.023	578.033	LT IO:O	i'	1 × 120	14.535 ± 0.006
2019 Nov 27.025	578.035	LT IO:O	i'	1 × 120	14.503 ± 0.006
2019 Nov 27.084	578.094	LT IO:O	i'	1 × 120	14.558 ± 0.005
2019 Nov 27.086	578.096	LT IO:O	i'	1 × 120	14.578 ± 0.005
2019 Nov 27.087	578.097	LT IO:O	i'	1 × 120	14.453 ± 0.005
2019 Nov 27.134	578.144	LT IO:O	i'	1 × 120	14.495 ± 0.005
2019 Nov 27.135	578.145	LT IO:O	i'	1 × 120	14.565 ± 0.005
2019 Nov 27.137	578.147	LT IO:O	i'	1 × 120	14.521 ± 0.005
2019 Nov 27.183	578.193	LT IO:O	i'	1 × 120	14.494 ± 0.005
2019 Nov 27.185	578.195	LT IO:O	i'	1 × 120	14.552 ± 0.005
2019 Nov 27.186	578.196	LT IO:O	i'	1 × 120	14.463 ± 0.005
2019 Nov 27.944	578.954	LT IO:O	i'	1 × 120	14.157 ± 0.014
2019 Nov 27.945	578.955	LT IO:O	i'	1 × 120	14.123 ± 0.014
2019 Nov 27.947	578.957	LT IO:O	i'	1 × 120	14.351 ± 0.039
2019 Nov 27.979	578.989	LT IO:O	i'	1 × 120	14.168 ± 0.006
2019 Nov 27.980	578.990	LT IO:O	i'	1 × 120	14.161 ± 0.012
2019 Nov 27.982	578.992	LT IO:O	i'	1 × 120	14.168 ± 0.007
2019 Nov 28.012	579.022	LT IO:O	i'	1 × 120	14.225 ± 0.007
2019 Nov 28.013	579.023	LT IO:O	i'	1 × 120	14.223 ± 0.007
2019 Nov 28.015	579.025	LT IO:O	i'	1 × 120	14.203 ± 0.009
2019 Nov 28.042	579.052	LT IO:O	i'	1 × 120	14.208 ± 0.006
2019 Nov 28.043	579.053	LT IO:O	i'	1 × 120	14.207 ± 0.005
2019 Nov 28.045	579.055	LT IO:O	i'	1 × 120	14.213 ± 0.006
2019 Nov 28.071	579.081	LT IO:O	i'	1 × 120	14.194 ± 0.006
2019 Nov 28.073	579.083	LT IO:O	i'	1 × 120	14.208 ± 0.006
2019 Nov 28.074	579.084	LT IO:O	i'	1 × 120	14.228 ± 0.005
2019 Nov 28.098	579.108	LT IO:O	i'	1 × 120	14.229 ± 0.005
2019 Nov 28.099	579.109	LT IO:O	i'	1 × 120	14.182 ± 0.005
2019 Nov 28.101	579.111	LT IO:O	i'	1 × 120	14.195 ± 0.006
2019 Nov 28.914	579.924	LT IO:O	i'	1 × 120	14.199 ± 0.006

Table A3 – continued from previous page

Date (UT)	Δ t / days	Telescope & Instrument	Filter	Exposure time /s	Photometry /mag
2019 Nov 28.916	579.926	LT IO:O	i'	1×120	14.196 ± 0.006
2019 Nov 28.917	579.927	LT IO:O	i'	1×120	14.507 ± 0.005
2019 Nov 28.951	579.961	LT IO:O	i'	1×120	14.266 ± 0.005
2019 Nov 28.953	579.963	LT IO:O	i'	1×120	14.280 ± 0.005
2019 Nov 28.954	579.964	LT IO:O	i'	1×120	14.245 ± 0.005
2019 Nov 28.993	580.003	LT IO:O	i'	1×120	14.194 ± 0.006
2019 Nov 28.994	580.004	LT IO:O	i'	1×120	14.171 ± 0.006
2019 Nov 28.996	580.006	LT IO:O	i'	1×120	14.153 ± 0.007
2019 Nov 29.022	580.032	LT IO:O	i'	1×120	14.165 ± 0.007
2019 Nov 29.024	580.034	LT IO:O	i'	1×120	14.172 ± 0.007
2019 Nov 29.026	580.036	LT IO:O	i'	1×120	14.172 ± 0.006
2019 Nov 29.052	580.062	LT IO:O	i'	1×120	14.201 ± 0.005
2019 Nov 29.054	580.064	LT IO:O	i'	1×120	14.206 ± 0.006
2019 Nov 29.056	580.066	LT IO:O	i'	1×120	14.214 ± 0.005
2019 Nov 29.082	580.092	LT IO:O	i'	1×120	14.203 ± 0.006
2019 Nov 29.083	580.093	LT IO:O	i'	1×120	14.196 ± 0.006
2019 Nov 29.085	580.095	LT IO:O	i'	1×120	14.198 ± 0.006
2019 Nov 29.938	580.948	LT IO:O	i'	1×120	14.225 ± 0.005
2019 Nov 29.939	580.949	LT IO:O	i'	1×120	14.203 ± 0.006
2019 Nov 29.941	580.951	LT IO:O	i'	1×120	14.216 ± 0.006
2019 Nov 29.943	580.953	LT IO:O	i'	1×120	14.225 ± 0.006
2019 Nov 29.944	580.954	LT IO:O	i'	1×120	14.243 ± 0.006
2019 Nov 29.946	580.956	LT IO:O	i'	1×120	14.252 ± 0.006
2019 Nov 29.947	580.957	LT IO:O	i'	1×120	14.244 ± 0.006
2019 Nov 29.949	580.959	LT IO:O	i'	1×120	14.255 ± 0.006
2019 Nov 29.951	580.961	LT IO:O	i'	1×120	14.265 ± 0.005
2019 Nov 29.952	580.962	LT IO:O	i'	1×120	14.255 ± 0.006
2019 Nov 29.954	580.964	LT IO:O	i'	1×120	14.255 ± 0.005
2019 Nov 29.956	580.966	LT IO:O	i'	1×120	14.259 ± 0.006
2019 Nov 29.957	580.967	LT IO:O	i'	1×120	14.252 ± 0.006
2019 Nov 29.959	580.969	LT IO:O	i'	1×120	14.258 ± 0.006
2019 Nov 29.960	580.970	LT IO:O	i'	1×120	14.238 ± 0.006
2019 Nov 29.962	580.972	LT IO:O	i'	1×120	14.234 ± 0.006
2019 Nov 29.964	580.974	LT IO:O	i'	1×120	14.198 ± 0.006
2019 Nov 29.965	580.975	LT IO:O	i'	1×120	14.190 ± 0.006
2019 Nov 29.967	580.977	LT IO:O	i'	1×120	14.183 ± 0.006
2019 Nov 29.968	580.978	LT IO:O	i'	1×120	14.171 ± 0.006
2019 Nov 30.009	581.019	LT IO:O	i'	1×120	14.190 ± 0.007
2019 Nov 30.011	581.021	LT IO:O	i'	1×120	14.208 ± 0.006
2019 Nov 30.013	581.023	LT IO:O	i'	1×120	14.207 ± 0.007
2019 Nov 30.014	581.024	LT IO:O	i'	1×120	14.205 ± 0.006
2019 Nov 30.016	581.026	LT IO:O	i'	1×120	14.210 ± 0.007
2019 Nov 30.017	581.027	LT IO:O	i'	1×120	14.205 ± 0.006
2019 Nov 30.019	581.029	LT IO:O	i'	1×120	14.201 ± 0.007
2019 Nov 30.021	581.031	LT IO:O	i'	1×120	14.207 ± 0.006
2019 Nov 30.022	581.032	LT IO:O	i'	1×120	14.196 ± 0.006
2019 Nov 30.024	581.034	LT IO:O	i'	1×120	14.204 ± 0.006
2019 Nov 30.026	581.036	LT IO:O	i'	1×120	14.195 ± 0.006
2019 Nov 30.027	581.037	LT IO:O	i'	1×120	14.179 ± 0.006
2019 Nov 30.029	581.039	LT IO:O	i'	1×120	14.191 ± 0.006
2019 Nov 30.030	581.040	LT IO:O	i'	1×120	14.214 ± 0.006
2019 Nov 30.032	581.042	LT IO:O	i'	1×120	14.244 ± 0.006
2019 Nov 30.034	581.044	LT IO:O	i'	1×120	14.227 ± 0.005
2019 Nov 30.035	581.045	LT IO:O	i'	1×120	14.237 ± 0.006
2019 Nov 30.037	581.047	LT IO:O	i'	1×120	14.249 ± 0.006
2019 Nov 30.038	581.048	LT IO:O	i'	1×120	14.284 ± 0.005
2019 Nov 30.040	581.050	LT IO:O	i'	1×120	14.296 ± 0.005
2019 Nov 30.076	581.086	LT IO:O	i'	1×120	14.334 ± 0.006

Table A3 – continued from previous page

Date (UT)	Δ t / days	Telescope & Instrument	Filter	Exposure time /s	Photometry /mag
2019 Nov 30.077	581.087	LT IO:O	i'	1 × 120	14.391 ± 0.005
2019 Nov 30.079	581.089	LT IO:O	i'	1 × 120	14.288 ± 0.006
2019 Nov 30.080	581.090	LT IO:O	i'	1 × 120	14.310 ± 0.006
2019 Nov 30.082	581.092	LT IO:O	i'	1 × 120	14.388 ± 0.005
2019 Nov 30.084	581.094	LT IO:O	i'	1 × 120	14.388 ± 0.005
2019 Nov 30.085	581.095	LT IO:O	i'	1 × 120	14.377 ± 0.005
2019 Nov 30.087	581.097	LT IO:O	i'	1 × 120	14.355 ± 0.005
2019 Nov 30.088	581.098	LT IO:O	i'	1 × 120	14.393 ± 0.006
2019 Nov 30.090	581.100	LT IO:O	i'	1 × 120	14.432 ± 0.006
2019 Nov 30.092	581.102	LT IO:O	i'	1 × 120	14.495 ± 0.006
2019 Nov 30.093	581.103	LT IO:O	i'	1 × 120	14.556 ± 0.006
2019 Nov 30.095	581.105	LT IO:O	i'	1 × 120	14.411 ± 0.005
2019 Nov 30.096	581.106	LT IO:O	i'	1 × 120	14.349 ± 0.005
2019 Nov 30.098	581.108	LT IO:O	i'	1 × 120	14.372 ± 0.005
2019 Nov 30.100	581.110	LT IO:O	i'	1 × 120	14.607 ± 0.006
2019 Nov 30.101	581.111	LT IO:O	i'	1 × 120	14.531 ± 0.006
2019 Nov 30.103	581.113	LT IO:O	i'	1 × 120	14.445 ± 0.005
2019 Nov 30.104	581.114	LT IO:O	i'	1 × 120	14.345 ± 0.005
2019 Nov 30.106	581.116	LT IO:O	i'	1 × 120	14.311 ± 0.005
2019 Nov 30.132	581.142	LT IO:O	i'	1 × 120	14.345 ± 0.005
2019 Nov 30.133	581.143	LT IO:O	i'	1 × 120	14.501 ± 0.005
2019 Nov 30.135	581.145	LT IO:O	i'	1 × 120	14.425 ± 0.006
2019 Nov 30.137	581.147	LT IO:O	i'	1 × 120	14.507 ± 0.005
2019 Nov 30.138	581.148	LT IO:O	i'	1 × 120	14.515 ± 0.005
2019 Nov 30.140	581.150	LT IO:O	i'	1 × 120	14.360 ± 0.006
2019 Nov 30.142	581.152	LT IO:O	i'	1 × 120	14.508 ± 0.006
2019 Nov 30.143	581.153	LT IO:O	i'	1 × 120	14.397 ± 0.005
2019 Nov 30.145	581.155	LT IO:O	i'	1 × 120	14.500 ± 0.006
2019 Nov 30.146	581.156	LT IO:O	i'	1 × 120	14.496 ± 0.006
2019 Nov 30.148	581.158	LT IO:O	i'	1 × 120	14.516 ± 0.006
2019 Nov 30.150	581.160	LT IO:O	i'	1 × 120	14.527 ± 0.005
2019 Nov 30.151	581.161	LT IO:O	i'	1 × 120	14.550 ± 0.005
2019 Nov 30.153	581.163	LT IO:O	i'	1 × 120	14.602 ± 0.005
2019 Nov 30.154	581.164	LT IO:O	i'	1 × 120	14.547 ± 0.005
2019 Nov 30.156	581.166	LT IO:O	i'	1 × 120	14.591 ± 0.006
2019 Nov 30.158	581.168	LT IO:O	i'	1 × 120	14.525 ± 0.006
2019 Nov 30.159	581.169	LT IO:O	i'	1 × 120	14.598 ± 0.006
2019 Nov 30.161	581.171	LT IO:O	i'	1 × 120	14.706 ± 0.006
2019 Nov 30.162	581.172	LT IO:O	i'	1 × 120	14.574 ± 0.005
2019 Dec 01.941	582.951	LT IO:O	i'	1 × 120	14.441 ± 0.006
2019 Dec 01.943	582.953	LT IO:O	i'	1 × 120	14.527 ± 0.005
2019 Dec 01.945	582.955	LT IO:O	i'	1 × 120	14.520 ± 0.006
2019 Dec 01.946	582.956	LT IO:O	i'	1 × 120	14.574 ± 0.006
2019 Dec 01.948	582.958	LT IO:O	i'	1 × 120	14.609 ± 0.005
2019 Dec 01.950	582.960	LT IO:O	i'	1 × 120	14.595 ± 0.006
2019 Dec 01.951	582.961	LT IO:O	i'	1 × 120	14.657 ± 0.006
2019 Dec 01.953	582.963	LT IO:O	i'	1 × 120	14.792 ± 0.005
2019 Dec 01.954	582.964	LT IO:O	i'	1 × 120	14.666 ± 0.006
2019 Dec 01.956	582.966	LT IO:O	i'	1 × 120	14.542 ± 0.005
2019 Dec 01.958	582.968	LT IO:O	i'	1 × 120	14.602 ± 0.005
2019 Dec 01.959	582.969	LT IO:O	i'	1 × 120	14.535 ± 0.006
2019 Dec 01.961	582.971	LT IO:O	i'	1 × 120	14.573 ± 0.006
2019 Dec 01.962	582.972	LT IO:O	i'	1 × 120	14.583 ± 0.005
2019 Dec 01.964	582.974	LT IO:O	i'	1 × 120	14.546 ± 0.006
2019 Dec 01.966	582.976	LT IO:O	i'	1 × 120	14.588 ± 0.006
2019 Dec 01.967	582.977	LT IO:O	i'	1 × 120	14.595 ± 0.006
2019 Dec 01.969	582.979	LT IO:O	i'	1 × 120	14.504 ± 0.005
2019 Dec 01.970	582.980	LT IO:O	i'	1 × 120	14.642 ± 0.006

Table A3 – continued from previous page

Date (UT)	Δ t / days	Telescope & Instrument	Filter	Exposure time /s	Photometry /mag
2019 Dec 01.972	582.982	LT IO:O	i'	1 × 120	14.479 ± 0.006
2019 Dec 01.999	583.010	LT IO:O	i'	1 × 120	14.446 ± 0.006
2019 Dec 02.001	583.011	LT IO:O	i'	1 × 120	14.591 ± 0.006
2019 Dec 02.003	583.013	LT IO:O	i'	1 × 120	14.509 ± 0.006
2019 Dec 02.005	583.015	LT IO:O	i'	1 × 120	14.625 ± 0.006
2019 Dec 02.006	583.016	LT IO:O	i'	1 × 120	14.551 ± 0.006
2019 Dec 02.008	583.018	LT IO:O	i'	1 × 120	14.643 ± 0.006
2019 Dec 02.009	583.019	LT IO:O	i'	1 × 120	14.530 ± 0.006
2019 Dec 02.011	583.021	LT IO:O	i'	1 × 120	14.622 ± 0.006
2019 Dec 02.013	583.023	LT IO:O	i'	1 × 120	14.474 ± 0.005
2019 Dec 02.014	583.024	LT IO:O	i'	1 × 120	14.640 ± 0.006
2019 Dec 02.016	583.026	LT IO:O	i'	1 × 120	14.585 ± 0.006
2019 Dec 02.017	583.027	LT IO:O	i'	1 × 120	14.560 ± 0.006
2019 Dec 02.019	583.029	LT IO:O	i'	1 × 120	14.568 ± 0.006
2019 Dec 02.021	583.031	LT IO:O	i'	1 × 120	14.613 ± 0.006
2019 Dec 02.022	583.032	LT IO:O	i'	1 × 120	14.609 ± 0.006
2019 Dec 02.024	583.034	LT IO:O	i'	1 × 120	14.591 ± 0.006
2019 Dec 02.025	583.035	LT IO:O	i'	1 × 120	14.456 ± 0.006
2019 Dec 02.027	583.037	LT IO:O	i'	1 × 120	14.734 ± 0.006
2019 Dec 02.029	583.039	LT IO:O	i'	1 × 120	14.539 ± 0.006
2019 Dec 02.030	583.040	LT IO:O	i'	1 × 120	14.569 ± 0.006
2019 Dec 02.058	583.068	LT IO:O	i'	1 × 120	14.496 ± 0.006
2019 Dec 02.060	583.070	LT IO:O	i'	1 × 120	14.444 ± 0.006
2019 Dec 02.061	583.071	LT IO:O	i'	1 × 120	14.532 ± 0.006
2019 Dec 02.063	583.073	LT IO:O	i'	1 × 120	14.552 ± 0.005
2019 Dec 02.064	583.074	LT IO:O	i'	1 × 120	14.502 ± 0.005
2019 Dec 02.066	583.076	LT IO:O	i'	1 × 120	14.525 ± 0.005
2019 Dec 02.068	583.078	LT IO:O	i'	1 × 120	14.529 ± 0.005
2019 Dec 02.069	583.079	LT IO:O	i'	1 × 120	14.552 ± 0.005
2019 Dec 02.071	583.081	LT IO:O	i'	1 × 120	14.436 ± 0.005
2019 Dec 02.073	583.083	LT IO:O	i'	1 × 120	14.521 ± 0.005
2019 Dec 02.074	583.084	LT IO:O	i'	1 × 120	14.596 ± 0.005
2019 Dec 02.076	583.086	LT IO:O	i'	1 × 120	14.558 ± 0.006
2019 Dec 02.077	583.087	LT IO:O	i'	1 × 120	14.381 ± 0.005
2019 Dec 02.079	583.089	LT IO:O	i'	1 × 120	14.592 ± 0.006
2019 Dec 02.081	583.091	LT IO:O	i'	1 × 120	14.585 ± 0.006
2019 Dec 02.082	583.092	LT IO:O	i'	1 × 120	14.542 ± 0.005
2019 Dec 02.084	583.094	LT IO:O	i'	1 × 120	14.414 ± 0.006
2019 Dec 02.085	583.095	LT IO:O	i'	1 × 120	14.520 ± 0.006
2019 Dec 02.087	583.097	LT IO:O	i'	1 × 120	14.429 ± 0.006
2019 Dec 02.089	583.099	LT IO:O	i'	1 × 120	14.373 ± 0.005
2019 Dec 02.114	583.124	LT IO:O	i'	1 × 120	14.517 ± 0.006
2019 Dec 02.116	583.126	LT IO:O	i'	1 × 120	14.504 ± 0.006
2019 Dec 02.117	583.127	LT IO:O	i'	1 × 120	14.576 ± 0.006
2019 Dec 02.119	583.129	LT IO:O	i'	1 × 120	14.467 ± 0.007
2019 Dec 02.121	583.131	LT IO:O	i'	1 × 120	14.589 ± 0.006
2019 Dec 02.122	583.132	LT IO:O	i'	1 × 120	14.586 ± 0.006
2019 Dec 02.124	583.134	LT IO:O	i'	1 × 120	14.470 ± 0.005
2019 Dec 02.125	583.135	LT IO:O	i'	1 × 120	14.539 ± 0.005
2019 Dec 02.127	583.137	LT IO:O	i'	1 × 120	14.516 ± 0.006
2019 Dec 02.129	583.139	LT IO:O	i'	1 × 120	14.686 ± 0.007
2019 Dec 02.130	583.140	LT IO:O	i'	1 × 120	14.601 ± 0.006
2019 Dec 02.132	583.142	LT IO:O	i'	1 × 120	14.628 ± 0.006
2019 Dec 02.133	583.143	LT IO:O	i'	1 × 120	14.530 ± 0.006
2019 Dec 02.135	583.145	LT IO:O	i'	1 × 120	14.669 ± 0.006
2019 Dec 02.137	583.147	LT IO:O	i'	1 × 120	14.736 ± 0.005
2019 Dec 02.138	583.148	LT IO:O	i'	1 × 120	14.667 ± 0.006
2019 Dec 02.140	583.150	LT IO:O	i'	1 × 120	14.671 ± 0.006

Continued on next page

Table A3 – continued from previous page

Date (UT)	Δ t / days	Telescope & Instrument	Filter	Exposure time /s	Photometry /mag
2019 Dec 02.142	583.152	LT IO:O	i'	1×120	14.625 ± 0.006
2019 Dec 02.143	583.153	LT IO:O	i'	1×120	14.666 ± 0.006
2019 Dec 02.145	583.155	LT IO:O	i'	1×120	14.582 ± 0.005
2019 Dec 02.196	583.206	LT IO:O	i'	1×120	14.439 ± 0.005
2019 Dec 02.197	583.207	LT IO:O	i'	1×120	14.531 ± 0.005
2019 Dec 02.199	583.209	LT IO:O	i'	1×120	14.446 ± 0.006
2019 Dec 02.201	583.211	LT IO:O	i'	1×120	14.527 ± 0.005
2019 Dec 02.202	583.212	LT IO:O	i'	1×120	14.425 ± 0.006
2019 Dec 02.204	583.214	LT IO:O	i'	1×120	14.128 ± 0.008
2019 Dec 02.205	583.215	LT IO:O	i'	1×120	14.126 ± 0.010
2019 Dec 02.207	583.217	LT IO:O	i'	1×120	14.156 ± 0.010
2019 Dec 02.209	583.219	LT IO:O	i'	1×120	14.106 ± 0.010
2019 Dec 02.210	583.220	LT IO:O	i'	1×120	14.091 ± 0.008
2019 Dec 02.212	583.222	LT IO:O	i'	1×120	14.141 ± 0.011
2019 Dec 02.214	583.224	LT IO:O	i'	1×120	14.173 ± 0.009
2019 Dec 02.215	583.225	LT IO:O	i'	1×120	14.152 ± 0.011
2019 Dec 02.217	583.227	LT IO:O	i'	1×120	14.160 ± 0.009
2019 Dec 02.218	583.228	LT IO:O	i'	1×120	14.170 ± 0.010
2019 Dec 02.220	583.230	LT IO:O	i'	1×120	14.209 ± 0.011
2019 Dec 02.222	583.232	LT IO:O	i'	1×120	14.175 ± 0.010
2019 Dec 02.223	583.233	LT IO:O	i'	1×120	14.198 ± 0.010
2019 Dec 02.225	583.235	LT IO:O	i'	1×120	14.187 ± 0.010
2019 Dec 02.226	583.236	LT IO:O	i'	1×120	14.179 ± 0.011
2019 Dec 09.911	590.921	LT IO:O	i'	1×60	14.338 ± 0.007
2019 Dec 09.912	590.922	LT IO:O	i'	1×60	14.331 ± 0.007
2019 Dec 09.913	590.923	LT IO:O	i'	1×60	14.322 ± 0.005
2020 Aug 31.177	856.187	LT IO:O	i'	3×120	14.509 ± 0.006
2021 Feb 02.879	1011.889	LT IO:O	i'	3×180	14.329 ± 0.006
2018 Jul 21.198	84.208	LT IO:O	z'	3×30	13.075 ± 0.008
2018 Jul 22.222	85.232	LT IO:O	z'	3×30	13.087 ± 0.008
2018 Jul 23.199	86.209	LT IO:O	z'	3×30	13.097 ± 0.007
2018 Jul 24.191	87.201	LT IO:O	z'	3×30	13.121 ± 0.006
2018 Jul 25.187	88.197	LT IO:O	z'	3×30	13.224 ± 0.006
2018 Jul 26.196	89.206	LT IO:O	z'	3×30	13.200 ± 0.010
2018 Jul 27.187	90.197	LT IO:O	z'	3×30	13.136 ± 0.011
2018 Jul 28.181	91.191	LT IO:O	z'	3×30	13.283 ± 0.007
2018 Jul 29.180	92.190	LT IO:O	z'	3×30	13.300 ± 0.010
2018 Jul 31.174	94.184	LT IO:O	z'	3×30	13.317 ± 0.007
2018 Aug 01.188	95.198	LT IO:O	z'	3×30	13.338 ± 0.009
2018 Aug 02.164	96.174	LT IO:O	z'	3×30	13.253 ± 0.007
2018 Aug 03.163	97.173	LT IO:O	z'	3×30	13.406 ± 0.007
2018 Aug 06.154	100.164	LT IO:O	z'	3×30	13.410 ± 0.009
2018 Aug 08.170	102.180	LT IO:O	z'	3×30	13.449 ± 0.007
2018 Aug 10.176	104.186	LT IO:O	z'	3×30	13.467 ± 0.006
2018 Aug 13.178	107.188	LT IO:O	z'	3×30	13.563 ± 0.014
2018 Aug 16.128	110.138	LT IO:O	z'	3×30	13.510 ± 0.007
2018 Aug 19.171	113.181	LT IO:O	z'	3×30	13.482 ± 0.008
2018 Aug 22.223	116.233	LT IO:O	z'	3×30	13.424 ± 0.007
2018 Aug 25.103	119.113	LT IO:O	z'	3×30	13.537 ± 0.006
2018 Aug 28.113	122.123	LT IO:O	z'	3×30	13.460 ± 0.008
2018 Aug 31.090	125.100	LT IO:O	z'	3×30	13.495 ± 0.007
2018 Sep 03.079	128.089	LT IO:O	z'	3×30	13.534 ± 0.007
2018 Sep 06.071	131.081	LT IO:O	z'	3×30	13.574 ± 0.008
2018 Sep 09.060	134.070	LT IO:O	z'	3×30	13.677 ± 0.007
2018 Sep 12.068	137.078	LT IO:O	z'	3×30	13.701 ± 0.008
2018 Sep 18.091	143.101	LT IO:O	z'	3×30	13.720 ± 0.006
2018 Sep 23.023	148.033	LT IO:O	z'	3×30	13.742 ± 0.012
2018 Sep 26.019	151.029	LT IO:O	z'	3×30	13.785 ± 0.008

Table A3 – continued from previous page

Date (UT)	Δ t / days	Telescope & Instrument	Filter	Exposure time /s	Photometry /mag
2018 Sep 29.062	154.072	LT IO:O	z'	3×30	13.786 ± 0.007
2018 Oct 02.018	157.028	LT IO:O	z'	3×30	13.874 ± 0.006
2018 Nov 01.117	187.126	LT IO:O	z'	3×30	14.032 ± 0.007
2018 Nov 08.165	194.175	LT IO:O	z'	3×30	14.009 ± 0.007
2018 Nov 16.123	202.133	LT IO:O	z'	3×30	14.015 ± 0.007
2018 Nov 26.029	212.039	LT IO:O	z'	3×30	13.965 ± 0.007
2018 Dec 10.070	226.080	LT IO:O	z'	3×30	14.004 ± 0.007
2018 Dec 15.969	231.979	LT IO:O	z'	3×30	14.009 ± 0.008
2018 Dec 22.845	238.855	LT IO:O	z'	3×30	14.108 ± 0.011
2018 Dec 28.899	244.909	LT IO:O	z'	3×30	14.123 ± 0.010
2019 Jan 04.925	251.935	LT IO:O	z'	3×30	14.106 ± 0.006
2019 Jan 10.978	257.988	LT IO:O	z'	3×30	14.107 ± 0.007
2019 Jan 19.993	267.003	LT IO:O	z'	3×30	14.015 ± 0.007
2019 Jan 25.908	272.918	LT IO:O	z'	3×30	14.000 ± 0.006
2019 Jan 31.944	278.954	LT IO:O	z'	3×30	13.812 ± 0.007
2019 Feb 06.894	284.904	LT IO:O	z'	3×30	14.043 ± 0.009
2019 Feb 12.880	290.890	LT IO:O	z'	3×30	14.095 ± 0.007
2019 Feb 19.904	297.914	LT IO:O	z'	3×30	14.138 ± 0.013
2019 Feb 28.894	306.904	LT IO:O	z'	3×30	14.127 ± 0.006
2019 Mar 16.852	322.862	LT IO:O	z'	3×30	14.073 ± 0.007
2019 Apr 08.864	345.874	LT IO:O	z'	3×30	14.111 ± 0.007
2019 Apr 25.857	362.867	LT IO:O	z'	3×30	14.117 ± 0.008
2019 Jul 19.220	447.230	LT IO:O	z'	3×30	14.038 ± 0.007
2019 Aug 01.224	460.234	LT IO:O	z'	3×30	14.043 ± 0.006
2019 Aug 19.131	478.141	LT IO:O	z'	3×30	14.014 ± 0.007
2019 Sep 14.122	504.132	LT IO:O	z'	3×60	14.163 ± 0.013
2019 Oct 14.986	534.996	LT IO:O	z'	3×60	13.959 ± 0.008
2019 Nov 16.946	567.956	LT IO:O	z'	3×60	13.783 ± 0.007
2019 Dec 09.914	590.924	LT IO:O	z'	3×60	13.991 ± 0.007
2020 Aug 31.182	856.192	LT IO:O	z'	3×120	14.165 ± 0.006
2021 Feb 02.907	1011.917	LT IO:O	z'	3×180	14.053 ± 0.006
2018 Jul 20.155	83.165	Swift UVOT	uvw1	252	16.708 ± 0.056
2018 Jul 26.804	89.814	Swift UVOT	uvw1	325	16.812 ± 0.054
2018 Jul 27.170	90.180	Swift UVOT	uvw1	523	16.934 ± 0.052
2018 Jul 27.934	90.944	Swift UVOT	uvw1	325	17.062 ± 0.056
2018 Aug 03.207	97.217	Swift UVOT	uvw1	632	17.257 ± 0.053
2018 Aug 18.651	112.661	Swift UVOT	uvw1	382	17.476 ± 0.058
2018 Aug 19.773	113.783	Swift UVOT	uvw1	195	17.522 ± 0.067
2018 Aug 24.335	118.345	Swift UVOT	uvw1	581	17.531 ± 0.055
2018 Aug 31.436	125.446	Swift UVOT	uvw1	669	17.609 ± 0.054
2018 Sep 08.004	133.014	Swift UVOT	uvw1	480	17.878 ± 0.060
2018 Sep 14.052	139.062	Swift UVOT	uvw1	591	17.937 ± 0.058
2018 Sep 21.091	146.101	Swift UVOT	uvw1	595	18.053 ± 0.059
2018 Sep 28.297	153.307	Swift UVOT	uvw1	862	17.996 ± 0.055
2018 Oct 12.743	167.753	Swift UVOT	uvw1	702	18.242 ± 0.059
2018 Oct 26.618	181.628	Swift UVOT	uvw1	686	18.262 ± 0.060
2018 Nov 09.801	195.811	Swift UVOT	uvw1	360	18.399 ± 0.063
2018 Nov 23.120	209.130	Swift UVOT	uvw1	701	18.365 ± 0.060
2018 Dec 07.587	223.597	Swift UVOT	uvw1	256	18.417 ± 0.080
2018 Dec 11.436	227.446	Swift UVOT	uvw1	428	18.440 ± 0.069
2018 Dec 21.095	237.105	Swift UVOT	uvw1	852	18.280 ± 0.057
2019 Jan 04.516	251.526	Swift UVOT	uvw1	502	18.529 ± 0.068
2019 Jan 18.095	265.105	Swift UVOT	uvw1	607	18.261 ± 0.061
2019 Feb 02.431	280.441	Swift UVOT	uvw1	644	18.620 ± 0.065
2019 Feb 07.473	285.483	Swift UVOT	uvw1	622	18.373 ± 0.062
2019 Feb 15.350	293.360	Swift UVOT	uvw1	374	18.654 ± 0.076
2019 Feb 21.187	299.197	Swift UVOT	uvw1	89	18.422 ± 0.121
2019 Mar 07.635	313.645	Swift UVOT	uvw1	607	18.412 ± 0.063

Continued on next page

Table A3 – continued from previous page

Date (UT)	Δ t / days	Telescope & Instrument	Filter	Exposure time /s	Photometry /mag
2019 Mar 21.045	327.055	Swift UVOT	uvw1	473	18.202 ± 0.064
2019 Apr 04.198	341.208	Swift UVOT	uvw1	757	18.607 ± 0.063
2019 Apr 18.782	355.792	Swift UVOT	uvw1	689	18.396 ± 0.061
2019 Apr 24.657	361.667	Swift UVOT	uvw1	740	18.512 ± 0.062
2019 Jul 21.133	449.143	Swift UVOT	uvw1	354	18.371 ± 0.073
2019 Aug 18.757	477.767	Swift UVOT	uvw1	581	18.285 ± 0.063
2019 Sep 16.768	506.778	Swift UVOT	uvw1	625	18.439 ± 0.064
2019 Oct 14.722	534.732	Swift UVOT	uvw1	283	18.470 ± 0.079
2019 Nov 14.446	565.456	Swift UVOT	uvw1	592	18.214 ± 0.061
2019 Dec 09.235	590.245	Swift UVOT	uvw1	510	18.158 ± 0.062
2020 Jan 12.730	624.740	Swift UVOT	uvw1	319	18.267 ± 0.072
2020 Feb 12.130	655.140	Swift UVOT	uvw1	288	18.451 ± 0.079
2020 Mar 12.123	684.133	Swift UVOT	uvw1	317	18.258 ± 0.072
2020 Apr 12.358	715.368	Swift UVOT	uvw1	292	18.053 ± 0.070
2020 Aug 24.436	849.446	Swift UVOT	uvw1	331	18.405 ± 0.074
2018 Jul 20.152	83.162	Swift UVOT	uvm2	252	18.676 ± 0.102
2018 Jul 27.167	90.177	Swift UVOT	uvm2	609	18.820 ± 0.079
2018 Jul 27.918	90.928	Swift UVOT	uvm2	323	19.037 ± 0.105
2018 Aug 03.207	97.217	Swift UVOT	uvm2	616	19.276 ± 0.091
2018 Aug 18.649	112.659	Swift UVOT	uvm2	377	19.229 ± 0.107
2018 Aug 19.771	113.781	Swift UVOT	uvm2	156	19.383 ± 0.166
2018 Aug 24.331	118.341	Swift UVOT	uvm2	657	19.365 ± 0.091
2018 Aug 31.432	125.442	Swift UVOT	uvm2	644	19.338 ± 0.091
2018 Sep 08.003	133.013	Swift UVOT	uvm2	538	19.729 ± 0.113
2018 Sep 14.048	139.058	Swift UVOT	uvm2	551	19.664 ± 0.110
2018 Sep 21.087	146.097	Swift UVOT	uvm2	648	19.947 ± 0.115
2018 Sep 28.294	153.304	Swift UVOT	uvm2	868	19.999 ± 0.105
2018 Oct 12.739	167.749	Swift UVOT	uvm2	618	20.045 ± 0.121
2018 Oct 26.614	181.624	Swift UVOT	uvm2	627	20.170 ± 0.127
2018 Nov 09.798	195.808	Swift UVOT	uvm2	341	20.184 ± 0.127
2018 Nov 23.116	209.126	Swift UVOT	uvm2	625	20.082 ± 0.122
2018 Dec 07.586	223.596	Swift UVOT	uvm2	238	20.218 ± 0.201
2018 Dec 11.434	227.444	Swift UVOT	uvm2	278	19.961 ± 0.166
2018 Dec 21.092	237.102	Swift UVOT	uvm2	733	20.102 ± 0.116
2019 Jan 04.514	251.524	Swift UVOT	uvm2	466	20.452 ± 0.165
2019 Jan 18.092	265.102	Swift UVOT	uvm2	642	20.045 ± 0.120
2019 Feb 02.429	280.439	Swift UVOT	uvm2	691	20.616 ± 0.150
2019 Feb 07.472	285.482	Swift UVOT	uvm2	647	20.245 ± 0.130
2019 Feb 15.346	293.356	Swift UVOT	uvm2	378	20.214 ± 0.163
2019 Feb 21.186	299.196	Swift UVOT	uvm2	108	20.082 ± 0.277
2019 Mar 07.632	313.642	Swift UVOT	uvm2	613	20.468 ± 0.151
2019 Mar 21.042	327.052	Swift UVOT	uvm2	434	20.320 ± 0.163
2019 Apr 04.194	341.204	Swift UVOT	uvm2	761	20.402 ± 0.132
2019 Apr 18.780	355.790	Swift UVOT	uvm2	533	20.287 ± 0.146
2019 Apr 24.654	361.664	Swift UVOT	uvm2	615	20.145 ± 0.129
2019 Jul 21.263	449.273	Swift UVOT	uvm2	474	20.247 ± 0.154
2019 Aug 18.755	477.765	Swift UVOT	uvm2	548	19.987 ± 0.128
2019 Sep 16.765	506.775	Swift UVOT	uvm2	465	20.229 ± 0.138
2019 Oct 14.749	534.759	Swift UVOT	uvm2	451	20.462 ± 0.174
2019 Nov 14.442	565.452	Swift UVOT	uvm2	567	19.904 ± 0.118
2019 Dec 09.229	590.239	Swift UVOT	uvm2	475	19.845 ± 0.125
2020 Jan 12.728	624.738	Swift UVOT	uvm2	319	19.911 ± 0.152
2020 Feb 12.128	655.138	Swift UVOT	uvm2	288	20.067 ± 0.173
2020 Mar 12.121	684.131	Swift UVOT	uvm2	317	20.293 ± 0.186
2020 Apr 12.356	715.366	Swift UVOT	uvm2	292	19.751 ± 0.150
2020 Aug 24.434	849.444	Swift UVOT	uvm2	331	20.176 ± 0.170
2018 Jul 20.146	83.156	Swift UVOT	uvw2	252	17.863 ± 0.079
2018 Jul 26.787	89.797	Swift UVOT	uvw2	572	18.063 ± 0.072

Table A3 – continued from previous page

Date (UT)	Δ t / days	Telescope & Instrument	Filter	Exposure time /s	Photometry /mag
2018 Jul 27.164	90.174	Swift UVOT	uvw2	609	18.239 ± 0.073
2018 Aug 03.204	97.214	Swift UVOT	uvw2	616	18.484 ± 0.075
2018 Aug 10.606	104.616	Swift UVOT	uvw2	48	18.802 ± 0.189
2018 Aug 18.617	112.627	Swift UVOT	uvw2	581	18.679 ± 0.078
2018 Aug 19.769	113.779	Swift UVOT	uvw2	159	18.948 ± 0.121
2018 Aug 24.327	118.337	Swift UVOT	uvw2	657	18.736 ± 0.077
2018 Aug 31.428	125.438	Swift UVOT	uvw2	644	18.825 ± 0.079
2018 Sep 08.002	133.012	Swift UVOT	uvw2	538	19.085 ± 0.087
2018 Sep 14.045	139.055	Swift UVOT	uvw2	551	19.118 ± 0.087
2018 Sep 21.084	146.094	Swift UVOT	uvw2	648	19.165 ± 0.084
2018 Sep 28.291	153.301	Swift UVOT	uvw2	868	19.232 ± 0.080
2018 Oct 12.735	167.745	Swift UVOT	uvw2	616	19.323 ± 0.088
2018 Oct 26.610	181.620	Swift UVOT	uvw2	627	19.470 ± 0.091
2018 Nov 09.796	195.806	Swift UVOT	uvw2	341	19.508 ± 0.092
2018 Nov 23.112	209.122	Swift UVOT	uvw2	625	19.597 ± 0.095
2018 Dec 07.584	223.594	Swift UVOT	uvw2	238	19.643 ± 0.134
2018 Dec 11.432	227.442	Swift UVOT	uvw2	278	19.488 ± 0.120
2018 Dec 21.089	237.099	Swift UVOT	uvw2	733	19.466 ± 0.088
2019 Jan 04.489	251.499	Swift UVOT	uvw2	547	19.561 ± 0.097
2019 Jan 18.088	265.098	Swift UVOT	uvw2	642	19.360 ± 0.089
2019 Feb 02.427	280.437	Swift UVOT	uvw2	691	19.870 ± 0.101
2019 Feb 07.470	285.480	Swift UVOT	uvw2	647	19.672 ± 0.097
2019 Feb 15.341	293.351	Swift UVOT	uvw2	378	19.832 ± 0.122
2019 Feb 21.184	299.194	Swift UVOT	uvw2	108	19.891 ± 0.214
2019 Mar 07.628	313.638	Swift UVOT	uvw2	613	19.965 ± 0.111
2019 Mar 21.039	327.049	Swift UVOT	uvw2	434	19.509 ± 0.104
2019 Apr 04.189	341.199	Swift UVOT	uvw2	761	19.784 ± 0.096
2019 Apr 18.778	355.788	Swift UVOT	uvw2	533	19.563 ± 0.100
2019 Apr 24.651	361.661	Swift UVOT	uvw2	616	19.651 ± 0.098
2019 Jul 21.262	449.272	Swift UVOT	uvw2	491	19.705 ± 0.109
2019 Aug 18.753	477.763	Swift UVOT	uvw2	548	19.455 ± 0.096
2019 Sep 16.761	506.771	Swift UVOT	uvw2	465	19.589 ± 0.098
2019 Oct 14.747	534.757	Swift UVOT	uvw2	634	19.683 ± 0.097
2019 Nov 14.439	565.449	Swift UVOT	uvw2	567	19.256 ± 0.089
2019 Dec 09.223	590.233	Swift UVOT	uvw2	475	19.285 ± 0.094
2020 Jan 12.724	624.734	Swift UVOT	uvw2	319	19.342 ± 0.108
2020 Feb 12.124	655.134	Swift UVOT	uvw2	288	19.601 ± 0.125
2020 Mar 12.117	684.127	Swift UVOT	uvw2	317	19.293 ± 0.107
2020 Apr 12.353	715.363	Swift UVOT	uvw2	292	19.188 ± 0.108
2020 Aug 24.430	849.440	Swift UVOT	uvw2	331	19.722 ± 0.122

Table A4: AAVSO observers, including their country and astronomical society if available.

Observer code	Name	Country	Society
AAVSO AFSA	Soldán Alfaro, Francisco	ES	AAVSO
AAVSO ATE	Arranz, Teofilo	ES	AAVSO
AAVSO BDG	Boyd, David	GB	BAA-VSS
AAVSO BMSA	Bundas, Matthew	US	AAVSO
AAVSO BRIA	Biernikowicz, Richard	PL	AAVSO
AAVSO CDJA	Coulter, Daniel	US	AAVSO
AAVSO DKS	Dvorak, Shawn	US	AAVSO
AAVSO DPA	Diepvens, Alfons	BE	VVS
AAVSO EHEA	Eggenstein, Heinz-Bernd	DE	AAVSO
AAVSO ETOA	Eenmae, Tonis	EE	AAVSO
AAVSO FRL	Fournier, Ronald	US	AAVSO
AAVSO GJED	Gout, Jean-Francois	US	AAVSO
AAVSO JDAD	Janzen, Daryl	CA	
AAVSO JPG	Jordanov, Penko	BG	AAVSO
AAVSO KHAB	Kiiskinen, Harri	FI	URSA
AAVSO LDJ	Lane, David	CA	RASC
AAVSO LRCA	Larochelle, Riley	CA	AAVSO
AAVSO MDYA	Mankel, Dylan	US	AAVSO
AAVSO MIW	Miller, Ian	GB	BAA-VSS
AAVSO MMAO	Morales Aimar, Mario	ES	AAVSO
AAVSO MRV	Modic, Robert	US	AAVSO
AAVSO MUY	Muyllaert, Eddy	BE	
AAVSO NRNA	Naves, Ramon	ES	AAVSO
AAVSO OAR	Oksanen, Arto	FI	URSA
AAVSO ODEA	O'Keeffe, Derek	IE	AAVSO
AAVSO PMAK	Pyatnytskyy, Maksym	UA	AAVSO
AAVSO RBRB	Rodgers, Brennan	CA	
AAVSO RRIB	Rast, Rina	CA	RASC
AAVSO RZD	Rodriguez Perez, Diego	ES	AFOEV
AAVSO SDM	Schwendeman, Erik	US	AAVSO
AAVSO SFRA	Schorr, Frank	US	AAVSO
AAVSO SGEA	Stone, Geoffrey	US	AAVSO
AAVSO SHS	Sharpe, Steven	CA	AAVSO
AAVSO SSTA	Shadick, Stanley	CA	RASC
AAVSO STYA	Sove, Tylor	CA	
AAVSO TRT	Tordai, Tamás	HU	MCSE
AAVSO VMAG	Vrastak, Martin	SK	AAVSO
AAVSO VOL	Vollmann, Wolfgang	AT	AAVSO
AAVSO VRG	Venne, Roger	CA	AAVSO
AAVSO WKL	Wenzel, Klaus	DE	BAV

Table A5. V392 Per light curve parameters, under the assumption that each can be modelled by up to six broken power laws of form $f \propto t^{\alpha}$, where t_i and t_f denote the initial and final extent of each power law, respectively, and D is the duration of each power law's dominance.

uvw2	α	t_i [d]	t_f [d]	D [d]	uvm2	α	t_i [d]	t_f [d]	D [d]
5	-1.66 ± 0.14	70.0	186.4	116.4	5	-1.64 ± 0.11	70.0	181.0	111.0
6	0	186.4	849.4	663.1	6	0	181.0	849.4	668.4
uvw1	α	t_i [d]	t_f [d]	D [d]	u' fit	α	t_i [d]	t_f [d]	D [d]
4	. . .	-	. . .	-	4	-1.93 ± 0.42	70.0	103.5	33.5
5	-1.82 ± 0.09	70.0	182.2	112.2	5	-1.60 ± 0.10	103.5	195.9	92.3
6	0	182.2	849.4	667.2	6	-0.01 ± 0.09	195.9	1011.9	816.0
B	α	t_i [d]	t_f [d]	D [d]	*V*	α	t_i [d]	t_f [d]	D [d]
1	-1.75 ± 0.04	0.0	5.6	5.6	1	-1.76 ± 0.07	0.0	5.3	5.3
2	-0.15 ± 0.18	5.6	9.0	3.3	2	-0.45 ± 0.09	5.3	10.2	4.9
3	-2.18 ± 0.08	9.0	58.2	49.2	3	-2.72 ± 0.05	10.2	14.6	4.4
4	-2.42 ± 0.53	70.0	95.3	25.3	4	-2.08 ± 0.04	14.6	98.5	84.0
5	-1.22 ± 0.07	95.3	218.4	123.2	5	-1.07 ± 0.05	98.5	220.4	121.8
6	-0.11 ± 0.10	218.4	1011.9	793.5	6	-0.12 ± 0.05	220.4	1011.9	791.5
r'	α	t_i [d]	t_f [d]	D [d]	*i'*	α	t_i [d]	t_f [d]	D [d]
1	-1.78 ± 0.80	0.0	5.1	5.1	1	-3.22 ± 0.37	0.0	3.9	3.9
2	-0.52 ± 0.18	5.1	11.2	6.1	2	-1.05 ± 0.27	3.9	12.7	8.8
3	-2.86 ± 0.12	11.2	24.9	13.7	3	-3.78 ± 0.18	12.7	23.2	10.5
4	-2.37 ± 0.05	33.9	100.1	66.2	4	-2.52 ± 0.20	63.4	96.5	33.1
5	-0.94 ± 0.09	100.1	232.5	132.4	5	-0.83 ± 0.10	96.5	232.6	136.1
6	-0.06 ± 0.04	232.5	1011.9	779.4	6	-0.017 ± 0.04	232.6	1011.9	779.3
z'	α	t_i [d]	t_f [d]	D [d]					
4	-1.92 ± 0.27	70.0	96.0	26.0					
5	-0.86 ± 0.06	96.0	200.5	104.5					
6	-0.06 ± 0.08	200.5	1011.9	811.5					

Table A6: P Cygni velocities of Balmer line profiles from early time spectra of
V392 Per.

Time / days	Hα Slow / km s⁻¹	Hα Fast / km s⁻¹	Hβ Slow / km s⁻¹	Hβ Fast / km s⁻¹	Hγ Slow / km s⁻¹	Hγ Fast / km s⁻¹
1.91	−2994 ± 23	−4960 ± 23	−3209 ± 31	−5061 ± 31	−3180 ± 35	−4873 ± 35
2.13	−3070 ± 32	−5053 ± 32	−3602 ± 43	−5459 ± 43	−3583 ± 48	−5035 ± 48
2.88	−3748 ± 23	−5485 ± 23	−3796 ± 31	−5153 ± 31	−3802 ± 35	−5046 ± 35
2.90	−3840 ± 23	−5600 ± 23	−3641 ± 31	−5153 ± 31	−3664 ± 35	−5046 ± 35
3.85	. . .	−4068 ± 23	. . .	−5153 ± 31	. . .	−5046 ± 35
3.87	. . .	−4092 ± 26	. . .	−3861 ± 36	. . .	−3716 ± 40
4.16	. . .	−3829 ± 40	. . .	−3781 ± 54	. . .	−3249 ± 61
4.80	. . .	. . .	. . .	−3905 ± 11	. . .	. . .
4.82	. . .	−4007 ± 8	. . .	. . .	. . .	. . .
4.87	−3958 ± 73	. . .	−3593 ± 49	−3988 ± 49	−3216 ± 55	−3659 ± 55
4.88	. . .	−4274 ± 23	. . .	−4073 ± 31	−3664 ± 35	−4320 ± 35
5.16	. . .	−4031 ± 42	. . .	−3770 ± 57	. . .	−3749 ± 64
5.86	. . .	−4137 ± 23	. . .	−3765 ± 31	. . .	−3698 ± 35
5.87	−4049 ± 73	. . .	−3232 ± 49	−3677 ± 49	−3452 ± 55	−3673 ± 55
5.90	. . .	−4137 ± 23	. . .	−3580 ± 31	. . .	−3456 ± 35
5.94	. . .	−3991 ± 43	. . .	−3520 ± 58	. . .	−3485 ± 65
6.13	−3937 ± 32	. . .	−3307 ± 43	−3782 ± 43	−3321 ± 48	−3757 ± 48
6.86	. . .	−3954 ± 23	. . .	−3641 ± 31	. . .	−3767 ± 35
6.87	−3931 ± 27	. . .	−3366 ± 22	−3820 ± 22	−3410 ± 24	−3724 ± 24
6.90	. . .	−4023 ± 23	. . .	−3580 ± 31	. . .	−3491 ± 35
6.96	. . .	−4017 ± 22	. . .	−3763 ± 30	. . .	−3570 ± 34
7.13	−3904 ± 32	. . .	−3356 ± 43	−3831 ± 43	−3346 ± 48	−3782 ± 48
7.84	−3815 ± 2	−3981 ± 2	−3441 ± 3	−3823 ± 3	. . .	. . .
7.88	. . .	−3986 ± 26	. . .	−3576 ± 36	. . .	−3317 ± 40
7.87	. . .	−3931 ± 23	. . .	−3580 ± 31	. . .	−3698 ± 35
8.13	. . .	. . .	−3352 ± 43	−3785 ± 43	−3300 ± 48	. . .
8.14	. . .	. . .	. . .	−3642 ± 52	. . .	−3576 ± 58
8.85	. . .	−3975 ± 2	−3333 ± 3	−3468 ± 3	. . .	. . .
8.88	. . .	−4137 ± 23	. . .	−3518 ± 31	. . .	−3422 ± 35
8.90	. . .	−4320 ± 23	. . .	−3518 ± 31	−3387 ± 35	−3871 ± 35
9.13	. . .	−4099 ± 37	. . .	−3709 ± 50	. . .	−3668 ± 56
9.80	. . .	−4099 ± 37	. . .	. . .	. . .	. . .
9.83	. . .	. . .	. . .	−3369 ± 11	. . .	. . .
9.87	. . .	. . .	. . .	−3394 ± 31	. . .	. . .
9.88	. . .	−4160 ± 23	−3549 ± 31	−4012 ± 31	. . .	−3456 ± 35
9.93	. . .	−4161 ± 22	. . .	−3683 ± 30	. . .	−3453 ± 34
9.93	. . .	−4228 ± 23	. . .	−3394 ± 31	. . .	−3525 ± 35

Table A7: Dereddened line fluxes for Hα, Hβ, [O III] 5007 Å and [O III] 4959 Å.

Time / days	Hα Flux / erg cm^{-2} s^{-1}	Hβ Flux / erg cm^{-2} s^{-1}	[O III] 5007 Å Flux / erg cm^{-2} s^{-1}	[O III] 4959 Å Flux / erg cm^{-2} s^{-1}
4.9	$(3.219 \pm 0.060) \times 10^{-7}$	$(1.815 \pm 0.018) \times 10^{-7}$	. . .	. . .
5.9	$(2.514 \pm 0.042) \times 10^{-7}$	$(1.119 \pm 0.018) \times 10^{-7}$	. . .	. . .
6.9	$(2.739 \pm 0.031) \times 10^{-7}$	$(1.026 \pm 0.014) \times 10^{-7}$	. . .	. . .
76.2	$(6.852 \pm 0.133) \times 10^{-10}$	. . .	. . .	. . .
77.2	$(6.811 \pm 0.118) \times 10^{-10}$	$(9.516 \pm 0.867) \times 10^{-11}$	$(9.448 \pm 0.257) \times 10^{-10}$	$(2.724 \pm 0.171) \times 10^{-10}$
82.2	$(5.179 \pm 0.105) \times 10^{-10}$	$(1.426 \pm 0.061) \times 10^{-10}$	$(1.359 \pm 0.022) \times 10^{-9}$	$(4.131 \pm 0.126) \times 10^{-10}$
84.2	$(4.645 \pm 0.122) \times 10^{-10}$	$(1.349 \pm 0.095) \times 10^{-10}$	$(1.336 \pm 0.034) \times 10^{-9}$	$(4.053 \pm 0.185) \times 10^{-10}$
87.2	$(4.175 \pm 0.093) \times 10^{-10}$	$(1.512 \pm 0.089) \times 10^{-10}$	$(1.968 \pm 0.026) \times 10^{-9}$	$(6.061 \pm 0.197) \times 10^{-10}$
89.2	$(4.012 \pm 0.086) \times 10^{-10}$	$(1.126 \pm 0.084) \times 10^{-10}$	$(1.226 \pm 0.028) \times 10^{-9}$	$(4.014 \pm 0.171) \times 10^{-10}$
101.2	$(3.351 \pm 0.076) \times 10^{-10}$	$(8.151 \pm 0.595) \times 10^{-11}$	$(1.000 \pm 0.018) \times 10^{-9}$	$(3.169 \pm 0.103) \times 10^{-10}$
112.1	$(2.088 \pm 0.041) \times 10^{-10}$	$(5.775 \pm 0.440) \times 10^{-11}$	$(7.511 \pm 0.126) \times 10^{-10}$	$(2.621 \pm 0.074) \times 10^{-10}$
143.2	$(1.519 \pm 0.030) \times 10^{-10}$	. . .	. . .	. . .
157.0	$(9.964 \pm 0.282) \times 10^{-11}$	$(1.918 \pm 0.295) \times 10^{-11}$	$(4.670 \pm 0.073) \times 10^{-10}$	$(1.655 \pm 0.046) \times 10^{-10}$
186.2	$(7.052 \pm 0.239) \times 10^{-11}$	$(1.402 \pm 0.290) \times 10^{-11}$	$(3.556 \pm 0.069) \times 10^{-10}$	$(1.211 \pm 0.042) \times 10^{-10}$
212.1	. . .	$(1.259 \pm 0.268) \times 10^{-11}$	$(2.523 \pm 0.061) \times 10^{-10}$	$(8.952 \pm 0.361) \times 10^{-11}$
226.1	$(4.899 \pm 0.181) \times 10^{-11}$	. . .	. . .	. . .
252.0	$(3.158 \pm 0.222) \times 10^{-11}$	. . .	. . .	. . .
253.0	$(3.306 \pm 0.222) \times 10^{-11}$	$(7.745 \pm 1.507) \times 10^{-12}$	$(1.464 \pm 0.035) \times 10^{-10}$	$(5.066 \pm 0.204) \times 10^{-11}$
306.9	$(2.588 \pm 0.237) \times 10^{-11}$	$(7.583 \pm 1.455) \times 10^{-12}$	$(9.551 \pm 0.344) \times 10^{-11}$	$(3.862 \pm 0.222) \times 10^{-11}$
345.9	$(1.904 \pm 0.153) \times 10^{-11}$	$(4.157 \pm 1.110) \times 10^{-12}$	$(5.929 \pm 0.284) \times 10^{-11}$	$(2.541 \pm 0.203) \times 10^{-11}$
448.2	$(8.407 \pm 0.958) \times 10^{-12}$	. . .	. . .	. . .
478.2	$(7.274 \pm 0.947) \times 10^{-12}$	. . .	. . .	. . .
504.1	$(8.252 \pm 1.004) \times 10^{-12}$	. . .	. . .	. . .
535.0	$(6.146 \pm 0.861) \times 10^{-12}$	. . .	. . .	. . .
568.1	$(5.209 \pm 0.690) \times 10^{-12}$	. . .	. . .	. . .
591.0	$(4.961 \pm 0.570) \times 10^{-12}$	. . .	. . .	. . .
854.2	$(4.541 \pm 0.278) \times 10^{-12}$	. . .	. . .	. . .

Table A8: Dereddened line fluxes for [O III] 4363 Å, He I 6678 Å, He I 7065 Å and
He II 4686 Å.

Time / days	[O III] 4363 Å flux / erg cm⁻² s⁻¹	He I 6678 Å flux / erg cm⁻² s⁻¹	He I 7065 Å flux / erg cm⁻² s⁻¹	He II 4686 Å flux / erg cm⁻² s⁻¹
4.9	. . .	$(5.303 \pm 0.011) \times 10^{-9}$	$(3.735 \pm 0.038) \times 10^{-8}$	. . .
5.9	. . .	$(2.763 \pm 0.003) \times 10^{-9}$	$(2.754 \pm 0.032) \times 10^{-8}$	. . .
6.9	. . .	$(2.696 \pm 0.002) \times 10^{-9}$	$(2.107 \pm 0.021) \times 10^{-8}$	. . .
76.2	. . .	$(5.266 \pm 0.051) \times 10^{-12}$	$(1.989 \pm 0.061) \times 10^{-10}$	. . .
77.2	$(1.757 \pm 0.327) \times 10^{-10}$	$(4.664 \pm 0.012) \times 10^{-12}$	$(1.694 \pm 0.032) \times 10^{-10}$	. . .
82.2	$(3.897 \pm 0.216) \times 10^{-10}$	$(2.741 \pm 0.053) \times 10^{-12}$	$(8.373 \pm 0.364) \times 10^{-11}$	$(1.089 \pm 0.102) \times 10^{-10}$
84.2	$(4.595 \pm 0.289) \times 10^{-10}$	. . .	$(6.934 \pm 0.383) \times 10^{-11}$	$(9.858 \pm 1.208) \times 10^{-11}$
87.2	$(4.752 \pm 0.256) \times 10^{-10}$	$(2.436 \pm 0.010) \times 10^{-12}$	$(1.164 \pm 0.028) \times 10^{-10}$	. . .
89.2	$(3.101 \pm 0.281) \times 10^{-10}$	$(2.647 \pm 0.178) \times 10^{-12}$	$(5.933 \pm 0.411) \times 10^{-11}$	$(8.481 \pm 0.815) \times 10^{-11}$
101.2	$(2.540 \pm 0.198) \times 10^{-10}$	$(9.985 \pm 0.090) \times 10^{-13}$	$(5.602 \pm 0.326) \times 10^{-11}$	$(4.667 \pm 0.592) \times 10^{-11}$
112.1	$(1.388 \pm 0.104) \times 10^{-10}$	$(1673.492 \pm 0.001) \times 10^{-15}$	$(2.990 \pm 0.126) \times 10^{-11}$	$(4.503 \pm 0.430) \times 10^{-11}$
143.2	. . .	$(2.021 \pm 0.006) \times 10^{-12}$	$(6.177 \pm 0.180) \times 10^{-11}$	. . .
157.0	$(6.512 \pm 0.806) \times 10^{-11}$	$(15.503 \pm 0.004) \times 10^{-13}$	$(1.902 \pm 0.109) \times 10^{-11}$	$(2.391 \pm 0.155) \times 10^{-11}$
186.2	$(3.598 \pm 0.608) \times 10^{-11}$	$(1311.492 \pm 0.002) \times 10^{-15}$	$(1.026 \pm 0.067) \times 10^{-11}$	$(2.069 \pm 0.088) \times 10^{-11}$
212.1	$(2.464 \pm 0.607) \times 10^{-11}$	$(106.25 \pm 0.004) \times 10^{-14}$	$(1.096 \pm 0.141) \times 10^{-11}$	$(1.718 \pm 0.148) \times 10^{-11}$
226.1	. . .	$(1.318 \pm 0.004) \times 10^{-12}$	$(3.454 \pm 0.101) \times 10^{-11}$	. . .
252.0	. . .	$(1.166 \pm 0.011) \times 10^{-12}$	$(4.338 \pm 0.191) \times 10^{-11}$	. . .
253.0	$< 2.777 \times 10^{-11}$	$(92.876 \pm 0.005) \times 10^{-14}$	$(9.729 \pm 0.751) \times 10^{-12}$	$(1.357 \pm 0.053) \times 10^{-11}$
306.9	$< 3.037 \times 10^{-11}$	$(9.262 \pm 0.346) \times 10^{-13}$	$(8.284 \pm 0.782) \times 10^{-12}$	$(1.338 \pm 0.063) \times 10^{-11}$
345.9	$< 2.514 \times 10^{-11}$	$(1.070 \pm 0.003) \times 10^{-12}$	. . .	$(1.281 \pm 0.089) \times 10^{-11}$
448.2	. . .	$(1.080 \pm 0.001) \times 10^{-12}$	. . .	$(9.430 \pm 0.762) \times 10^{-12}$
478.2	. . .	$(9.950 \pm 0.063) \times 10^{-13}$	. . .	$(9.566 \pm 0.445) \times 10^{-12}$
504.1	. . .	$(1.219 \pm 0.013) \times 10^{-12}$	. . .	$(8.227 \pm 0.714) \times 10^{-12}$
535.0	. . .	$(8.822 \pm 0.053) \times 10^{-13}$	. . .	$(9.503 \pm 0.670) \times 10^{-12}$
568.1	. . .	$(8.295 \pm 0.050) \times 10^{-13}$	. . .	$(9.666 \pm 0.348) \times 10^{-12}$
591.0	. . .	$(1.270 \pm 0.048) \times 10^{-12}$	. . .	$(1.248 \pm 0.132) \times 10^{-11}$
854.2	. . .	. . .	. . .	$(9.493 \pm 0.407) \times 10^{-12}$

This paper has been typeset from a TeX/LaTeX file prepared by the author.